8-2020

Structure and Adsorption at the Bastnäsite-Water Interface: Fundamental Investigations toward Rare Earth Mineral Recovery

Anna Kristiina Wanhala
awanhala@vols.utk.edu

To the Graduate Council:

I am submitting herewith a dissertation written by Anna Kristiina Wanhala entitled "Structure and Adsorption at the Bastnäsite-Water Interface: Fundamental Investigations toward Rare Earth Mineral Recovery." I have examined the final electronic copy of this dissertation for form and content and recommend that it be accepted in partial fulfillment of the requirements for the degree of Doctor of Philosophy, with a major in Energy Science and Engineering.

Andrew G. Stack, Major Professor

We have read this dissertation and recommend its acceptance:

Lawrence M. Anovitz, Parans Paranthaman, Sheng Dai

Accepted for the Council:

Dixie L. Thompson

Vice Provost and Dean of the Graduate School

(Original signatures are on file with official student records.)

Structure and Adsorption at the Bastnäsite-Water Interface: Fundamental Investigations toward Rare Earth Mineral Recovery

A Dissertation Presented for the

Doctor of Philosophy

Degree

The University of Tennessee, Knoxville

Anna Kristiina Wanhala

August 2020

ACKNOWLEDGEMENTS

The CTR work in Chapter 4 would not have been possible without the support and guidance of Joanne Stubbs. Sang Soo Lee assisted in additional data collection for this work.

ABSTRACT

This dissertation investigates the interfacial structure and reactivity of a rare earth mineral in the context of froth flotation. Bastnäsite [(Ce,La,Nd)FCO_3], one of the primary mineral sources of rare earth elements, has been chosen for this investigation. Flotation separation relies on selective adsorption of collector ligands to the desired mineral surface in solution; fundamental understanding of these adsorption reactions will aid in the development of more effective separation technologies.

Chapter 1 presents an introduction to the significance of rare earth minerals and the process of froth flotation. Chapters 2 and 3 address the adsorption reactions of ligand molecules at the interface. Chapter 2 analyzes the adsorption mechanism of octanohydroxamic acid, a popular candidate for bastnäsite flotation. In-situ FTIR reveals mechanistic information that demystifies the quantitative results of the adsorption isotherm. Chapter 3 compares several flotation ligands to determine the effect of ligand structure on the mechanism of adsorption.

In Chapter 4, the structure of the bastnäsite (001) surface is investigated under varying conditions using X-Ray reflectivity. The surface termination is significant because it determines which sites are available for ligand adsorption in the flotation system. Changes in the surface structure are evaluated by fitting a model to a set of crystal truncation rods measured at this interface. This work provides fundamental information about the aqueous geochemistry of bastnäsite flotation on both sides of the interface.

TABLE OF CONTENTS

LIST OF TABLES

LIST OF FIGURES

CHAPTER 1
INTRODUCTION

Improving the efficiency of mineral beneficiation processes is crucial to meeting the increasing global demand for rare earth elements. Efforts to develop new separation strategies will benefit from a fundamental understanding of processes influencing adsorption at the mineral-water interface. The goal of this dissertation is to answer longstanding questions about adsorption in the bastnäsite flotation system. Chapters 2 and 3 investigate the mechanisms by which flotation collectors adsorb to bastnäsite, and how these reactions are influenced by molecular structure. Chapter 4 focuses on the bastnäsite surface, revealing the termination structure of the dominant crystal face. These findings provide fundamental information to guide a rationalized, targeted approach to designing new collectors for bastnäsite.

Background

The significance of rare earth elements (REEs) in modern technology has increased the demand for these materials. Clean energy technologies are particularly reliant on REEs—specifically catalytic converters, permanent magnets, and batteries.[1] Applications in the medical field and consumer electronics are also major contributors to demand.[2, 3]

As of 2014, China accounted for 86.3% of global REE production. China's advantage in the rare earths market is due in part to its ionic clay deposits, which contain a higher proportion of heavy rare earths, and are somewhat easier to process than other mineral sources.[4] Environmental regulations are in place for REE processing in China, but regulated production in 2018 only accounted for about two thirds of the estimated total.[5] The environmental impacts of unregulated mining are severe; for each ton of rare earth oxide produced, as much as 1000 tons of wastewater is created, exposing the local environment to heavy metals and leaching reagents.[4]

Without competition, harmful mining practices will continue to meet the rising global demand for rare earths. Increasing the supply of rare earths requires innovations that are not only more economical than previous strategies, but also more environmentally friendly.

A variety of minerals contain REEs, but only a few have a high enough concentration to be commercially viable. Bastnäsite [$(REE)CO_3F$] is currently the primary mineral source. Other important REE ores are Monazite [$(REE, Th)PO_4$] and xenotime [YPO_4].[6, 7]

A single sample of bastnäsite can contain multiple elements in varying proportion, depending on the source. An analysis of samples from the Mountain Pass ore deposit in California found mostly cerium and lanthanum bastnäsite (41.6% and 41.0% respectively), followed by neodymium (10.1%), praseodymium (3.3%), and small amounts of samarium, europium, and gadolinium (less than 1% each).[8]

A major obstacle to bastnäsite production is poor separation from undesired gangue minerals, particularly calcite ($CaCO_3$). An analysis of the composition of bastnäsite ore from Mountain Pass, California also found significant amounts of silicon dioxide, calcium oxide, and barite.[8] Previous mining operations in this deposit recovered only 65-70% of available REEs in the beneficiation of bastnäsite.[9, 10] The final concentrate contained significant amounts of gangue minerals, resulting in a 63% rare earth oxide content. Mining efforts in the Bayan Obo region of China—the most significant producer of REEs—have had devastating environmental impacts, while recovering only about 72% of rare earth content.[11, 12]

Froth Flotation

In the mining process, flotation is the primary method used for separating REE ores from unwanted (gangue) ores. This process is represented

schematically in Figure 1.1. The finely ground ore is added to a slurry containing amphiphilic ligands, called collectors. Collectors have a polar functional group, which adsorbs to the charged mineral surface, and a nonpolar tail, which is hydrophobic. When a layer of collector molecules is formed on the mineral particles, they become hydrophobic. Air bubbles are circulated through the slurry, allowing the particles to attach and float to the top of the solution.

The efficacy of a flotation system can be described both in terms of recovery and selectivity. *Recovery* refers to the total amount of rare earth content present in the starting ore that is collected in the final product. Poor recovery results in the loss of valuable materials to waste streams. *Selectivity* refers to the amount of rare earths recovered relative to gangue. Improvements in selectivity often come at the cost of decreased recovery; to avoid floating undesired products, a flotation collector with low overall reactivity must be used. For instance, a highly-charged anion will adsorb readily to any positively charged surface, resulting in high recovery of many mineral types and poor selectivity. The fundamental work in this dissertation is mostly focused on maximizing the strength of interaction between collectors and bastnäsite surfaces, presenting key insights into one piece of the froth flotation puzzle.

Solution chemistry is a crucial factor in froth flotation. Separation relies on selectivity of the collector for the desired mineral phases. However, adsorption is influenced by chemical and electrostatic interactions. In practice, froth flotation involves many steps and added reagents to achieve separation. This is particularly true for traditional collectors, which are not inherently selective. To separate bastnäsite using fatty acid collectors, the ore undergoes several high-temperature conditioning steps. Sodium carbonate is added to control the pH and carbonate equilibrium in solution, and lignin sulfonate is added as a depressant, adsorbing to gangue ores to prevent flotation. Electrokinetic experiments have shown that these treatments have a significant effect on barite gangue, inducing

a negative surface charge to inhibit adsorption of anionic collectors.[13] However, separation from calcite remains a challenge.

Collectors containing hydroxamic and phosphoric acid functional groups are more selective for bastnäsite than fatty acids.[14, 15] While many potential ligands have shown promise, modifications to the flotation system are still needed to achieve separation. To offset the increased cost, specialized collectors must be highly selective. If the chemistry of adsorption is well understood, collector performance can be further enhanced by optimizing the solution conditions.

Organization of Dissertation

This dissertation incorporates several studies to evaluate collector adsorption to bastnäsite. Chapters 2 and 3 explore the specific interaction of ligands at the surface in varying solutions. In Chapter 2, the mechanism of adsorption of alkyl hydroxamic acid, a potential flotation collector, onto bastnäsite is determined using *in-situ* Fourier transform infrared (FTIR) spectroscopy. This work resulted in a first-author publication:

Wanhala, A. K.; Doughty, B.; Bryantsev, V. S.; Wu, L.; Mahurin, S. M.; Jansone-Popova, S.; Cheshire, M. C.; Navrotsky, A.; Stack, A. G., Adsorption Mechanism of Alkyl Hydroxamic Acid onto Bastnäsite: Fundamental Steps toward Rational Collector Design for Rare Earth Elements. *Journal of Colloid and Interface Science* **2019**.

The *in-situ* FTIR methodology is further applied in Chapter 3 to investigate some effects of ligand structure on reactivity. Two sets of related collectors are compared. These experiments were a key part of collaborative projects involving multiple experimental and computational approaches. The results presented in Chapter 3 contributed to two publications:

Sutton, J. E.; Roy, S.; Chowdhury, A. U.; Wu, L.; Wanhala, A. K.; De Silva, N.; Jansone-Popova, S.; Hay, B. P.; Cheshire, M. C.; Windus, T. L., Molecular Recognition at Mineral Interfaces: Implications for the Beneficiation of Rare Earth Ores. *ACS Applied Materials & Interfaces* **2020,** *12* (14), 16327-16341.

Chapelski, R.; Chowdhury, A.U.; Wanhala, A.K.; Bocharova, V.; Roy,S; Keller, P.C.; Everly, D.; Jansone-Popova, S.; Kisliuk, A.; Sacci, R.L.; Stack, A.G.; Anderson, C.G.; Doughty, B.; Bryantsev, V.S., Thinking Small to Avoid Large Losses: a Molecular-Scale Approach to Rare-Earth Beneficiation. *iScience* **2020**.

Finally, in Chapter 4, a best-fit model is fit to crystal truncation rod (CTR) X-ray reflectivity data of the bastnäsite (001) surface, revealing the atomic structure of the terminated surface. At the time of this dissertation, a first-author publication of this work is still in development.

References

1. Eggert, R.; Wadia, C.; Anderson, C.; Bauer, D.; Fields, F.; Meinert, L.; Taylor, P., Rare earths: market disruption, innovation, and global supply chains. *Annual Review of Environment and Resources* **2016,** *41*, 199-222.
2. Castor, S. B.; Hedrick, J. B., Rare earth elements. *Industrial minerals volume, 7th edition: Society for mining, metallurgy, and exploration, Littleton, Colorado* **2006**, 769-792.
3. Ganguli, R.; Cook, D. R., Rare earths: A review of the landscape. *MRS Energy & Sustainability* **2018,** *5*.
4. Packey, D. J.; Kingsnorth, D., The impact of unregulated ionic clay rare earth mining in China. *Resources Policy* **2016,** *48*, 112-116.
5. *Mineral Commodity Summaries 2019*; Reston, VA, 2019.
6. Navrotsky, A.; Lee, W.; Mielewczyk-Gryn, A.; Ushakov, S. V.; Anderko, A.; Wu, H.; Riman, R. E., Thermodynamics of solid phases containing rare earth oxides. *The Journal of Chemical Thermodynamics* **2015,** *88*, 126-141.
7. Jackson, W. D.; Christiansen, G., *International Strategic Minerals Inventory Summary Report--rare-earth Oxides*. US Government Printing Office: 1993.
8. Lin, C.; Hsieh, C.-H.; Miller, J., Characterization of rare-earth resources at Mountain Pass, CA using high-resolution X-ray microtomography (HRXMT). *Mining, Metallurgy & Exploration* **2013,** *30* (1), 10-17.
9. Jordens, A.; Cheng, Y. P.; Waters, K. E., A review of the beneficiation of rare earth element bearing minerals. *Minerals Engineering* **2013,** *41*, 97-114.
10. Nagaraj, D.; Farinato, R., Evolution of flotation chemistry and chemicals: A century of innovations and the lingering challenges. *Minerals Engineering* **2016,** *96*, 2-14.
11. Chakhmouradian, A. R.; Wall, F., Rare earth elements: minerals, mines, magnets (and more). *Elements* **2012,** *8* (5), 333-340.
12. Gupta, C. K.; Krishnamurthy, N., EXTRACTIVE METALLURGY OF RARE-EARTHS. *International Materials Reviews* **1992,** *37* (5), 197-248.
13. Pradip; Fuerstenau, D., The role of inorganic and organic reagents in the flotation separation of rare-earth ores. *International Journal of Mineral Processing* **1991,** *32* (1-2), 1-22.
14. Jordens, A.; Marion, C.; Kuzmina, O.; Waters, K. E., Surface chemistry considerations in the flotation of bastnäsite. *Minerals Engineering* **2014,** *66*, 119-129.
15. Bulatovic, S., Flotation of REO minerals. *Handbook of Flotation Reagents: Chemistry, Theory and Practice. first ed. Elsevier Science, Amsterdam, NL* **2010**, 151-173.

Appendix

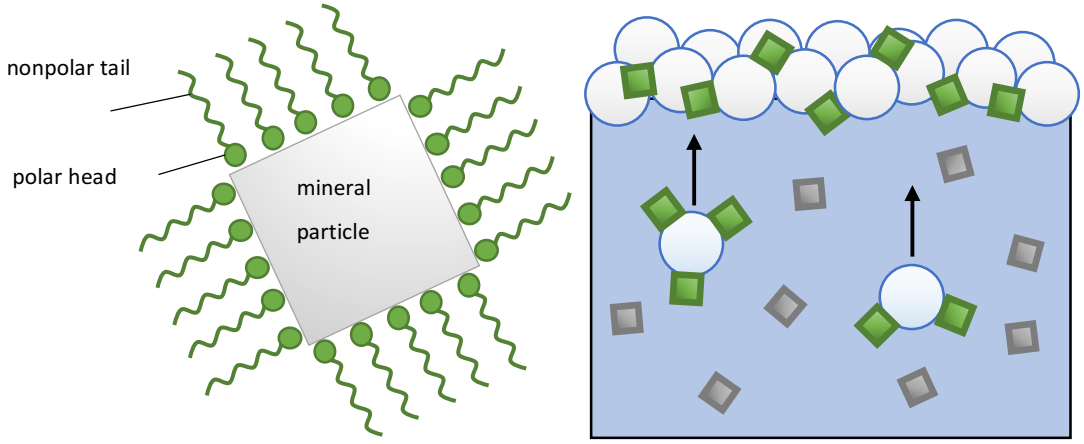

Figure 1.1: Schematic of froth flotation.

CHAPTER 2

ADSORPTION MECHANISM OF ALKYL HYDROXAMIC ACID ONTO BASTNÄSITE

A version of this chapter was originally published in the Journal of Colloid and Interface Sciences:

Anna K. Wanhala, Benjamin Doughty, Vyacheslav S. Bryantsev, Lili Wu, Shannon M. Mahurin, Santa Jansone-Popova, Michael C. Cheshire, Alexandra Navrotsky, Andrew G. Stack. “Adsorption mechanism of alkyl hydroxamic acid onto bastnäsite: Fundamental steps toward rational collector design for rare earth elements.” *Journal of Colloid and Interface Science* 553 (2019): 210-219.

The published version of this chapter is a result of a collaborative effort, connecting experimental and computational work from several research groups. Findings from each author were analyzed in the context of all other collaborators.

The Fourier transform infrared spectroscopy experiments were planned and conducted by the author. Benjamin Doughty was responsible for the sum frequency generation vibrational spectroscopy experiments. Vyacheslav S. Bryantsev provided density functional theory simulated vibrational frequencies for comparison with experimental results. Lili Wu and Alexandra Navrotsky conducted calorimetry experiments to measure the thermodynamics of the adsorption reaction. Santa Jansone-Popova assisted in the spectral interpretation. Shannon M. Mahurin provided support for the FTIR experiments, and Michael C. Cheshire assisted in the preparation of samples for FTIR analysis.

Abstract

Rare earth element (REE) production is limited in part by inefficient strategies for beneficiation. Hydroxamic acid ligands are promising reagents for the selective flotation of bastnäsite [(Ce,La)FCO_3], a major REE ore mineral, but the mechanism and energetics of adsorption are not understood, interfering with the design of new, more efficient reagents. Here, the adsorption of octyl hydroxamic acid onto bastnäsite was measured using a combination of experimental and computational methods. In-situ attenuated total reflectance Fourier transform infrared (ATR-FTIR) spectroscopy revealed changes in the hydroxamate functional group vibrational frequencies, corresponding to chelation with cerium cations at the bastnäsite surface. The results indicate a monodentate chemisorption mechanism at low surface loading that changes to bidentate chemisorption at higher concentrations. This interpretation is supported by molecular vibrational frequency shifts calculated using density functional theory (DFT), and orientation of the hydrocarbon chain measured by sum frequency generation (SFG) vibrational spectroscopy. The binding enthalpies of octyl hydroxamic acid interacting with La and Ce-bastnäsite surfaces were measured using isothermal titration calorimetry (ITC) revealing a stronger coordinating ability with bastnäsite than with a common gangue mineral, calcite ($CaCO_3$). Because octyl hydroxamate favors monodentate adsorption at low surface coverages, the relative chelating strength of metal ions could be a poor predictor for selectivity under monolayer adsorption conditions. At higher surface loadings, where the bidentate mode of adsorption is active, selectivity is likely to be limited by increased flotation of gangue ores.

Introduction

Rare earth elements (REEs) are ubiquitous in modern technology, used in devices ranging from catalytic converters, magnets, and electric vehicle batteries

to phosphors in smart phone displays.[1, 2] In spite of their importance for clean energy technologies, production of REE resources is wasteful and inefficient.[3] REEs are found in carbonates, phosphates, oxides, and other minerals. Due to their similar surface chemistry, separation of REE-bearing ore mineral phases from gangue, or unusable minerals, remains a major obstacle to production.[4, 5] Bastnäsite [$(Ce,La)FCO_3$] is the major ore mineral in the REE mine located at Mountain Pass, California, but a maximum of only 65–70% of available REEs are recovered during processing.[6] Additionally, many gangue minerals are unintentionally captured, resulting in a final concentrate composed of only 63% rare earth oxides.

The dominant method for separating REE ore minerals from the surrounding gangue is froth flotation, in which bubbles of air are injected through a mineral suspension containing an amphiphilic ligand, or collector. The ligand contains a polar functional group that adsorbs to the mineral surface and a nonpolar tail that causes the particles to segregate to the air-water interface. Typical ligands used for floating non-sulfide ores include carboxylic, hydroxamic, sulfonic, and phosphonic acids.[6] The current collector ligands used for bastnäsite are fatty acids, whose low selectivity for REE ore minerals is viewed as a major limitation to production. In particular, fatty acid ligands are ineffective at separating bastnäsite from the most common gangue mineral, calcite ($CaCO_3$), even at high temperatures.[6] While alkyl hydroxamic acids—particularly octanohydroxamic acid—have been reported to be more selective for bastnäsite than previously used fatty acid ligands, little is known about their mechanism of adsorption to bastnäsite surfaces.[7-9] Thus, it is not understood why they are more selective. More generally, rational design of new ligands with improved selectivity for REE ore minerals will benefit from a better, more fundamental understanding of ligand interaction at the surfaces of REE minerals and common gangue mineral surfaces such as calcite. Here we have chosen to focus on understanding the interaction of bastnäsite with octanohydroxamic acid.

Alkyl hydroxamic acid adsorption onto bastnäsite presumably involves chemisorption to cerium or lanthanum ions on the surface, through one or both oxygen atoms, shown in Figure 2.1 (all figures are collected in an appendix at the end of this chapter).[9-11] In aqueous solution, hydroxamate ligands readily form complexes with dissolved metal ions in a bidentate chelate, favoring trivalent rare earth cations over divalent calcium ions.[12] Previous work shows that adsorption is maximized at pH values where hydroxyl species of metal ions are abundant, possibly by chelation of hydroxamate with dissolved ions near the surface.[13] The stability of this complex provides a logical basis for hydroxamate selectivity for bastnäsite (containing cerium and other REE surface sites) over calcite (containing calcium). However, the solvation environment for the surface sites is not known, beyond a computational DFT study that shows direct coordination of only one water molecule at surface cerium sites.[14] The more restricted steric environment on a mineral surface relative to an aqueous solution may affect how ligand adsorption occurs on bastnäsite. Ultimately, it is not known which, if any, of the hypothesized mechanisms of adsorption shown in Figure 2.1 is correct. Thus, our focus is on determining the mechanism and thermodynamic favorability of alkyl hydroxamate adsorption onto bastnäsite surfaces by applying a mixture of spectroscopic, computational, and calorimetric methods.

We first use attenuated total reflectance Fourier transform infrared (ATR-FTIR) spectroscopy to probe adsorption. ATR-FTIR is suitable for studying adsorption in aqueous solutions because the infrared beam does not propagate throughout the sample cell, limiting the strong IR signal from water vibrations.[15-17] ATR- FTIR has been used to quantify adsorption of IR-active functional groups in organophosphates[18] and biomolecules[19-21] onto soil minerals. Organic compounds for mineral flotation also contain functional groups whose IR spectra are dependent on the bonding environment.[22-24] In previous work, FTIR spectra of hydroxamate-treated bastnäsite samples have shown additional peaks corresponding to vibrational modes of the collector.[11, 25, 26] However, applications

of FTIR to this system have so far been limited to ex-situ analysis of dried samples, primarily focusing on the presence of alkyl chain vibrations, which do not provide mechanistic information about the hydroxamate functional group. In this work, we observe distinct changes to the hydroxamate vibrational modes when the ligand is chemisorbed to bastnäsite in situ that allow us to interpret directly the mechanism of adsorption, and its changes as a function of solution composition.

We additionally use vibrational sum frequency generation (SFG), an interface-sensitive nonlinear optical method, to investigate the orientation of the alkyl chains of the adsorbed hydroxamate.[27-31] Analysis of resulting vibrational spectra, including band positions and relative intensities, reveals information about the interface, including chemical partitioning,[32, 33] reactivity,[34-36] ordering,[37, 38] and molecular orientation.[39-42]

ATR-FTIR and SFG spectroscopic techniques provide complementary information about hydroxamate adsorption onto bastnäsite. The FTIR spectra reflect changes to the hydroxamate functional group, i.e., adsorption shifts the frequency of vibrational modes involving the oxygen and nitrogen atoms, whereas the SFG spectra analyze the intensity of C-H stretching vibrations in the alkyl chain, which do not shift in IR frequency. SFG spectra collected with varying light polarizations reveal the average orientation angle of the alkyl tails, along with qualitative information about how well the layer is ordered.

Lastly, we use isothermal titration calorimetry (ITC) to determine the binding affinity of alkyl hydroxamate for both bastnäsite and calcite surfaces. Thus far, few calorimetric measurements have been reported for organic molecules interacting with mineral surfaces. The enthalpies of d-aluminum oxide interacting with various organic acids (phthalate, salicylate, benzoate, chlorophenol and aliphatic acids) have been measured by isothermal titration calorimetry (ITC),[43] with small exothermic heat effects that are ascribed to the proton transfer reaction.

The heat effects of ligand-mineral reactions are usually controlled by many factors including solution pH, size and properties of ligands (including molecular weight),[44] solvent effects, and surface coverage. Ligand-mineral binding energy directly impacts the effectiveness of ligands used in flotation, with a large difference in binding energy being favorable for selectivity.

Experimental Section

Adsorption Density Determination

The equilibrium adsorption density of octyl hydroxamic acid on calcite and bastnäsite particles was determined by solution depletion. Pure mineral samples were ground and analyzed by BET to determine their surface area. Individual samples for each mineral containing 50 mg of solid and 10 mL of calcite-saturated hydroxamate solution (pH ~8.3) were shaken for 16 hours, and then filtered to remove solids. The concentration of remaining hydroxamate in solution was measured using ion chromatography.

The isotherm results are shown in Figure 2.2. Adsorption density of hydroxamate was greater for bastnäsite than calcite at all concentrations tested, and monolayer coverage was exceeded on bastnäsite in 1 mM hydroxamate solution. The concentrations chosen for FTIR and SFG measurements in this work were based on these results. Because only one pH condition was tested, this is not an absolute measure of selectivity. Results of adsorption density measurements tend to vary depending on experimental conditions, including solution chemistry, solid-to-liquid ratio, sampling method, temperature, and particle size.

Fourier Transform Infrared Spectroscopy

To determine the FTIR spectrum of hydroxamate in bidentate coordination with metal ions, complexes of cerium and lanthanum hydroxamates were

synthesized. First, $Ce(NO_3)_3$ and $La(NO_3)_3$ (Aldrich, 99.99%) were dissolved in deionized water. Octanohydroxamic acid solution (Aldrich CPR-grade in deionized water) was then added to each solution in a 1:3 metal-to-ligand stoichiometric ratio. 0.1 M NaOH solution was added dropwise until a precipitate formed. The precipitate was filtered using vacuum filtration, rinsed with water, and dried.

ATR-FTIR spectra were collected using a PerkinElmer Frontier FTIR with a mercury cadmium telluride (MCT) detector and a 45° single-reflection diamond IRE accessory (PIKE Technologies GladiATR). Spectra were collected for 256 accumulations with 4 cm^{-1} resolution. Spectra of solid cerium and lanthanum complexes were measured for comparison with solid hydroxamic acid. The FTIR spectrum of free hydroxamate in solution was measured using 10 mM octanohydroxamic acid aqueous solution with 0.1 M NaCl background electrolyte. Solution spectra were taken at pH values from 6 to 11, adjusted by addition of 0.1 M NaOH or 0.1 M HCl. Aqueous hydroxamate bands were undetectable at lower concentrations used for adsorption measurements (<2 mM).

To analyze adsorption to bastnäsite in situ, natural bastnäsite samples from the Khyber Pass region of Pakistan were milled to particle size 5 μm. Mineralogy was verified using X-ray diffraction. A thin film of mineral particles was deposited by drying three 10 μL drops of bastnäsite in methanol suspension (7 mg/mL) on the ATR crystal. An aqueous solution of 0.1 M NaCl background electrolyte (100 mL) was flowed over the particle film at a rate of 10 mL/min with recirculation until no further changes were seen in the spectra. The background was then set before changing the solution to hydroxamic acid in 0.1 M NaCl (100 mL, recirculating). Adsorption of 1 mM hydroxamate solution was compared at pH 8.5 and 10. The pH of each solution was adjusted using 0.1 M NaOH and 0.1 M HCl. Spectra were taken under flowing hydroxamate solution at ten-minute

intervals over the course of an hour to allow the reaction to reach equilibrium (which may not occur in industrial settings).

Adsorption onto the bastnäsite film was measured at concentrations below 1 mM by flowing a 0.1 M NaCl background solution over the bastnäsite-coated ATR crystal, and incrementally increasing the concentration by adding 1mM hydroxamate solution. Adsorption was measured for one hour at a total concentration of 0.2 mM, before increasing the concentration to 0.4 mM, and then 0.6 mM. The solution pH was maintained at 9, which has been reported as the maximum floatability condition for bastnäsite with hydroxamate in the literature.[8, 11, 45]

Density Functional Theory Calculations

To analyze the vibrational modes measured in the ATR-FTIR, density functional theory (DFT) calculations were carried out using the Gaussian 16 Revision A.03 software package.[46] The PBE density functional[47] with the 6-311+G(d,p) basis set for light elements was employed for geometry optimization and harmonic vibrational frequency calculations. Ce^{3+} was modeled using large-core (LC) relativistic effective core potential (RECP) and the associated (7s6p5d2f)/[5s4p3d2f] basis sets.[48] Since LC RECP calculations include the 4f electrons in the core, they were performed on a pseudo singlet state configuration. Grimme's D3 dispersion correction[49] was applied in all calculations to provide a better account of noncovalent interactions. Fundamental vibrational frequencies were not scaled, because the recommended[50] scaling factor for PBE/6–311+G(d,p) with no dispersion correction is close to unity (0.9944). To better mimic the solvent environment, two water molecules were added to the deprotonated ligand and seven to eight water molecules were added to form a nine-coordinate complex with Ce^{3+}, completing its primary coordination shell. IR spectra were visualized using the ChemCraft program.[51]

Sum Frequency Generation Vibrational Spectroscopy

Broadband vibrational SFG measurements utilized two intense laser pulses, one in the mid-infrared (IR) and another in the near-infrared (NIR), that are temporally and spatially overlapped at the mineral-solution interface. Simultaneous interaction of the IR and NIR laser pulses creates a coherent second order polarization that radiates new light at the sum and difference frequencies of the driving laser fields. The intensity, expressed in Equation 2.1, is proportional to the square of the second order nonlinear susceptibility, $\chi_{eff}^{(2)}$, and the two incident laser fields, (E_{ω}). The effective second order nonlinear susceptibility, shown in Equation 2.2, is the sum of resonant ($\chi_{res}^{(2)}$) and non-resonant ($\chi_{NR}^{(2)}$) contributions. The resonant contribution is a function of the frequency of the incident IR laser (ω_{IR}), amplitude of the *k*th vibrational mode (A_k), the measured vibrational frequency (ω_k), and the spectral linewidth (Γ_k).

$$I_{SFG} \propto \left|\chi_{eff}^{(2)} E_{\omega 1} E_{\omega 2}\right|^2 \tag{2.1}$$

$$\chi_{eff}^{(2)} = \chi_{NR}^{(2)} + \chi_{res}^{(2)} = \chi_{NR}^{(2)} + \sum_k \frac{A_k}{\omega_{IR} - \omega_k + i\Gamma_k} \tag{2.2}$$

When a molecular vibration is in resonance with the incident IR laser, there is an enhancement in the SFG signal, thereby mapping the interfacial vibrational spectrum. Notably, SFG from bulk species in isotropic and centrosymmetric media destructively interferes, leaving only the molecules present at the interface, where symmetry is broken, to contribute to the signal.

Details of our SFG instrumentation can be found elsewhere.[52] Briefly, the output of a femtosecond regenerative amplifier (Spectra Physics Spitfire Pro), producing ~6 mJ pulses at 1 kHz was split into two arms. One arm was directed into a TOPAS-Prime Plus optical parametric amplifier and difference frequency mixer to produce mid-infrared (IR) pulses. The output mid-IR light was centered at ~2900 cm^{-1} having approximately a 300 cm^{-1} bandwidth at full width half

maximum. The second arm utilized ~1.2 mJ of the remaining near infrared (NIR) light and was directed into a compact 4*f*-pulse shaper outfitted with a spatial light modulator at the Fourier plane. This converted the femtosecond NIR pulse into a spectrally narrowband picosecond pulse.

SFG data were collected with the spectral bandwidth fixed at ~0.8 nm. The polarizations for each arm were purified by appropriate polarizers and rotated with zero-order half waveplates before being combined colinearly in a dichroic optic. The light was focused on the sample using a CaF_2 lens at a 60° angle relative to the surface normal. Radiated SFG light was collected by an achromatic doublet in a reflection geometry. The SFG was polarization-resolved and filtered using a 750 nm shortpass filter before being sent into an Acton sp300*i* spectrograph furnished with a Pixis 256E CCD. All data collection was performed with custom LabVIEW software. SFG spectra were collected in different polarization combinations, e.g., SSP, PPP, and SPS, where the letters in the abbreviation represent the polarization of SFG, NIR, and IR pulses respectively. Raw SFG spectra were background subtracted using co-specified regions of interest and scaled to the IR spectra collected from the neat bastnäsite sample itself in the PPP combination.

Isothermal Titration Calorimetry

Isothermal titration calorimetry (ITC) was used to quantify the interaction energetics, i.e., to measure the enthalpies of hydroxamic ligand interaction with bastnäsite and calcite. Adsorption enthalpy measurements were conducted using an isothermal titration calorimetry (ITC) CSC 4200 instrument operated at 25° C. To provide enough surface area for measurable heat effects in the experiment with a limited amount of sample, two nanoscale bastnäsite samples ($LaFCO_3$ and $CeFCO_3$, laboratory made) and a commercialized calcite ($CaCO_3$, SkySpring NanoMat. Inc.) were used as a point of comparison. The synthesis of La and Ce-bastnäsite has been published previously.[53] Surface areas were characterized by

BET analysis of nitrogen gas adsorption. A 3 mM hydroxamic acid solution was prepared by dissolving N-hydroxyoctanamide ($C_8H_{17}NO_2$, Aldrich) in deionized water (pH 5.6). For each measurement, about 10 mg of mineral powder was weighed and placed in the cell of the ITC. The syringe was then filled with hydroxamic acid solution and set up on an auto burette station for titration. When the calorimetric signal was stabilized, the titration experiment was started. The program was set to dose 10 mL of the ligand solution for 15 additions with equilibrium time of 1200 s between each dose. Three series of experiments for each sample were performed. To correct for the effect of the solid-water interaction, the same experiment was conducted using deionized water. The results were used in calculation of binding enthalpy by subtracting the contribution of water interaction.

Results and Discussion

To investigate the vibrational modes of N-octanohydroxamic acid and how those change with complexation, the FTIR spectra of solid N-octanohydroxamic acid and its cerium and lanthanum complexes are shown in Figure 2.3. Peak assignments from Cui et al. were used to aid in the interpretation.[26] A broad O-H stretch band at 2730 cm^{-1} is present in the spectrum of the acid form, but absent in the complexed spectra, indicating that the ligand is deprotonated while complexed with cerium and lanthanum. The acid form shows a band at 3245 cm^{-1}, assigned to N-H stretch, and an N-H bend overtone at 3060 cm^{-1}.[54] This band is broader and less intense when complexed to a metal cation. While the N-H bands are clear in the solid spectra, they are diminished in solution due to H-bond interactions and overlap with the broad O-H stretch band of bulk water, preventing them from being used diagnostically to understand adsorption *in situ*.

Changes in the hydroxamate functional group vibrations are reflected in the region of the spectra between 900 and 1800 cm^{-1}. In the acid form, two

bands corresponding to the C=O (amide I) stretch are shown at 1621cm^{-1} and 1658 cm^{-1}. Complexation with a metal ion shifts these into a single band at a lower frequency.[55] In the cerium and lanthanum salts, this band appears at 1602 and 1599 cm^{-1}, respectively. The C-N stretch and N-H bend combined band at 1561 cm^{-1} in the acid spectrum is also influenced by the complexation, appearing as a broad band centered at 1545 cm^{-1} and 1523 cm^{-1} in the cerium and lanthanum salts, respectively. Since these moieties are strongly affected by complexation with metal ions, the position of these bands while the molecule is adsorbed to bastnäsite is used to determine if an adsorbed complex has been formed at the mineral surface.

To determine the effect of protonation state and hydration on the functional group vibrational modes, spectra of aqueous solutions containing dissolved hydroxamate were measured at several pH; spectra of 10 mM hydroxamate solution from pH 6–11 are shown in Figure 2.4. At pH 6, the protonated hydroxamate shows two C=O stretch peaks: a sharp peak at 1665 cm^{-1} and a smaller peak at 1621 cm^{-1} (similar to the modes in solid acid form of the hydroxamate shown in Figure 2.3). As the pH increases, the intense band at 1665 cm^{-1} shifts to lower wavenumbers, indicating deprotonation of the terminal oxygen. Above the pKa of hydroxamate (about 9.4), the two peaks overlap into a single band centered at about 1624 cm^{-1}. Although deprotonation in solution alters the relative intensity of the C=O stretch band at 1621 cm^{-1}, it does not shift in frequency as seen in the metal complex spectra. The combined N-H bend/C-N stretch band appears as an intense peak at 1531 cm^{-1} in protonated solution. Deprotonation significantly lowers the intensity of this band. A sharp peak at 1465 cm^{-1} is seen in the protonated solution, but diminishes at higher pH, indicating there is a NOH contribution to this band. The FTIR spectra of hydroxamate in solution provide further guidance for interpreting the *in-situ* adsorption spectra. Specifically, physisorption presumably will not significantly alter the hydroxamate functional group vibrational modes, so the spectra of the

ligand will resemble its solution phase spectrum (Figure 2.4). However, if the ligand is chemisorbed via complexation with cerium, its spectrum will appear more like the complex salt (Figure 2.3).

To confirm peak assignment and further aid in the interpretation of these bands, spectra of the ligand were modeled using DFT. Figure 2.5 shows calculated spectra of neutral and deprotonated hydroxamate, as well as its bidentate and monodentate cerium coordination modes. Positions of bands associated with the hydroxamate ligand functional group are summarized in Table 2.1. The computational results show a slight shift in the C=O stretch band to lower frequency in the deprotonated state, and a much larger shift upon bidentate complexation, a trend consistent with the experimental results in Figure 2.3. The coordinated spectrum shifts the C-N stretch band and the associated bending modes to higher frequencies. Experimental spectra show a broad band at 1531 cm^{-1} in solution that is more intense and shifted up to 1545 cm^{-1} in the cerium complex. The DFT calculations support the assignment of this band as a C-N stretch with bending contribution.

DFT calculated spectra can help to understand whether the complexed hydroxamate species measured *in situ* are mono- or bi-dentate. In the spectra calculated with DFT, bidentate coordination shifts the C=O stretch band to a lower frequency whereas a monodentate interaction shifts it significantly higher (Table 2.1). The monodentate coordinated spectrum is the only model which shows the C=O stretch at a higher frequency than the water bending mode. This band provides a distinct difference between the spectra of monodentate and bidentate coordinated hydroxamate. Thus, we can conclude that the spectrum of hydroxamate in monodentate coordination with cerium in solids was not observed experimentally and the data in Figure 2.3 of the complex species are exclusively bidentate.

With these experimental and computational guides, *in-situ* spectra of hydroxamate adsorbed to bastnäsite reveal the mechanism of adsorption.

Results obtained from 1 mM solution at pH 8.5 and 10 are shown in Figure 2.6 and Figure 2.7, respectively. At pH 8.5, a band at 1608 cm^{-1} corresponding to the C=O stretch vibration forms within minutes (Figure 2.6). This band is lower in frequency than solution state hydroxamate, indicating that the ligand has not only been deprotonated but is also forming a bidentate bond to the surface. A broad band corresponding to C-N stretch, CNH, and HNO bending modes appears at 1551 cm^{-1}. The increased frequency of this band relative to the aqueous phase is consistent with complex formation. For solution-phase hydroxamate, the band is at 1531 cm^{-1} (Figure 2.4) but at 1545 cm^{-1} and 1523 cm^{-1} in the cerium and lanthanum salts (Figure 2.3). After 10 min, another band appears at 1654 cm^{-1}, indicating the presence of protonated hydroxamate, as seen in aqueous solution (Figure 2.4). The intensity of this band continues to increase until it exceeds that of the neighboring complexed C=O stretch band. After the initial chemisorption, the appearance of additional bands indicating hydroxamate in the protonated form shows that hydroxamate adsorption is likely exceeding monolayer coverage at 1 mM solution concentration. This result is consistent with the adsorption density measured by solution depletion (Figure 2.2) and previously published adsorption density curves.[7, 8] Based on the frequency of these peaks, the initial monolayer is likely deprotonated and complexed to surface sites, whereas subsequent layers are physisorbed.

Spectra of hydroxamate adsorption at pH 10 show similar behavior (Figure 2.7). The most intense band in the adsorption spectra is the C=O stretch at 1608 cm^{-1}. This peak appears within minutes, along with a broad band at 1550 cm^{-1}, corresponding to the C-N stretch and bending modes. Because the ligand is deprotonated in solution, the contribution of physisorbed molecules is less apparent than in protonated solution. Over time, the C=O stretch band becomes more intense on the higher-wavelength side, and additional band at 1661 cm^{-1} forms. These changes indicate the presence of physisorbed hydroxamate ion. In the deprotonated state, adsorption is aided by electrostatic charge interactions

between the negatively charged ligand and positively charged cation surface sites. For a multi-layer adsorption (beyond two layers) with a deprotonated ligand, however, a counter-ion must be involved to balance charge. Previous work has speculated that dissolved cerium plays that role.[9] In the case of protonated hydroxamate, all that is required is that the ligand's affinity for itself, perhaps driven by the hydrophobicity of the alkyl chains, is strong enough for the molecules to aggregate, forming multilayers.

To examine adsorption of the first monolayer exclusively, the experiments were repeated using more dilute solutions. Figure 2.8 shows spectra of hydroxamate adsorbed to the bastnäsite surface after equilibration with 0.2, 0.4, and 0.6 mM solutions at pH 9. The C=O peak at 1608 cm^{-1} appears narrower than in the higher-concentration adsorption spectra, suggesting less variation in the complexation state and structure of hydroxamate present at the interface. These spectra also show an additional, more intense peak at 1735 cm^{-1}, which is assigned to monodentate-bound hydroxamate based on the DFT modeled spectrum (Figure 2.5). This contrasts with the spectra collected using 1 mM solutions, where the peak at 1735 cm^{-1} is not present, suggesting multilayer adsorption via bidentate complexation. The C-N vibrational band appears at 1545 cm^{-1}, consistent with chemisorbed deprotonated hydroxamate. After an hour of equilibration at each concentration, there is still no significant absorbance between 1620 and 1660 cm^{-1}, which would represent the C=O stretch of physisorbed hydroxamate. This indicates that multilayer adsorption is likely not occurring at these solution concentrations (0.6 mM). To summarize, the FTIR spectra suggest that monodentate chemisorption of hydroxamate is the dominant binding mode to the interface at 0.2, 0.4, and 0.6 mM concentrations, while bidentate chemisorption is favored along with multilayer physisorption at 1 mM concentration.

SFG spectroscopy was used to evaluate the orientation of hydroxamate at the (0001) bastnäsite-aqueous interface. The SFG spectra of the C-H stretch

bands in pH 9 solution at 0.5 mM and 1 mM hydroxamate concentrations are shown in Figure 2.9. The SSP polarized spectra show two bands at 2880 cm^{-1} and 2943 cm^{-1}. These were previously assigned to the CH_3 symmetric stretch and a corresponding Fermi resonance.[8] However, based on the other polarization combinations collected here, we consider these peaks to be composed of an unresolved mixture of CH_3 and CH_2 alkyl symmetric stretches, and a Fermi resonance with the CH_3 asymmetric stretch, respectively. Specifically, the PPP spectrum shows a broad, unresolved band around 2860 cm^{-1} and characteristic dips near 2920 cm^{-1} and 2955 cm^{-1} that correspond to CH_2 and CH_3 asymmetric stretches. Similarly, distinct peaks at 2914 cm^{-1} and 2955 cm^{-1} correspond to CH_2 and CH_3 asymmetric stretches, respectively. These assignments agree with both previous work studying alkyl chains and the SFG selection rules.[30] At both concentrations, the SFG signal from methylene stretches is strong, indicating poor ordering of alkyl chains at the surface. In a well-ordered monolayer, destructive interference from within the tail (i.e., opposing orientations of CH_2 groups in the octyl tail) would reduce the signal from CH_2 groups. This contrasts with previous work utilizing SFG spectra, in which only the SSP polarization combination was collected. Our results indicate that hydroxamate does not appear to form a well packed monolayer at either concentration.

In the PPP and SPS polarized spectra, the alkyl symmetric stretches are combined into a broad, unresolved band around 2860 cm^{-1}. Peaks at 2914 cm^{-1} and 2955 cm^{-1} correspond to CH_2 and CH_3 asymmetric stretches, respectively. The average orientation angle of the methyl group with respect to the interface was determined using the ratios of these band intensities. Assuming an index of refraction of 1.717 for bastnäsite[56] and an interfacial index of refraction of 1.18, based on previous work,[40, 41] the average angle of the terminal methyl group with respect to the surface normal was 20 ± 4° in 0.5 mM solution and 28 ± 4° in 1 mM solution.

The increase in angle with increased solution concentration is consistent with a change from monodentate to bidentate adsorption, as shown in Figure 2.1. However, the higher loading on the surface is likely a greater contributor to the observed angle. As discussed above, at 1mM solution concentration, hydroxamate readily adsorbs in multi-layers, as shown in the FTIR adsorption spectra and indicated by the level of disorder in the SFG data. Because the angle obtained by SFG is an average of all alkyl chains at the surface, this value cannot be attributed to chemisorbed species alone if additional physisorbed molecules are present. Aggregation on the surface could also compress the chemisorbed layer, causing the alkyl chains to lie more parallel to the surface.

Overall, these results show that alkyl hydroxamate readily chemisorbs to the bastnäsite surface, making it a good candidate for bastnäsite flotation. However, good selectivity for an REE mineral also requires a low adsorption affinity for gangue minerals, of which calcite will be used as a common representative. In contrast to the measured ATR-FTIR spectra of alkyl hydroxamate on the bastnäsite surface, adsorption was not detected at the calcite interface under the same conditions. This is consistent with lower adsorption densities measured on calcite (Figure 2.2) and reported in the literature.[7-9] These results suggest that alkyl hydroxamate binds more strongly to bastnäsite than to calcite, which would make it a desirable collector molecule.

To confirm that alkyl hydroxamate binds more strongly to bastnäsite than calcite surfaces, the interaction enthalpies of La and Ce-bastnäsites and calcite with 3 mM hydroxamic acid (ΔH_{int}) were measured by ITC. These measurements are plotted in Figure 2.10 and summarized in Table 2.2. Figure 2.11 and Table 2.3 show the results of the water correction for each mineral, related to the hydration energy and solvation effects. The data (Table 2.3) show that La and Ce-bastnasite have stronger adsorption of water on the surface than calcite. The overall interaction enthalpies after subtracting water correction are 0.92, 0.19, and 0.02 kJ per mole of the $LaFCO_3$, $CeFCO_3$ and $CaCO_3$ respectively (Table

2.4). The last value is essentially zero within experimental error. A similar trend in binding enthalpies is observed with and without the water correction (Table 2.2 and Table 2.4, respectively). The water-corrected values in terms of surface area of the solid phase are 0.06, 0.04 and 0.01 J/m^2 for the three materials (Table 2.4).

Enthalpy values per mole of adsorbed ligand could not be calculated because the actual amount of hydroxamate adsorbed on the mineral surface is unknown. The interaction enthalpy becomes less exothermic in the sequence $LaFCO_3$ > $CeFCO_3$ > $CaCO_3$, which suggests $LaFCO_3$ and $CeFCO_3$ have substantially more favorable interaction with hydroxamic acid than calcite. This confirms the finding from the ATR-FTIR spectra that hydroxamate species bind to bastnäsite more strongly than calcite. Moreover, the stronger interaction with lanthanum bastnäsite compared to cerium bastnäsite suggests that the hydroxamate species is bound to cationic surface sites (e.g., cerium or lanthanum) and that sorption is highly cation-specific, raising the possibility that further improvements in ligand design could be made depending on the REE of interest that is targeted. This specificity may potentially be utilized to separate various REE.

Summary and Conclusions

In-situ FTIR spectra of octanohydroxamic acid adsorbed to bastnäsite show chemisorption in both monodentate and bidentate forms. The preferred mechanism depends on concentration: the monodentate mechanism is dominant at low surface loading, whereas the bidentate species is more prominent at higher concentrations. DFT calculations of the hydroxamate vibrational modes support the peak assignments in the observed spectra. SFG measurements of hydroxamate adsorption in 0.5 mM and 1.0 mM solutions show the alkyl chains are slightly more parallel to the surface at higher concentration, supporting the

change from monodentate to bidentate adsorption. Deprotonation of the ligand occurs to facilitate chemisorption regardless of the solution pH. Additional layers are physisorbed, retaining their bulk-like protonation state. The binding enthalpies of La and Ce-bastnäsite with hydroxamic acid are exothermic and stronger than for calcite.

These results have direct implications for the beneficiation of bastnäsite by alkyl hydroxamate ligands. Because hydroxamate does not need to be deprotonated in solution to chemisorb, selectivity may be maximized at pH values where adsorption to calcite is poor. Previous work by Pradip and Fuerstenau[45] showed little variation in the flotation recovery of pure bastnäsite with 0.3 mM octyl hydroxamate between pH 5 and 9, while calcite recovery sharply declined below pH 9. Our findings support the authors' prediction that selectivity for bastnäsite would be achieved at pH values below the pKa of hydroxamate.

While previous work has primarily cited bidentate chelation as the mechanism for hydroxamate chemisorption,[7-9, 13] our results show that the monodentate conformation also plays a significant role in adsorption on the bastnäsite surface. To avoid micelle formation and adsorption to gangue ores, flotation may be more effective at low hydroxamate concentrations. This is supported by microflotation experiments conducted at pH 9 by Pradip and Fuerstenau,[45] in which both bastnäsite and calcite were fully recovered at concentrations greater than 0.5 mM, while calcite recovery was much lower than bastnäsite at 0.3 mM. Although hydroxamate chelates more strongly with cerium ions than calcium ions, both reactions occur readily at pH 9, resulting in poor selectivity. Calcite recovery may be reduced by changing the pH, but increasing the ligand concentration under any condition would inevitably cause more calcite to float. Since hydroxamate adsorption onto bastnäsite occurs via bidentate chemisorption only at high surface coverages, the stability gained by chelation would be offset by poor rejection of calcite. To induce greater selectivity for

bastnäsite, a ligand that forms a bidentate complex at low surface coverages might be conceived.

References

1. Humphries, M., Rare earth elements: the global supply chain. *Congressional Research Service* **2012**, 7-5700.
2. Tunsu, C.; Petranikova, M.; Gergorić, M.; Ekberg, C.; Retegan, T., Reclaiming rare earth elements from end-of-life products: A review of the perspectives for urban mining using hydrometallurgical unit operations. *Hydrometallurgy* **2015,** *156*, 239-258.
3. Wall, F. R., Alain; Pell, Robert S. , Responsible Sourcing of Critical Metals. *Elements* **2017,** *13* (5), 313-318.
4. Castor, S. B.; Hedrick, J. B., Rare earth elements. *Industrial minerals volume, 7th edition: Society for mining, metallurgy, and exploration, Littleton, Colorado* **2006**, 769-792.
5. Jordens, A.; Cheng, Y. P.; Waters, K. E., A review of the beneficiation of rare earth element bearing minerals. *Minerals Engineering* **2013,** *41*, 97-114.
6. Nagaraj, D.; Farinato, R., Evolution of flotation chemistry and chemicals: A century of innovations and the lingering challenges. *Minerals Engineering* **2016,** *96*, 2-14.
7. Pradip; Fuerstenau, D., The adsorption of hydroxamate on semi-soluble minerals. Part I: Adsorption on barite, Calcite and Bastnaesite. *Colloids and Surfaces* **1983,** *8* (2), 103-119.
8. Zhang, X.; Du, H.; Wang, X. M.; Miller, J. D., Surface chemistry aspects of bastnaesite flotation with octyl hydroxamate. *International Journal of Mineral Processing* **2014,** *133*, 29-38.
9. Jordens, A.; Marion, C.; Kuzmina, O.; Waters, K. E., Surface chemistry considerations in the flotation of bastnäsite. *Minerals Engineering* **2014,** *66*, 119-129.
10. Pradip; Fuerstenau, D., Adsorption of hydroxamate collectors on semisoluble minerals Part II: effect of temperature on adsorption. *Colloids and Surfaces* **1985,** *15*, 137-146.
11. Pavez, O.; Brandao, P.; Peres, A., Technical note adsorption of oleate and octyl-hydroxamate on to rare-earths minerals. *Minerals Engineering* **1996,** *3* (9), 357-366.
12. Zhang, W.; Honaker, R., A fundamental study of octanohydroxamic acid adsorption on monazite surfaces. *International Journal of Mineral Processing* **2017,** *164*, 26-36.
13. Fuerstenau, D. W.; Pradip, A Century of Research Leading to Understanding the Scientific Basis of Selective Mineral Flotation and Design of Flotation Collectors. *Mining, Metallurgy & Exploration* **2019,** *36* (1), 3-20.
14. Srinivasan, S. G.; Shivaramaiah, R.; Kent, P. R.; Stack, A. G.; Riman, R.; Anderko, A.; Navrotsky, A.; Bryantsev, V. S., A comparative study of surface energies and water adsorption on Ce-bastnäsite, La-bastnäsite, and calcite via

density functional theory and water adsorption calorimetry. *Physical Chemistry Chemical Physics* **2017,** *19* (11), 7820-7832.
15. Sreenivas, T.; Padmanabhan, N., Surface chemistry and flotation of cassiterite with alkyl hydroxamates. *Colloids and Surfaces A: Physicochemical and Engineering Aspects* **2002,** *205* (1), 47-59.
16. Yang, J.; Bremer, P. J.; Lamont, I. L.; McQuillan, A. J., Infrared spectroscopic studies of siderophore-related hydroxamic acid ligands adsorbed on titanium dioxide. *Langmuir* **2006,** *22* (24), 10109-10117.
17. Hind, A. R.; Bhargava, S. K.; McKinnon, A., At the solid/liquid interface: FTIR/ATR - the tool of choice. *Advances in Colloid and Interface Science* **2001,** *93*, 91-114.
18. Krumina, L.; Kenney, J. P.; Loring, J. S.; Persson, P., Desorption mechanisms of phosphate from ferrihydrite and goethite surfaces. *Chemical Geology* **2016,** *427*, 54-64.
19. Parikh, S. J.; Chorover, J., ATR-FTIR study of lipopolysaccharides at mineral surfaces. *Colloids and Surfaces B: Biointerfaces* **2008,** *62* (2), 188-198.
20. Yoon, T. H.; Johnson, S. B.; Musgrave, C. B.; Brown, G. E., Adsorption of organic matter at mineral/water interfaces: I. ATR-FTIR spectroscopic and quantum chemical study of oxalate adsorbed at boehmite/water and corundum/water interfaces. *Geochimica et Cosmochimica Acta* **2004,** *68* (22), 4505-4518.
21. Borer, P.; Hug, S. J.; Sulzberger, B.; Kraemer, S. M.; Kretzschmar, R., ATR-FTIR spectroscopic study of the adsorption of desferrioxamine B and aerobactin to the surface of lepidocrocite (γ-FeOOH). *Geochimica et Cosmochimica Acta* **2009,** *73* (16), 4661-4672.
22. Li, F.; Zhong, H.; Xu, H.; Jia, H.; Liu, G., Flotation behavior and adsorption mechanism of α-hydroxyoctyl phosphinic acid to malachite. *Minerals Engineering* **2015,** *71*, 188-193.
23. Beattie, D. A.; Addai-Mensah, J.; Beaussart, A.; Franks, G. V.; Yeap, K.-Y., In situ particle film ATR FTIR spectroscopy of poly (N-isopropyl acrylamide)(PNIPAM) adsorption onto talc. *Physical Chemistry Chemical Physics* **2014,** *16* (45), 25143-25151.
24. Azizi, D.; Larachi, F.; Latifi, M., Ionic-liquid collectors for rare-earth minerals flotation--Case of tetrabutylammonium bis (2-ethylhexyl)-phosphate for monazite and bastnäsite recovery. *Colloids and Surfaces A: Physicochemical and Engineering Aspects* **2016,** *506*, 74-86.
25. Sarvaramini, A.; Azizi, D.; Larachi, F., Hydroxamic acid interactions with solvated cerium hydroxides in the flotation of monazite and bastnäsite—experiments and DFT study. *Applied Surface Science* **2016,** *387*, 986-995.
26. Cui, J.; Hope, G. A.; Buckley, A. N., Spectroscopic investigation of the interaction of hydroxamate with bastnaesite (cerium) and rare earth oxides. *Minerals Engineering* **2012,** *36*, 91-99.

27. Tian, C.; Shen, Y., Recent progress on sum-frequency spectroscopy. *Surface Science Reports* **2014,** *69* (2), 105-131.
28. Shen, Y., Phase-sensitive sum-frequency spectroscopy. *Annual review of physical chemistry* **2013,** *64*, 129-150.
29. Shen, Y., Basic theory of surface sum-frequency generation. *The Journal of Physical Chemistry C* **2012,** *116* (29), 15505-15509.
30. Wang, H.-F.; Gan, W.; Lu, R.; Rao, Y.; Wu, B.-H., Quantitative spectral and orientational analysis in surface sum frequency generation vibrational spectroscopy (SFG-VS). *International Reviews in Physical Chemistry* **2005,** *24* (2), 191-256.
31. Wang, H.-F., Sum frequency generation vibrational spectroscopy (SFG-VS) for complex molecular surfaces and interfaces: Spectral lineshape measurement and analysis plus some controversial issues. *Progress in Surface Science* **2016,** *91* (4), 155-182.
32. Doughty, B.; Yin, P.; Ma, Y.-Z., Adsorption, Ordering, and Local Environments of Surfactant-Encapsulated Polyoxometalate Ions Probed at the Air–Water Interface. *Langmuir* **2016,** *32* (32), 8116-8122.
33. Voylov, D. N.; Holt, A. P.; Doughty, B.; Bocharova, V.; Meyer III, H. M.; Cheng, S.; Martin, H.; Dadmun, M.; Kisliuk, A.; Sokolov, A. P., Unraveling the Molecular Weight Dependence of Interfacial Interactions in Poly (2-vinylpyridine)/Silica Nanocomposites. *ACS Macro Letters* **2017,** *6* (2), 68-72.
34. Han, H. L.; Melaet, G.; Alayoglu, S.; Somorjai, G. A., In Situ Microscopy and Spectroscopy Applied to Surfaces at Work. *ChemCatChem* **2015,** *7* (22), 3625-3638.
35. Kweskin, S.; Rioux, R.; Song, H.; Komvopoulos, K.; Yang, P.; Somorjai, G., High-Pressure Adsorption of Ethylene on Cubic Pt Nanoparticles and Pt (100) Single Crystals Probed by in Situ Sum Frequency Generation Vibrational Spectroscopy. *ACS Catalysis* **2012,** *2* (11), 2377-2386.
36. Thompson, C. M.; Carl, L. M.; Somorjai, G. A., Sum frequency generation study of the interfacial layer in liquid-phase heterogeneously catalyzed oxidation of 2-propanol on platinum: effect of the concentrations of water and 2-propanol at the interface. *The Journal of Physical Chemistry C* **2013,** *117* (49), 26077-26083.
37. Bordenyuk, A. N.; Weeraman, C.; Yatawara, A.; Jayathilake, H. D.; Stiopkin, I.; Liu, Y.; Benderskii, A. V., Vibrational sum frequency generation spectroscopy of dodecanethiol on metal nanoparticles. *The Journal of Physical Chemistry C* **2007,** *111* (25), 8925-8933.
38. Jayathilake, H. D.; Driscoll, J. A.; Bordenyuk, A. N.; Wu, L.; da Rocha, S. R.; Verani, C. N.; Benderskii, A. V., Molecular Order in Langmuir− Blodgett Monolayers of Metal− Ligand Surfactants Probed by Sum Frequency Generation. *Langmuir* **2009,** *25* (12), 6880-6886.
39. Rao, Y.; Comstock, M.; Eisenthal, K. B., Absolute orientation of molecules at interfaces. *The Journal of Physical Chemistry B* **2006,** *110* (4), 1727-1732.

40. Doughty, B.; Goverapet Srinivasan, S.; Bryantsev, V. S.; Lee, D.; Lee, H. N.; Ma, Y.-Z.; Lutterman, D. A., Absolute Molecular Orientation of Isopropanol at Ceria (100) Surfaces: Insight into Catalytic Selectivity from Interfacial Structure. *The Journal of Physical Chemistry C* **2017**.
41. Tan, S.; Gray, M. B.; Kidder, M. K.; Cheng, Y.; Daemen, L. L.; Lee, D.; Lee, H. N.; Ma, Y.-Z.; Doughty, B.; Lutterman, D. A., Insight into the Selectivity of Isopropanol Conversion at Strontium Titanate (100) Surfaces: A Combination Kinetic and Spectroscopic Study. *ACS Catalysis* **2017,** *7* (12), 8118-8129.
42. Jang, J. H.; Lydiatt, F.; Lindsay, R.; Baldelli, S., Quantitative Orientation Analysis by Sum Frequency Generation in the Presence of Near-Resonant Background Signal: Acetonitrile on Rutile TiO2 (110). *The Journal of Physical Chemistry A* **2013,** *117* (29), 6288-6302.
43. Benoit, P.; Hering, J. G.; Stumm, W., Comparative study of the adsorption of organic ligands on aluminum oxide by titration calorimetry. *Applied geochemistry* **1993,** *8* (2), 127-139.
44. Davis, J. A.; Gloor, R., Adsorption of dissolved organics in lake water by aluminum oxide. Effect of molecular weight. *Environmental science & technology* **1981,** *15* (10), 1223-1229.
45. Pradip; Fuerstenau, D., The role of inorganic and organic reagents in the flotation separation of rare-earth ores. *International Journal of Mineral Processing* **1991,** *32* (1-2), 1-22.
46. Frisch, M. J.; Trucks, G. W.; Schlegel, H. B.; Scuseria, G. E.; Robb, M. A.; Cheeseman, J. R.; Scalmani, G.; Barone, V.; Petersson, G. A.; Nakatsuji, H.; Li, X.; Caricato, M.; Marenich, A. V.; Bloino, J.; Janesko, B. G.; Gomperts, R.; Mennucci, B.; Hratchian, H. P.; Ortiz, J. V.; Izmaylov, A. F.; Sonnenberg, J. L.; Williams; Ding, F.; Lipparini, F.; Egidi, F.; Goings, J.; Peng, B.; Petrone, A.; Henderson, T.; Ranasinghe, D.; Zakrzewski, V. G.; Gao, J.; Rega, N.; Zheng, G.; Liang, W.; Hada, M.; Ehara, M.; Toyota, K.; Fukuda, R.; Hasegawa, J.; Ishida, M.; Nakajima, T.; Honda, Y.; Kitao, O.; Nakai, H.; Vreven, T.; Throssell, K.; Montgomery Jr., J. A.; Peralta, J. E.; Ogliaro, F.; Bearpark, M. J.; Heyd, J. J.; Brothers, E. N.; Kudin, K. N.; Staroverov, V. N.; Keith, T. A.; Kobayashi, R.; Normand, J.; Raghavachari, K.; Rendell, A. P.; Burant, J. C.; Iyengar, S. S.; Tomasi, J.; Cossi, M.; Millam, J. M.; Klene, M.; Adamo, C.; Cammi, R.; Ochterski, J. W.; Martin, R. L.; Morokuma, K.; Farkas, O.; Foresman, J. B.; Fox, D. J. *Gaussian 16*, Wallingford, CT, 2016.
47. Perdew, J. P.; Burke, K.; Ernzerhof, M., Generalized Gradient Approximation Made Simple. *Physical Review Letters* **1996,** *77* (18), 3865-3868.
48. Dolg, M.; Stoll, H.; Savin, A.; Preuss, H., Energy-adjusted pseudopotentials for the rare earth elements. *Theoretical Chemistry Accounts: Theory, Computation, and Modeling (Theoretica Chimica Acta)* **1989,** *75* (3), 173-194.

49. Grimme, S.; Antony, J.; Ehrlich, S.; Krieg, H., A consistent and accurate ab initio parametrization of density functional dispersion correction (DFT-D) for the 94 elements H-Pu. *The Journal of chemical physics* **2010,** *132* (15), 154104.
50. Merrick, J. P.; Moran, D.; Radom, L., An evaluation of harmonic vibrational frequency scale factors. *The Journal of Physical Chemistry A* **2007,** *111* (45), 11683-11700.
51. https://www.chemcraftprog.com/.
52. Watson, B. R.; Ma, Y.-Z.; Cahill, J. F.; Doughty, B.; Calhoun, T. R., Probing ligand removal and ordering at quantum dot surfaces using vibrational sum frequency generation spectroscopy. *Journal of colloid and interface science* **2019,** *537*, 389-395.
53. Shivaramaiah, R.; Anderko, A.; Riman, R. E.; Navrotsky, A., Thermodynamics of bastnaesite: A major rare earth ore mineral. *American Mineralogist* **2016,** *101* (5), 1129-1134.
54. Hope, G. A.; Woods, R.; Buckley, A. N.; White, J. M.; McLean, J., Spectroscopic characterisation of n-octanohydroxamic acid and potassium hydrogen n-octanohydroxamate *Inorganica Chimica Acta* **2010,** (363), 935-943.
55. Higgins, F. S.; Magliocco, L. G.; Colthup, N. B., Infrared and Raman spectroscopy study of alkyl hydroxamic acid and alkyl hydroxamate isomers. *Applied spectroscopy* **2006,** *60* (3), 279-287.
56. Anthony, J. W.; Bideaux, R. A.; Bladh, K. W.; Nichols, M. C., Handbook of Mineralogy, Mineralogical Society of America, Chantilly, VA 20151-1110, USA. 2011.

Appendix

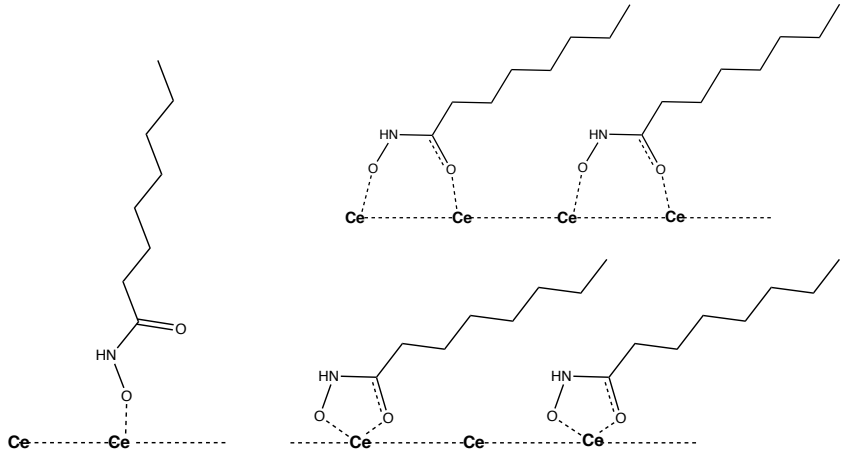

Figure 2.1: Hypothesized mechanisms for hydroxamic acid chemisorption to the surface of bastnäsite.

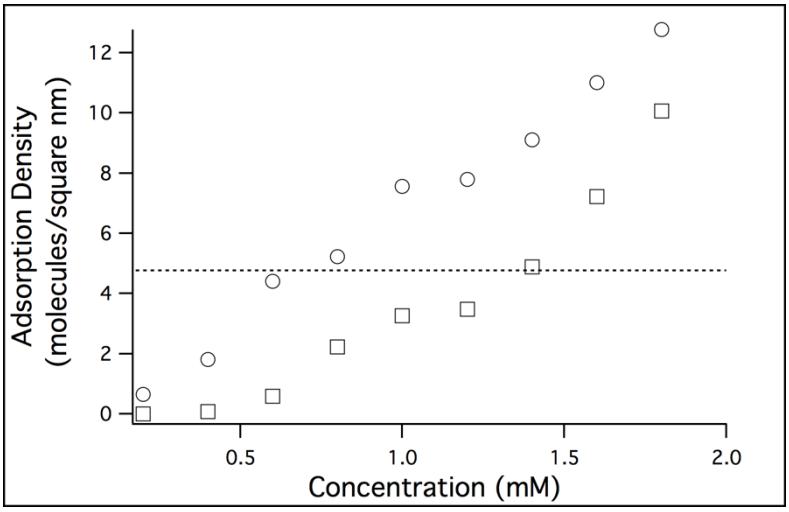

Figure 2.2: Octyl Hydroxamic Acid Adsorption Isotherm.

Adsorption density onto bastnäsite (circles) and calcite (squares). The dotted line corresponds to the adsorption density of a vertically oriented monolayer of hydroxamate molecules.

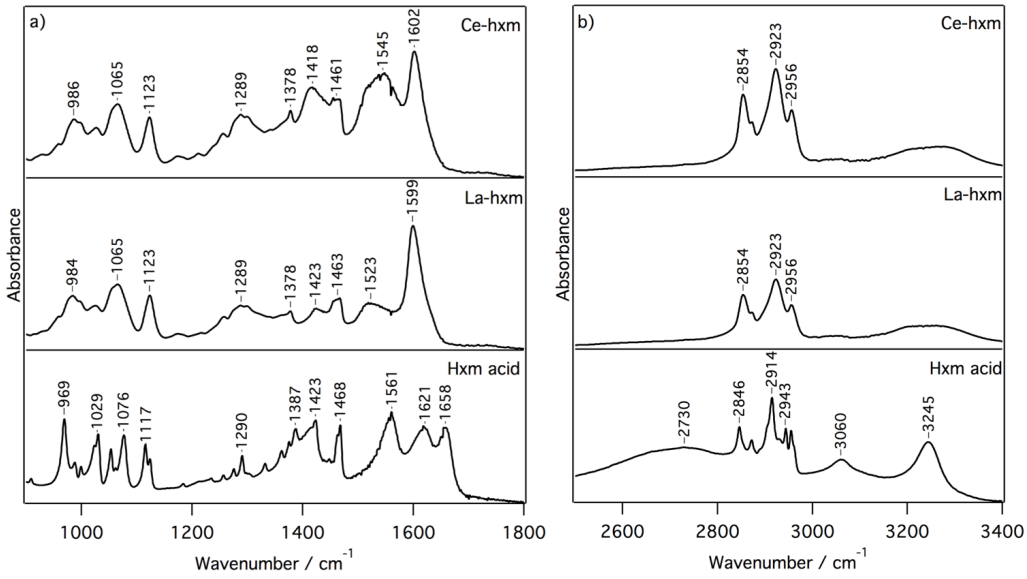

Figure 2.3: FTIR spectra of solid Ce-hydroxamate, La-hydroxamate, and hydroxamic acid.

The fingerprint region of 900-1800 cm^{-1} in (a) shows functional group vibrational modes that change with complexation, particularly ~1500-1650 cm^{-1}. In contrast, bands corresponding to alkyl chain vibrations show little change.

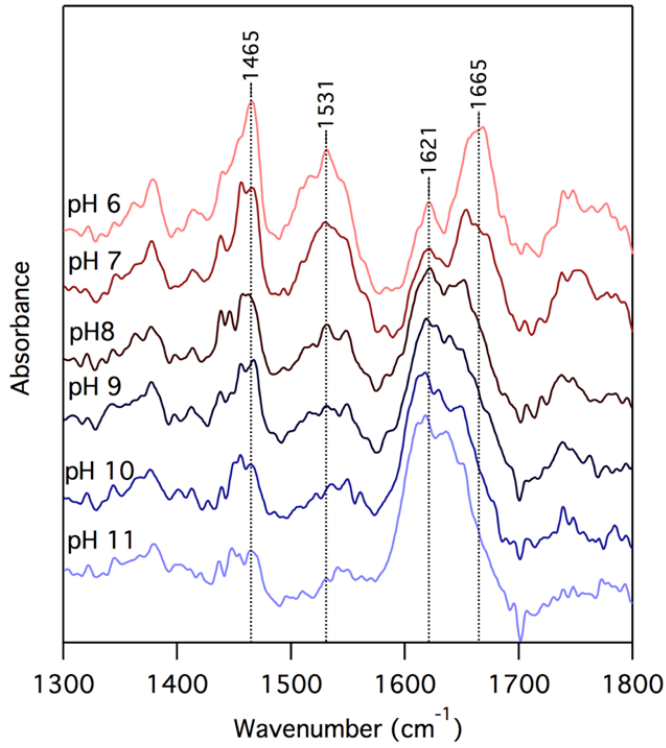

Figure 2.4: FTIR spectra of aqueous hydroxamate at pH 6-11.

In neutral form, the ligand shows two C=O stretch bands at 1621 cm^{-1} and 1665 cm^{-1}. When the ligand is deprotonated, these combine into a single, intense band at 1624 cm^{-1}.

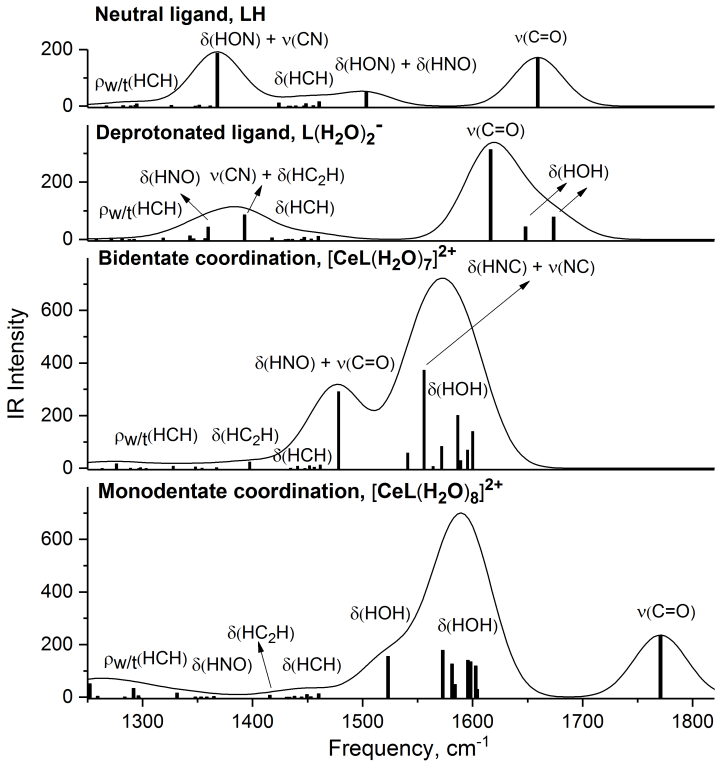

Figure 2.5: Simulated IR spectra and band assignment for a hydroxamic acid collector

Vibrational frequencies were computed in the neutral, deprotonated, and metal bound (deprotonated) bidentate and monodentate coordination forms. The contour of spectral lines is calculated using Gaussian broadening.

Table 2.1: Calculated and experimental frequencies of hydroxamate functional group vibrational modes.

	DFT Calculated (cm^{-1})				Experimental (cm^{-1})			
	Neutral	Deprot.	Bident. Complex	Monodent. Complex	Solid Acid	Solid Ce Complex	Aqueous Prot.	Aqueous Deprot.
N-O str.					969	986		
NOH bend	1368				1423		1465	
C-N str + CNH bend	1368	1393	1575	1590	1561	1545	1531	1536
HNO bend	1503	1360	1475	1331		1418		
C=O str.	1659	1620	1475	1770	1621, 1658	1602	1621, 1665	1624

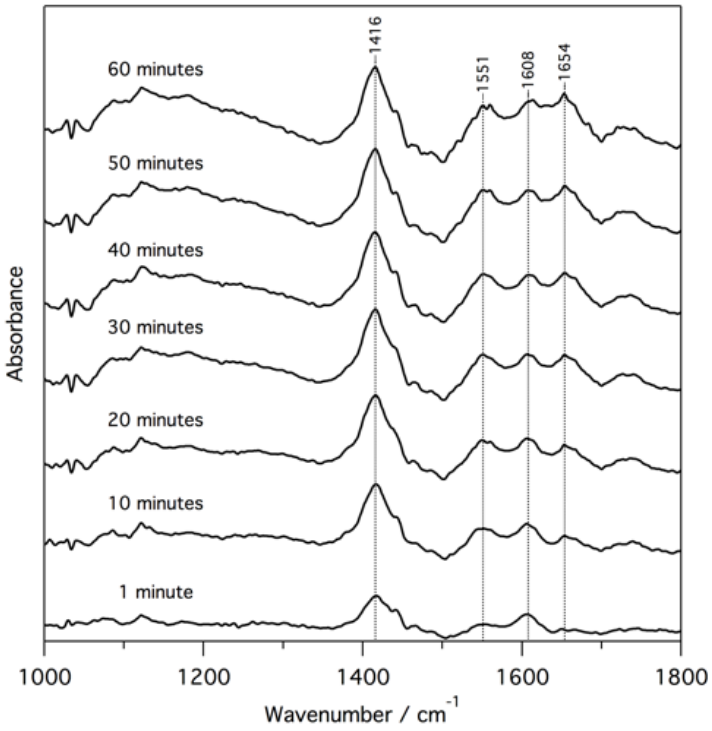

Figure 2.6: ATR-FTIR difference spectra of adsorption of hydroxamate onto bastnäsite at pH 8.5 (1 mM).

The peak 1608 cm^{-1} corresponds to chemisorbed hydroxamate. The appearance of an additional peak at 1654 cm^{-1} shows the formation of additional physisorbed hydroxamate.

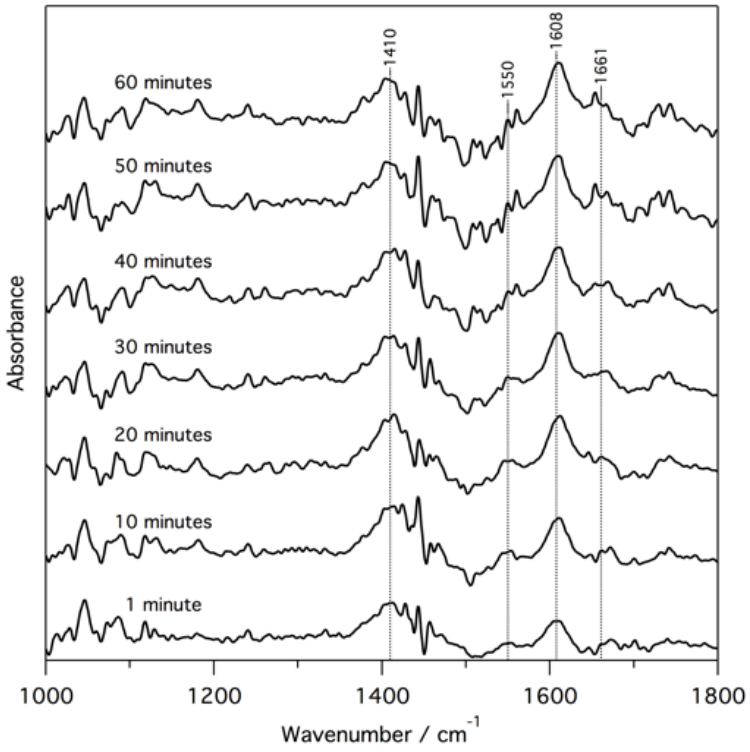

Figure 2.7: Adsorption of hydroxamate onto bastnäsite at pH 10 (1 mM).

A peak at 1608 cm^{-1} appears within a minute, showing rapid chemisorption.

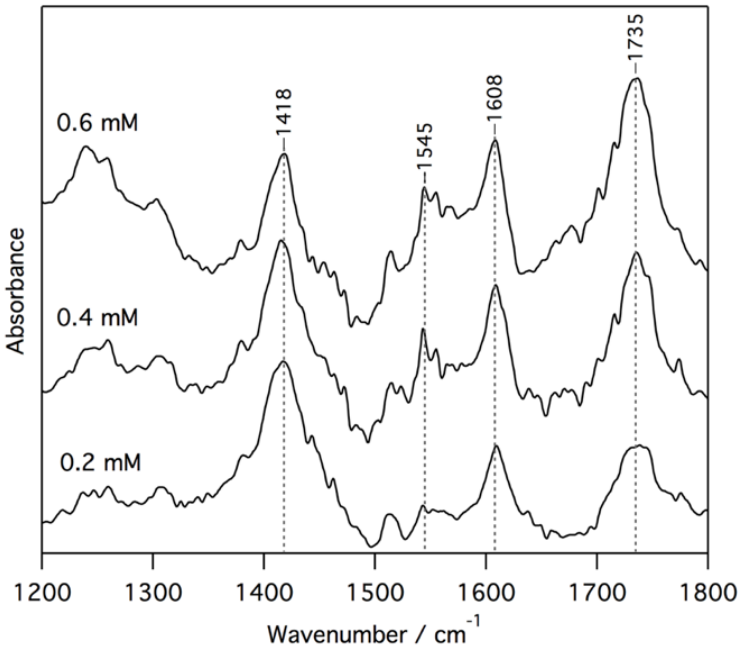

Figure 2.8: FTIR of hydroxamate adsorption onto bastnäsite at 0.6, 0.4, 0.2 mM.

An additional peak at 1735 cm^{-1} in these spectra corresponds to monodentate-coordinated hydroxamate.

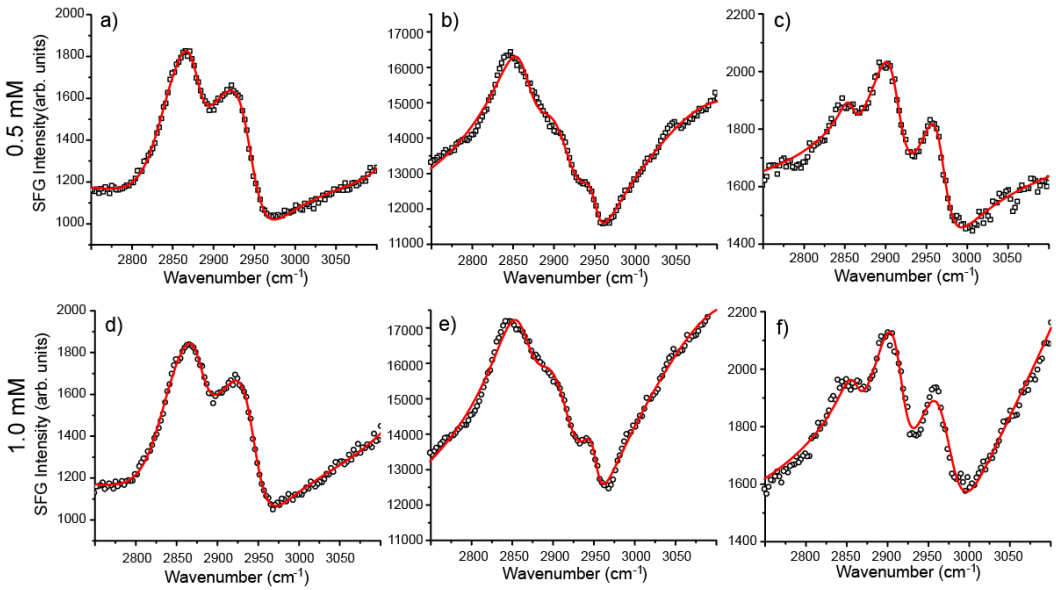

Figure 2.9: SFG spectra from hydroxamate at the bastnäsite-aqueous interface.

Figures a)-c) are for a 0.5 mM solution, whereas d)-f) are from a 1 mM solution. a) and d) show the SSP polarization combination, b) and e) are the PPP, and c) and f) are SPS. Points are measured data and solid red lines are fits based on Equation 2.3.

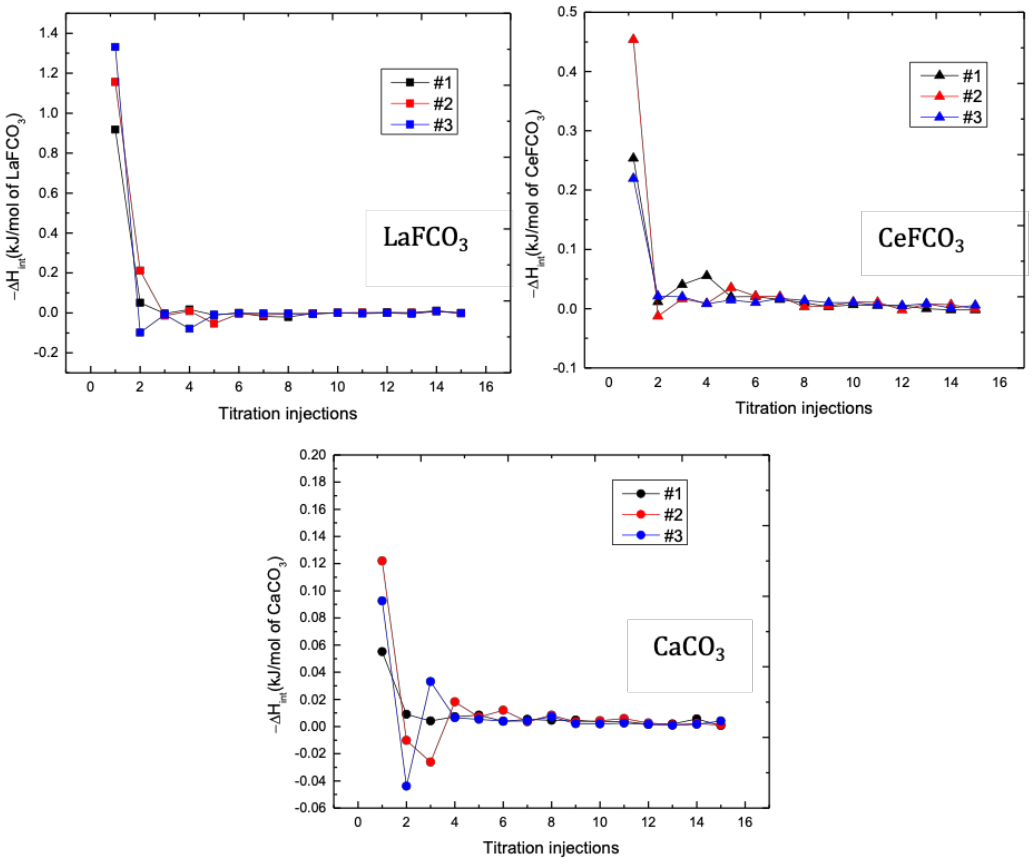

Figure 2.10: Interaction enthalpies of synthetic bastnäsite and calcite with hydroxamic acid

Each trial used15 injections (10 μL) of 3 mM hydroxamic acid.

Table 2.2: Interaction enthalpy (ΔH_{int}) of minerals with 3mM hydroxamic acid

Material	ΔH_{int}(kJ/mol of mineral)	ΔH_{int}(kJ/mol of acid)
La-bastnasite ($LaFCO_3$)	-1.12(3) ±0.173	-107.96 ±24.50
Ce-bastnasite ($CeFCO_3$)	-0.47(3) ±0.109	-43.53 ±11.40
Calcite ($CaCO_3$)	-0.12(3) ±0.026	-29.95 ±6.06

* Number in () means number of the experimental trials

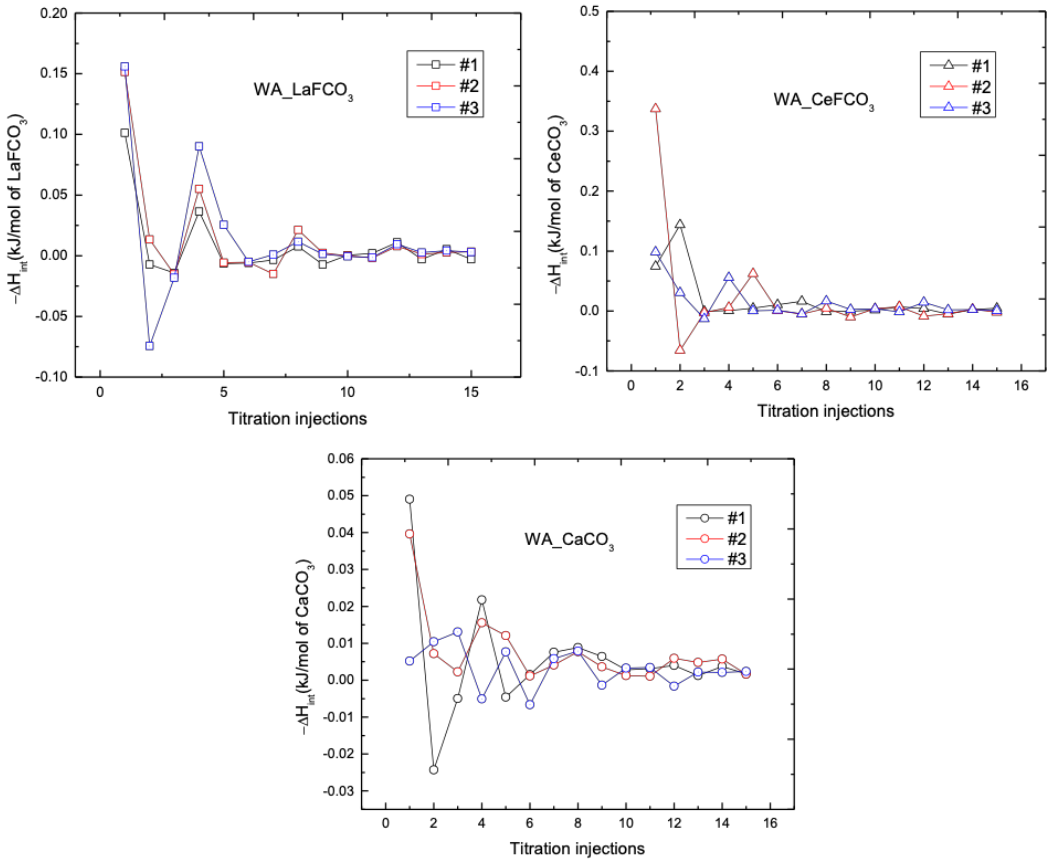

Figure 2.11: Interaction enthalpies of bastnäsite and calcite with water

3 trials were conducted on each solid using 15 injections (10μL) of water to calculate water correction for hydroxamic acid results.

Table 2.3: Interaction enthalpy (ΔH_{int}) of minerals with water

Materials	**ΔH_{int}(kJ/mol of mineral)**
$CeFCO_3$	- 0.28(3) ±0.05
$LaFCO_3$	- 0.20(3) ±0.06
$CaCO_3$	- 0.10(3) ±0.03

Table 2.4: Interaction enthalpy (ΔH_{int}) of different minerals with hydroxamic acid (3 mM) after water correction

Materials	ΔH_{int} (kJ/mol of mineral)	ΔH_{int} (kJ/mol of acid)	SA (m^2/g)	ΔH_{int} (J/m^2 of surface)
$LaFCO_3$	-0.92 ±0.18	-138.06 ±31.33	67.13[a]	-0.064 ±0.012
$CeFCO_3$	-0.19 ±0.13	-69.79 ±39.28	21.5[a]	-0.041 ±0.027
$CaCO_3$	-0.02 ±0.04	-31.10 ±25.44	22.41[a]	-0.010 ±0.017

[a] Data from Shivaramaiah [49]

CHAPTER 3
RELATIONSHIP BETWEEN LIGAND STRUCTURE AND REACTIVITY

Findings from this chapter were included in two separate publications.

The three ligands in the first section (salicylic acid, benzohydroxamic acid, and salicylhydroxamic acid) are part of a manuscript submitted by Robert C. Chapelski, Jr.:

Chapelski, R.; Chowdhury, A.U.; Wanhala, A.K.; Bocharova, V.; Roy,S; Keller, P.C.; Everly, D.; Jansone-Popova, S.; Kisliuk, A.; Sacci, R.L.; Stack, A.G.; Anderson, C.G.; Doughty, B.; Bryantsev, V.S., Thinking Small to Avoid Large Losses: a Molecular-Scale Approach to Rare-Earth Beneficiation. *iScience* **2020**.

This manuscript is currently under review. Anna K. Wanhala designed and conducted all Fourier transform infrared spectroscopic measurements presented in this publication, including analysis of the results.

The second section of this chapter concerns three phosphinic acid ligands. The results of this analysis were published by Jonathon E. Sutton:

Sutton, J. E.; Roy, S.; Chowdhury, A. U.; Wu, L.; Wanhala, A. K.; De Silva, N.; Jansone-Popova, S.; Hay, B. P.; Cheshire, M. C.; Windus, T. L., Molecular Recognition at Mineral Interfaces: Implications for the Beneficiation of Rare Earth Ores. *ACS Applied Materials & Interfaces* **2020,** *12* (14), 16327-16341.

Anna K. Wanhala designed and conducted Fourier transform infrared spectroscopic measurements for this publication, presented in this chapter.

Abstract

Separating bastnäsite, from unwanted gangue in mined ores relies on the selective binding of collector molecules at the mineral interface to facilitate froth flotation. While empirical tests of adsorption affinity (adsorption isotherms) and flotation performance (microflotation) help to validate the selectivity of collector ligands, they provide little information about the factors that influence selectivity. In this work, several ligands have been chosen with varying polar functional groups and nonpolar tails. Salicylhydroxamic acid, a ligand which performed well in microflotation tests, is compared with two analogs to elucidate the role of neighboring functional groups in the adsorption reaction. ATR-FTIR is employed as part of a collaborative investigation with Raman and SFG spectroscopies, as well as isothermal titration calorimetry, to test binding orientations predicted by DFT computations.

In a second study, three ligands with identical phosphinic acid functional groups are compared to evaluate the effect of ligand structure on binding. A monophosphinic acid is compared with two bis-phosphinic ligands, predicted to preferentially adsorb to bastnäsite by molecular modeling. Both bis-phosphinic ligands outperform the monophosphinic species, highlighting the potential for using molecular recognition to design ligands which target specific surfaces. By determining the mechanisms by which these ligands adsorb to bastnäsite, the relationship between structure and reactivity can be better characterized. This will allow for more strategic development of flotation collectors.

Introduction

Following the advent of froth flotation, a general formula for flotation collectors was quickly established. By 1920, researchers began to focus on the process of collector adsorption as a route to selectively separate minerals by surface charge. Ligands containing ionic functional groups revealed a strong

preference for charged mineral surfaces, such as calcite, rather than uncharged surfaces such as glass.[1] Further studies evaluated the role of ligands in inducing hydrophobicity. While adsorption experiments showed similar quantities of collectors with the same functional group, only collectors with nonpolar groups attached caused particles to float into the froth.[2] As a result of this early work, amphiphilic ligands—featuring a polar functional group with a nonpolar tail—became the standard for flotation collectors.

Countless molecules can be conceived following these criteria. Systematic investigations have revealed some ways in which collector structure influences flotation outcomes. In many cases, these studies have either focused on hydrophobicity—as a function of the size and shape of the hydrophobic tail[3, 4]—or selectivity of different polar functional groups.[5] In practice, however, advancements in froth flotation have largely come through trial-and-error attempts, guided by intuition and industry standards.[6, 7] In a 2007 review of flotation reagents, Nagaraj and Ravishankar[8] presented a broad range of possible flotation collectors, but asserted that 90% of nonsulfide mineral separations utilized either fatty acid or amine collectors.

The search for more efficient collectors could benefit immensely from the application of modern computational tools.[9] Empirical tests of various collectors are limited simply by the time and resources required to test each one. Molecular modeling tools have the potential to predict which ligand structures may be effective.[10-12] To boost the efficacy of these computational searches, predicted ligand interactions on mineral surfaces can be tested experimentally. Furthermore, a detailed characterization of how certain aspects of ligand structure influence reactivity could create a framework for developing ligands with specific adsorption behavior.

Variables influencing collector performance

Molecular structure has been shown to influence the performance of collectors with varying functional groups.[13] Fuerstenau, Herrera-Urbina, and McGlashan[14] evaluated the effect of several chelating ligands on the wettability of various copper minerals. Contact angles measured following collector adsorption varied significantly not only between minerals but also between collectors with the same chelating group. The authors concluded that ligands containing aromatic rings were both less soluble in water and less effective at inducing surface hydrophobicity than ligands with long alkyl chains.

A review by Marabini[4] also states that chelates with alkyl chains are more hydrophobic. However, aromatic rings improve the stability of chelates, and consequently the functional group selectivity. The influence of these competing phenomena would not be apparent in the results of microflotation experiments, but a fundamental understanding of their effects led to the development of mixed aromatic-aliphatic collectors.

Several effects of chemical structure on functional group reactivity are evident in the acidity of salicylic acid, shown in Figure 3.1. Lone pair electrons from the hydroxyl group donate electronegativity to the ring, which makes the carboxylic acid more negatively charged through conjugation. This could be expected to decrease the acidity of salicylic acid relative to benzoic acid, because the excess negativity would cause the conjugate base to be less stable. This is indeed the case with the *para*-hydroxybenzoic acid, which has a pKa of 4.58, compared to 4.19 in benzoic acid. However, the hydroxyl group is *ortho* to the carboxylate in salicylic acid, where it can stabilize the conjugate base via an intramolecular hydrogen bond. The stability gained from the neighboring hydrogen far outweighs the resonance effect, resulting in a greater acidity of salicylic acid (pKa=2.8) with respect to benzoic acid.

The example of salicylic acid illustrates an important point: the reactivity of a functional group is influenced by the rest of the molecule. It is helpful, then, to evaluate collector adsorption in the context of the underlying chemistry.

Sarma and Mahiuddin[15] compared the adsorption of salicylic acid (*ortho*-hydroxybenzoic acid) onto an a-alumina surface with its *para* isomer. Although the adsorption density of the *ortho* isomer was significantly greater at all pH values tested, DRIFT spectra of alumina treated with each ligand showed shifts in the symmetric and asymmetric (COO-) stretching frequencies corresponding to inner sphere complexation of the *para* isomer, but a mixture of inner and outer sphere adsorption of the *ortho* isomer. Thus, despite its greater affinity for the surface sites, the adsorption of *ortho*- hydroxybenzoic acid was relatively weaker. The authors rationalized this difference based on dissolution of the alumina solid. The *para* isomer promoted dissolution, releasing more Al^{3+} ions into solution, which then complexed with the ligand.

Ligand structure also has steric effects on the adsorption. The structure and flexibility of the nonpolar tail will affect the packing structure of the adsorbed layer, even causing the functional group to be oriented in a certain way with respect to the surface.

Han, Li, and Wandlowski[16] investigated the adsorption of aromatic carboxylic acids on gold electrodes. The authors compared benzoic acid with isophthalic acid (two carboxylic groups in 1 and 3 positions) and trimesic acid (3 carboxylic groups in 1, 3, and 5 positions) while varying the electrode potential using STM and ATR-SEIRAS. Each molecule physisorbed when the electrode was negative. On a positively charged electrode, each chemisorbed via one COO group. In the case of isophthalic and trimesic acids, the other COOH groups on the ring could form an ordered network of intramolecular H- bonds. With more COOH groups on the ring, interaction between the surface and adsorbate was somewhat weaker, but lateral interactions between adsorbate molecules increased, stabilizing the adsorbate layer. In the regular benzoic acid,

the adsorbates could not form an H-bond network, but pi-stacking caused ordering in the adsorbed layer.

Adsorption involves multiple types of forces. Chelation is a specific chemical interaction, resulting in the strongest forces. Additional forces present at the interface include van der Waals forces, H-bonding, and electrostatic interaction with the charged mineral surface. In the case of carbonate minerals, solution conditions directly impact surface charge. The charge of the ligand functional group is also dependent on solution conditions. These forces can significantly impact the favorability of adsorption, but they are often dependent on many factors, making them difficult to predict.[7] Determining whether a ligand forms a chelate provides direct information about its reactivity. The solution conditions can then be optimized to facilitate the known interaction.

Aromatic Analogs: Benzohydroxamic and Salicylhydroxamic Acid

Hydroxamic acids were identified as candidates for froth flotation as early as the 1960s.[17] In addition to iron and copper ores, hydroxamates have shown promise for REE minerals beneficiation.[18-25] Although these ligands are an improvement from traditional fatty acids, beneficiation with hydroxamic acids typically recovers only 60-72% REE from the primary ore, at best.[26, 27] To further improve efficiency, advanced collector ligands featuring the hydroxamate functional group can be strategically developed for bastnäsite flotation.

The interactions between the hydroxamic acid group (RC(=O)N(OH)R') and metal ions have been widely studied, showing evidence of chemisorption on REE mineral surfaces, and relatively weaker adsorption on gangue minerals such as calcite.[28-34] The predominant mechanism for chemisorption is chelation, with the metal cation forming a five-membered ring through interactions with both hydroxamic oxygen atoms.[28, 35] Electrostatic interactions involving hydroxamates and their influence on selective adsorption have also been discussed.[28]

Testing for selective collectors is still mostly a trial-and-error endeavor, based on empirical trends and trends observed in similar materials. More recently, research has favored a molecular-level approach to understand adsorption in terms of specific interactions between functional groups in the collector, mineral surface sites, and surrounding water molecules. This fundamental analysis has been used to evaluate ligand adsorption to various metal and mineral surfaces.[36-38] Insights gained from these in-depth studies can lead to the rational design of future collector ligands.

The aspiration for collector development features *molecular recognition of surfaces*, in which ligand molecules are structurally designed to align with the specific structure of the mineral surface. These efforts to employ molecular recognition for collectors on mineral surfaces have been reviewed in detail by Pradip.[39-42]

Previous investigations of hydroxamic acid adsorption onto various substrates via adsorption isotherms and bench-scale flotation have consistently shown a strong change in adsorption behavior with varying molecular structure.[4, 43-45] Based on the stability of cerium(III) complexes, shown in Table 3.1, adsorption affinity of octanohydroxamic acid (OHA), benzohydroxamic acid (BHA), and salicylhydroxamic acid (SHA) would be expected to decrease in the order: SHA>OHA>BHA. Salicylhydroxamic acid is both more acidic and more reactive toward cerium complexation than both octanohydroxamic and benzohydroxamic acid. SHA has been identified as a potential collector for rare earth minerals.[46] Microflotation and contact-angle experiments have shown an increase in hydrophobicity of bastnäsite after treatment with SHA.[34, 47] Selectivity of SHA for bastnäsite over calcite is hypothesized, due to a stronger chemisorption to rare earth cations.[34]

The results presented in this chapter are part of a combined approach to evaluate adsorption using density functional theory, along with Raman, FTIR, and SFG spectroscopies. Salicylhydroxamic acid (*N*,2-dihydroxybenzamide, SHA) is compared with benzohydroxamic acid (*N*-hydroxybenzamide, BHA), and salicylic acid (2-hydroxybenzoic acid, SA) to evaluate the role of adjacent hydroxamate and phenolic functional groups in bastanäsite flotation with SHA. The structures of these three ligands are shown in Figure 3.2. BHA consists of a benzene ring substituted with a hydroxamic acid group. SHA has an added phenol group *ortho* to the hydroxamate. SA is similar in structure to SHA, with a carboxylic acid group in place of the hydroxamate. A comparison of results using these ligands provides insight into how these functional groups affect adsorption onto bastnäsite and calcite surfaces.

Molecular Geometry: bis-phosphinic ligands

In this section, a computationally driven approach was used to design surface-active ligands with the optimal orientation of two phosphinic acid functional groups for binding to a specific bastnäsite surface. This approach considers the chemistry and structure of the mineral-water interface, tailoring the length and rigidity of the ligand backbone to place the adsorbing functional groups in the best relative positions for binding.

Previous work[16,17,29] has described a rational basis for computational design of collectors. Density functional theory (DFT) calculations were employed to identify the surface energies of La-bastnäsite,[17] Ce-bastnäsite, and calcite.[16] In this work, DFT calculations were conducted for a phosphinic acid ligand to characterize its adsorption configuration on bastnäsite. A search was then executed for possible ligand geometries with the molecular design software HostDesigner.[30] A small number candidates were selected based on the outcome of DFT calculations and feasibility of synthesis.

Three bis-phosphinic acids and one monophosphinic acid taken as a control were synthesized, and their binding properties were characterized using vibrational sum frequency generation (vSFG), attenuated total reflectance Fourier transform infrared (ATR-FTIR) spectroscopy, and isothermal titration calorimetry (ITC). The results of these experiments were compared with computational predictions, showing the efficacy of this computational approach in ligand design.

Materials and Methods

FTIR analysis of SHA, BHA, and SA adsorption

To determine the shift in peak positions with changing protonation state, ATR-FTIR spectra of each ligand in aqueous solution were measured at varying pH, with the bulk water background subtracted. Solutions were measured at near-saturated concentrations to enable detection of the ligand (15 mM for SA, 20 mM for BHA and SHA). To help interpret the adsorption mechanism from the FTIR of adsorbed ligands, spectra of cerium complexes were measured directly and compared with the uncomplexed ligand. The aqueous complex was formed by adding aqueous $CeCl_3$ to concentrated ligand solutions. Spectra of the complex in solution and the solid phase, which precipitates with the addition of NaOH, were measured and compared with the pure ligand solution.

ATR-FTIR spectra of each ligand in the adsorbed state were measured *in situ* using a 45° single-reflection diamond/ZnSe internal reflection element (PIKE Technologies GladiATR). A thin film of synthetic Ce-bastnäsite (particle size < 0.5 μm) was deposited directly on the IRE by adding three 10 μL drops of the solid in methanol suspension (10 g/mL) and allowing the methanol to evaporate. The dry film was rinsed with DI water, and then equilibrated with pH 8.5 NaOH solution for 20 minutes, until no further changes were observed in the spectrum. The film in solution was then set as the background before changing the liquid phase to the ligand solution. Spectra were measured at 10-minute intervals as

the ligand adsorbed, for a total of 60 minutes. The solutions used for adsorption experiments (0.5-2 mM) were below the detection limit of the aqueous ligands; peaks corresponding to the ligand appeared as a result of adsorption onto the bastnäsite film.

Spectra of adsorbed phosphinate ligands

To measure the vibrational spectra of ligands in the adsorbed state *in situ*, a thin film of synthetic Ce-bastnäsite ($CeFCO_3$) was deposited on a 45° single-reflection diamond/ZnSe internal reflection element (PIKE Technologies GladiATR). Scanning electron microscope (SEM) images of the synthetic bastnäsite showed a particle size of less than 0.5 μm. The particle film was deposited by adding 10 μl of bastnäsite in water suspension (13.5g/mL) and drying in air. A flow-through liquid cell was then placed over the film. Deionized (DI) water was flowed over the film for 20 minutes, at which point the spectrum remained constant. The background of the bastnäsite film in water was then set before changing to the ligand solution (0.4 mM, adjusted to pH 10 with NaOH). Spectra were measured in the ligand solution at 10-minute intervals for a total of 60 minutes. For comparison with the spectra of the adsorbed ligands, spectra of concentrated ligand solutions (4 mM, pH 10) were measured in the absence of the particle film, against a background of DI water. At the low concentration used for adsorption measurements, bands corresponding to the ligand in solution were not detected. Thus, peaks that appeared in the adsorption trials could be attributed to ligand molecules adsorbed onto the particle film. ATR-FTIR analysis was carried out for ligands **10b**, **13b**, and **24**. Because **24** has only one phosphinate functional group, it was also measured at 1 mM concentration.

Results and Discussion

Structural effects: Aromatic hydroxamate ligands

Aqueous salicylic acid has pKa values of 2.8 (carboxylate) and 13.4 (phenol). The monoanion is therefore the dominant form of salicylic acid over a wide range of pH values. In the deprotonated state, the symmetry of the carboxylate group is increased due to resonance. This functional group is characterized by asymmetric and symmetric stretching vibrations, which shift in frequency according to the binding mode.[48] In short, monodentate adsorption to a cation site causes one of the C-O bonds to become weaker, increasing the double bond character of the remaining C-O bond. This is reflected in the spectrum as two separate peaks, with a greater separation in wavenumber than the free ligand symmetric and asymmetric stretching. Conversely, bidentate chelation reduces the separation between symmetric and asymmetric stretching frequencies, causing the peaks to move closer together. A bridged bidentate structure causes a relatively smaller change in band positions.

Figure 3.3 shows the aqueous spectrum of SA before and after complexation with Ce^{3+}. Vibrational modes of the carboxylate group also involve movement of the aromatic ring, and bands between 1500 and 1700 cm^{-1} are combination bands. In the uncomplexed monoanion, COO^- asymmetric stretching and aromatic ring stretching (ring modes 8a and 8b) contribute to the peaks at 1575, 1593, and 1623 cm^{-1}.[49, 50] The peak at 1593 cm^{-1} is attributed mostly to aromatic C-C stretches (Wilson notation 8a/8b), with additional contribution from the carboxylate group. Two sharp peaks at 1459 and 1489 cm^{-1} are characteristic of ring modes 19a and 19b, respectively.[51]

The COO^- symmetric stretching vibration appears at 1340 cm^{-1}. An additional sharp peak at 1388 is assigned in the literature as a ring stretching vibration with contribution from the carboxylate symmetric stretch. The phenolic group vibrations are also influenced by H-bond formation with the carboxylate. In

solution, Ar-OH bending contributes to the broad intensity around 1340 cm^{-1}, while Ar-OH stretching appears as a medium peak at 1255 cm^{-1}.[49]

When Ce^{3+} is added to a salicylic acid solution, no significant change is observed at acidic pH values. When the solution pH is adjusted to pH 9, the solution turns orange, indicating formation of a complex. This complex has very low solubility, and readily precipitates as more base is added. The spectrum of the complex in solution has two sharp peaks at 1598 and 1563 cm^{-1}, in addition to a broad peak around 1520 cm^{-1}. The bands at 1561 and 1520 cm^{-1} reflect the COO^- asymmetric stretching of the chelate, which is lower in frequency than in the free ligand. Stretching vibrations of the aromatic ring are also shifted to lower frequency.

The COO^- symmetric stretching vibration shifts up into the strong band at 1388 cm^{-1}. The peak at 1459 cm^{-1}, assigned primarily to ring vibration 19a, is broadened and much higher in intensity relative to the neighboring peak at 1489. This indicates that COO^- symmetric stretching of the complex also contributes to the band at 1459. The appearance of multiple peaks related to the symmetric and asymmetric COO^- stretching vibrations indicates the presence of both chelated and bridged complexes in the aqueous phase. Complexation of the carboxylate functional group with Ce^{3+} reduces the H-bond interaction with the phenol, broadening the C-O stretching peak.

Spectra of SA adsorbed to bastnäsite *in situ* at pH 8.5 and pH 6 are shown in Figure 3.4. At pH 8.5, peaks corresponding to adsorbed SA are very weak. At 1 mM concentration, the symmetric and asymmetric COO^- stretching bands are visible at 1392 and 1563 cm^{-1}, respectively. Both of these bands are shifted closer relative to the free ligand, indicating symmetric bonding of the carboxylate group in either a bidentate chelate or bridging mechanism. The phenolic C-O stretching is a broadened peak at 1253 cm^{-1}, similar to the aqueous complex. Because this band is not significantly shifted, the phenolic oxygen atom does not appear to directly interact with the surface.

At 2 mM concentration, more SA adsorbs, slightly increasing the peak intensity. However, the peak positions are changed relative to the 1 mM spectra. The COO^- asymmetric stretching peak at 1563 cm^{-1} is smaller than the neighboring peaks at 1599 and 1623 cm^{-1}. The symmetric stretching frequency is lowered to 1388 cm^{-1}, with unresolved intensity on the low-wavenumber side of this peak. These bands are more similar to the uncomplexed ligand, indicating a weaker physisorption in addition to the chemisorbed layer. The phenolic C-O stretch is shifted further, to 1250 cm^{-1}, suggesting interaction of the phenolic group with the surface, likely through H-bonding.[52]

The low affinity of salicylic acid for bastnäsite at pH 8.5 suggests poor affinity for chelation with surface-bound cerium. This pH is near the isoelectric point of bastnäsite, so the magnitude of surface charge is low.[53] Adsorption of salicylic acid analogs onto various mineral surfaces has been reported in the literature to be strongly dependent on pH, with both total adsorption density and proportion of inner-sphere adsorbed species increasing with decreasing pH.[15, 48, 49, 52] The spectra of 2 mM SA adsorbed at pH 6 in Figure 3.4 show an increase in intensity of SA peaks. The monoanion is still the dominant form of SA in solution, but the bastnäsite solubility is increased, resulting in more aqueous cerium species. The surface also bears a higher positive charge. Thus, adsorption through both cerium chelation and electrostatic physisorption become more favorable. The symmetric COO^- stretch frequency increases with solution acidity, appearing at 1394 cm^{-1} when adsorbed at pH 6 and 1402 cm^{-1} at pH 4.7. Spectra under acidic conditions show some intensity from COO^- asymmetric stretching at 1523 cm^{-1}. The carboxylate stretching bands are shifted much closer together, indicating a bidentate chelate. Peaks at 1566 and 1623 cm^{-1} are also present in these spectra, indicating additional physisorbed ligand. None of the spectra of adsorbed SA showed evidence of monodentate-bound carboxylate, which would appear as a C=O peak at higher frequency. The phenol vibration at 1250 cm^{-1} is also more intense at lower pH. In both cases, there is more intensity to this peak

at lower wavenumber, suggesting greater involvement of the phenol oxygen in the adsorption.

Adsorption of hydroxamate ligands onto mineral surfaces have previously been measured using ATR-FTIR.[54-57] These ligands are best characterized by the strong C=O stretching frequency of the hydroxamate functional group, the precise position of which is influenced by the ligand structure. In previous investigations, the adsorption mechanisms of alkyl hydroxamates were clearly reflected in the strong C=O stretching peak.[58] The presence of an aromatic ring in BHA and SHA complicates interpretation because the aromatic (C-C) ring stretches appear as several peaks in the same region of the spectrum as the hydroxamate group vibrations. The result is a set of partially resolved bands, most of which involve a combination of hydroxamate and ring motions. These bands are described in terms of specific bonds when possible, but the trends in their behavior with binding mode are not straightforward.

Spectra of aqueous BHA and its cerium complex are shown in Figure 3.5. In pH 8.5 solution, peaks at 1609 and 1630 cm^{-1} are partially resolved. The C=O stretching band, centered at about 1630 cm^{-1} in acidic solution, decreases in frequency as the pH increases, coinciding with the ring stretching band at 1609 cm^{-1} at pH 10. A neighboring peak appears at 1575 cm^{-1}, shifting to slightly higher frequency in acidic solution, and slightly lower as the pH increases. This peak is related to the amide II mode of the hydroxamate (involving N-H bending and C-N stretching) as well as a stretching mode of the aromatic ring.[59] An additional small, broad band appears at 1530 cm^{-1} in deprotonated solution, corresponding to the lowered frequency of N-H bending, due to greater H-bond stabilization of the N-H at high pH.

When Ce^{3+} is added to the solution, the complex begins to precipitate. A strong, sharp peak at 1605 cm^{-1} is due to C=O stretching, shifted to lower frequency, along with aromatic ring vibrations. A strong peak at 1570 cm^{-1} can

also be assigned to aromatic ring stretching, as well as and C-N stretching/ N-H bending (amide II) of complexed hydroxamate.[60, 61] An additional broad peak, centered at 1535, is also related to the hydroxamate functional group. Although these bands involve combinations of hydroxamate and ring vibrations, and thus cannot be assigned in terms of individual bonds, their appearance is distinctly different from the uncomplexed spectrum.

A new peak appears at 1311 cm^{-1} upon complexation, which may also be attributed to altered bending modes of the complex. The peak at 1162 in the aqueous spectrum becomes a very strong, sharp peak at 1157, suggesting a strong correlation with C-N stretching of the hydroxamate functional group.[62-64] Finally, a strong peak at 913 in the complexed BHA corresponds to a hydroxamate group deformation, which has shifted from about 896 cm^{-1}.

Figure 3.6 shows the spectra of BHA adsorbed to bastnäsite. When BHA solution is added to the bastnäsite film, bands corresponding to adsorbed collector appear within minutes. These bands retain their shape and position while increasing in intensity for about 30 minutes or so. There is little change in the spectra after 30 minutes.

In all conditions tested, strong peaks at 1607 and 1571 cm^{-1} appear, consistent with those observed in the Ce-complexed BHA solution. A broad band around 1507 cm^{-1} varies with pH, suggesting contribution from N-H bending. The low frequency and significant intensity of this peak relative to the corresponding aqueous solutions supports the finding that the ligand is chelated. The sharp peak at 1159 cm^{-1} is reported in the literature for benzohydroxamic acid as a combined band with contributions from C-N, N-O, and aromatic C-C stretching, and C-H bending. Its position and intensity also resemble the spectra of Ce-complexed BHA.

Finally, a peak appears at 913 cm^{-1} in the adsorbed spectra, assigned to N-O stretching and CNO deformation of the hydroxamate functional group. Although this peak exhibits poor signal-to-noise due to the high background of

both the bulk water and the internal reflection element, it appears much more clearly, and at higher frequency, than in the aqueous phase. These results indicate a strong affinity for the bastnäsite surface. BHA adsorbs via a bidentate chelate.

Salicylhydroxamic acid differs from benzohydroxamic acid by the small addition of a phenol group in the *ortho* position. In its most stable conformation, the phenol group forms an intermolecular H-bond with the carbonyl oxygen in the hydroxamate group, forming a pseudo six-membered ring that is even more favorable than the pseudo five-membered ring formed by intramolecular H-bonding within the hydroxamate functional group. Computational and experimental studies have confirmed this in the gas phase and in nonpolar solvents.[65, 66] In aqueous solution, water molecules are available to interact with these sites, somewhat lowering the strength of the intramolecular H bond. However, this interaction between the phenol and hydroxamic groups is still significant, evidenced by an increased acidity of SHA relative to BHA and to *para*-hydroxybenzohydroxamic acid.

The aqueous spectrum of SHA at pH 8.5 is shown in Figure 3.7. C=O stretching contributes to the peak at 1610 cm^{-1}, which is unresolved from the aromatic C-C stretching peak at about 1600 cm^{-1}. The hydroxamate contribution to this band is evidenced by changes in the aqueous spectrum with pH. Protonation of the hydroxamate group results in distinct peaks in the pH 5.5 spectrum, at 1607 and 1633. Deprotonation of the phenol shifts this band to lower wavenumber, resulting in a single intense peak at 1600 cm^{-1} in pH 11 solution.

When SHA complexes with Ce in solution, the C=O stretching vibration contributes to a strong, sharp peak at 1600 cm^{-1}, with a broad shoulder around 1575 cm^{-1}. A broad, weak band around 1512 cm^{-1} in solution becomes a rounded, intense peak at 1507 cm^{-1} in the complex. Neighboring sharp peaks at

1471 and 1443 cm^{-1} are mostly related to vibrations of the aromatic ring, shifting with solution pH and complexation.

A strong peak at 1256 cm^{-1} in the complex is more intense and slightly higher frequency than the aqueous ligand. This band in particular has no analog in the spectrum of BHA, and its position is consistent with C-O stretching of the phenol group. The phenol bending vibration appears at 1360 cm^{-1}.[65] This band is present in the solid but diminished in the aqueous phase, reappearing after complexation with Ce^{3+}. This behavior supports the assumption that H-bond interaction between the phenolic OH and the hydroxamate carbonyl is significant in the aqueous ligand. The complex formed with Ce^{3+} involves the two hydroxamate oxygen atoms, reducing the interaction between the hydroxamate and phenol.

Spectra of SHA adsorbed to bastnäsite are shown in Figure 3.8. At 0.5 mM (pH 8.5) clear peaks corresponding to the adsorbed ligand appear within minutes. The sharp peak at 1605 cm^{-1} resembles the complexed ligand. This band involves both the hydroxamate C=O stretch and the aromatic ring C-C stretching. The sharpness of this peak—in particular, the lack of intensity at higher frequency—is consistent with chelated SHA. A partially resolved band at 1575 cm^{-1} is consistent with the spectrum of the complex. A strong peak at 1487, with additional intensity around 1507 cm^{-1}, is also indicative of chemisorbed SHA.

At 2mM concentration (pH 9), the spectrum of adsorbed SHA is slightly different. The hydroxamate mode around 1580 is less resolved from the carbonyl stretching, appearing as a shoulder at about 1582 cm^{-1}. The band around 1485 cm^{-1} is also broadened out, with less significant contribution from the shoulder. This suggests a mixed adsorption mode, with some of the SHA physisorbed at the surface. It is likely that monolayer adsorption is exceeded at 2 mM concentration.

Number and placement of functional groups: phosphinate ligands

The vibrational frequencies of organic functional groups are sensitive to changes in coordination. Thus, FTIR spectra of ligands in the adsorbed state might reveal information about the mechanisms of adsorption. The effect of binding mode on carboxylate stretching frequencies is well known in the literature.[63,64] Phosphinic acid ligands have not been as widely studied, but previous studies have shown shifts to the symmetric and asymmetric O-P-O stretch bands of phosphinic acid ligands from aqueous positions when adsorbed to goethite[65,66] and when coordinated with metal ions in solution.[67,68]

Figure 3.9 compares the spectra of **13b** adsorbed to bastnäsite *in situ* with the aqueous spectrum. The corresponding spectra for **10b** and **24** are shown in Figure 3.10 and Figure 3.11. In the aqueous phase, the free ligand symmetric stretch appears at 1023 cm^{-1} and the asymmetric stretch is about 1145 cm^{-1}.[65,66] An additional band at 1113 cm^{-1} appears due to bending vibrations of the aromatic ring. When adsorbed to bastnäsite, the symmetric stretch band is shifted to higher frequency. The resulting band has a maximum at 1034 cm^{-1} with shoulders at 1023 and 1043 cm^{-1}. The asymmetric stretch is red-shifted to 1140 cm^{-1}, with additional unresolved intensity between this band and the band at 1113 cm^{-1}.

The shifted components of the O-P-O bands are consistent with chemisorption of **13b**, presumably via monodentate complexation with each phosphinic acid group,[65] as suggested by DFT and AIMD simulations. The spectra also appear to have some contribution from unbound phosphinate, evidenced by the shoulder to the symmetric stretch at 1023 cm^{-1}. This may be due to steric hindrance, preventing both functional groups from chelating on the same surface. No definitive conclusion can be made regarding the mechanism of adsorption of **10b**, where only the symmetric O-P-O band shifts in the FTIR spectrum, whereas the asymmetric band does not shift, but increases in intensity (Figure 3.10).

The monophosphinic ligand **24** showed only very weak bands when adsorbed to bastnäsite (Figure 3.11). Even when the concentration was increased to 1 mM, the phosphinate bands were hardly detectable, and did not appear to shift from their initial positions in the aqueous state. This result is consistent with the vSFG analysis, which revealed weaker binding of the monofunctional compared to the bis-phosphinic ligand. Thus, despite the possibility that not all phosphinic groups adsorb simultaneously, the bis-phosphinic ligands **10b** and **13b** nonetheless adsorb more favorably to the bastnäsite surface than the monophosphinic ligand **24**.

Spectra of **10b** show two components of the symmetric O-P-O stretch band, likely due to a slight difference between the two phosphinic functional groups. In the aqueous phase, these are centered at 1018 and 1028 cm^{-1}. When adsorbed to the bastnäsite film, these peaks shift slightly to 1020 and 1031 cm^{-1}. An additional component to this band appears as a shoulder at 1038 cm^{-1}. The asymmetric stretch band at 1142 cm^{-1} does not appear to shift, but increases in intensity relative to the neighboring aromatic ring band in the adsorbed state. The adsorption affinity of **10b** at the bastnäsite interface is apparent by the intensity of ligand bands in the *in-situ* spectra. Symmetric and asymmetric O-P-O stretching bands of **24** (1025 cm^{-1} and 1143 cm^{-1}, respectively) are very weak in the adsorbed spectra, and do not shift from aqueous positions. This indicates a weaker adsorption of **24**, compared to **10b** and **13b**.

Summary and Conclusion

In-situ ATR-FTIR spectroscopy was used to mechanistically investigate the adsorption of similar ligands to the bastnäsite surface. This work contributed to a multifaceted approach that also included microflotation experiments, DFT calculations, and vSFG, and Raman spectroscopies. Complementary theoretical and surface-sensitive spectroscopic methods provide a molecular-level understanding of the relationship between structure and reactivity.

In the first section, salicylhydroxamic acid (SHA) was compared with benzohydroxamic acid (BHA) and salicylic acid (SA), revealing the role of adjacent hydroxamic acid and phenolic acid functional groups in improving flotation outcomes.

The ATR-FTIR analysis presented in this dissertation supported both computational analysis and microflotation outcomes, showing a stronger adsorption of the hydroxamic acid functional group on bastnäsite surfaces relative to the carboxylic acid group in SA. DFT computed binding modes and ATR-FTIR spectra show that hydroxamate and carboxylate groups present similar binding modes, each adsorbing via two oxygen atoms in the functional group. This finding was complemented by DFT, vSFG, and Raman analysis, which revealed that the aromatic ring in SHA tends to lie parallel to the bastnäsite surface at both low and high coverages, while the aromatic ring in BHA moves toward a more surface-perpendicular orientation as the ligand concentration increases.

The differing behavior of BHA and SHA on the bastnäsite surface highlights the role of the neighboring phenol functional group as an anchor in adsorption. Although the addition of the phenol group does not appear to affect the adsorption strength of SHA relative to BHA, as revealed through DFT and vSFG results, this affects how the ligand molecules arrange on the surface as they adsorb. These factors, impacting packing structure of adsorbed layers, can be utilized to design ligands which efficiently form a monolayer, inducing the surface hydrophobicity necessary to float the desired particles. By combining computationally and experimentally determined adsorption mechanisms with the results of microflotation tests, the practical outcomes of these molecular-level interactions are revealed.

The molecular-level information obtained from these experiments show the significance of nonbonding interactions in the froth flotation system. While mechanistic investigations have focused on adsorption through the lens of

hydroxamate chelation with metal ions, the approach presented here reveals the influence of hydrogen-bonding interactions in bastnäsite flotation. The fundamental understanding of how the structure of SHA influences adsorption to bastnäsite—and, consequently, its efficiency as a flotation collector—provides insight into factors of ligand design which influence performance.

The second investigation presented in this chapter applied the *in-situ* ATR-FTIR methodology to test computationally designed phosphinic acid ligands. Molecular mechanics calculations were used to identify bis-phosphinate ligands with molecular structures that would promote adsorption bastnäsite. The adsorption of three ligands to the bastnäsite surface was characterized using ATR-FTIR spectroscopy. The O-P-O vibrational frequencies were shifted from their solution-state positions upon adsorption, indicating complexation of the phosphinic acid groups at the surface. Significantly, the computationally designed bis-phosphinate ligands outperformed a monophosphinate analog. The poor signal from phosphinic acid functional group vibrations in the *in-situ* adsorbed spectra of the monophosphinic ligand were consistent with SFG measurements, which showed a lower adsorption density of the monophosphinic ligand.

These results suggest that the two phosphinate groups in the bis-phosphinic collectors enhance adsorption of the collector at low concentration. DFT calculations also suggested that the candidate ligands would have a greater affinity for adsorption to bastnäsite than calcite. This was supported by isothermal titration calorimetry measurements of the adsorption enthalpy, which revealed a much stronger interaction of the phosphinic ligands with bastnäsite than calcite. Therefore, computationally designed ligands offer a potential of improving the recovery and grade of rare earth ores from the surrounding gangue. Further FTIR measurements of adsorption to natural bastnäsite and calcite showed that ligand 10b, which features the two phosphinic groups in *para* positions, showed the greatest selective difference between the two mineral surfaces.

By combining experimental and computational methods, these experiments highlight efficacy of molecular design in improving collector selectivity for bastnäsite flotation. While computational methods can narrow the field of potential candidates by predicting which structures will perform best, spectroscopic experiments not only validate computational findings but also reveal behaviors that differ from simulated adsorption interactions. This, in turn, helps to develop more robust computational approaches. Fundamental experiments, which characterize adsorption in terms of molecular-level interactions, help to bridge the gap between pure theoretical work and empirical observations of flotation outcomes. As more relationships between ligand structure and reactivity are revealed, the search for more efficient flotation collectors can evolve from trial-and-error to informed investigation.

References

1. Langmuir, I., The mechanism of the surface phenomena of flotation. *Transactions of the Faraday Society* **1920,** *15* (June), 62-74.
2. Taggart, A. F., Flotation reagents. *TRANSACTIONS OF THE AMERICAN INSTITUTE OF MINING AND METALLURGICAL ENGINEERS* **1928,** *79*, 40-49.
3. Gaudin, A. M., *Flotation fundamentals*. University of Utah: 1928.
4. Marabini, A. M.; Ciriachi, M.; Plescia, P.; Barbaro, M., Chelating reagents for flotation. *Minerals Engineering* **2007,** *20* (10), 1014-1025.
5. Pradip; Fuerstenau, D., The adsorption of hydroxamate on semi-soluble minerals. Part I: Adsorption on barite, Calcite and Bastnaesite. *Colloids and Surfaces* **1983,** *8* (2), 103-119.
6. Fuerstenau, D. W.; Pradip, A Century of Research Leading to Understanding the Scientific Basis of Selective Mineral Flotation and Design of Flotation Collectors. *Mining, Metallurgy & Exploration* **2019,** *36* (1), 3-20.
7. Fuerstenau, M. C.; Jameson, G. J.; Yoon, R.-H., *Froth flotation: a century of innovation*. SME: 2007.
8. Nagaraj, D.; Ravishankar, S., Flotation reagents—A critical overview from an industry perspective. *Froth flotation: A century of innovation* **2007**, 375-423.
9. Zhao, H.; Yang, Y.; Shu, X.; Wang, Y.; Ran, Q., Adsorption of organic molecules on mineral surfaces studied by first-principle calculations: A review. *Advances in Colloid and Interface Science* **2018,** *256*, 230-241.
10. Rai, B., *Molecular modeling for the design of novel performance chemicals and materials*. CRC Press: 2012.
11. Rai, B., Molecular modeling and rational design of flotation reagents. *International Journal of Mineral Processing* **2003,** *72* (1-4), 95-110.
12. Pradip; Rai, B., Design of tailor-made surfactants for industrial applications using a molecular modelling approach. *Colloids and Surfaces A: Physicochemical and Engineering Aspects* **2002,** *205* (1), 139-148.
13. Herrera-Urbina, R., Recent developments and advances in formulations and applications of chemical reagents used in froth flotation. *Mineral Processing and Extractive Metallurgy Review* **2003,** *24* (2), 139-182.
14. Fuerstenau, D. W.; Herrera-Urbina, R.; McGlashan, D. W., Studies on the applicability of chelating agents as universal collectors for copper minerals. *International Journal of Mineral Processing* **2000,** *58* (1), 15-33.
15. Sarma, J.; Mahiuddin, S., Comparative adsorption involving ortho-and para-hydroxybenzoic acids in mixed-adsorbate mode onto α-alumina surface: Effect of molecular structure. *Journal of Environmental Chemical Engineering* **2014,** *2* (1), 90-99.
16. Han, B.; Li, Z.; Wandlowski, T., Adsorption and self-assembly of aromatic carboxylic acids on Au/electrolyte interfaces. *Analytical and bioanalytical chemistry* **2007,** *388* (1), 121-129.

17. Fuerstenau, M. C., Peterson, Hal D. Flotation Method for the Recovery of Minerals. 1969.
18. Pradip; Fuerstenau, D. W., Design and development of novel flotation reagents for the beneficiation of Mountain Pass rare-earth ore. *Mining, Metallurgy & Exploration* **2013,** *30* (1), 1-9.
19. Liu, W.; Wang, X.; Miller, J. D., Collector Chemistry for Bastnaesite Flotation – Recent Developments. *Miner. Process. Extr. Metall. Rev.* **2019,** *40* (6), 370-379.
20. Wanhala, A. K.; Doughty, B.; Bryantsev, V. S.; Wu, L.; Mahurin, S. M.; Jansone-Popova, S.; Cheshire, M. C.; Navrotsky, A.; Stack, A. G., Adsorption mechanism of alkyl hydroxamic acid onto bastnäsite: Fundamental steps toward rational collector design for rare earth elements. *J. Colloid Interface Sci.* **2019,** *553*, 210-219.
21. Zhang, X.; Du, H.; Wang, X.; Miller, J. D., Surface chemistry aspects of bastnaesite flotation with octyl hydroxamate. *Int. J. Miner. Process.* **2014,** *133*, 29-38.
22. Nagaraj, D. R. Process for improved precious metals recovery from ores with the use of alkylhydroxamate collectors. 1992.
23. Yoon, R.-h.; Hilderbrand, T. M. Purification of kaolin clay by froth flotation using hydroxamate collectors. 1986.
24. Assis, S. M.; Montenegro, L. C. M.; Peres, A. E. C., Utilisation of hydroxamates in minerals froth flotation. *Miner. Eng.* **1996,** *9* (1), 103-114.
25. Cui, H.; Anderson, C. G., Fundamental Studies on the Surface Chemistry of Ancylite, Calcite, and Strontianite. *Journal of Sustainable Metallurgy* **2017,** *3* (1), 48-61.
26. Nagaraj, D. R.; Farinato, R. S., Evolution of flotation chemistry and chemicals: A century of innovations and the lingering challenges. *Miner. Eng.* **2016,** *96-97*, 2-14.
27. Talens Peiró, L.; Villalba Méndez, G., Material and Energy Requirement for Rare Earth Production. *JOM* **2013,** *65* (10), 1327-1340.
28. Nagaraj, D., The chemistry and application of chelating or complexing agents in minerals separations. In *Reagents in mineral technology*, Routledge: 2018; pp 257-334.
29. Marion, C.; Li, R.; Waters, K. E., A review of reagents applied to rare-earth mineral flotation. *Adv. Colloid Interface Sci.* **2020,** *279*, 102142.
30. Anderson, C. D. Improved understanding of rare earth surface chemistry and its application to froth flotation. Colorado School of Mines. Arthur Lakes Library, 2015.
31. Pradip; Fuerstenau, D. W., The adsorption of hydroxamate on semi-soluble minerals. Part I: Adsorption on barite, Calcite and Bastnaesite. *Colloids and Surfaces* **1983,** *8* (2), 103-119.

32. Pradip; Fuerstenau, D. W., Adsorption of hydroxamate collectors on semisoluble minerals Part II: Effect of temperature on adsorption. *Colloids and Surfaces* **1985,** *15*, 137-146.
33. Cao, Z.; Cao, Y.; Qu, Q.; Zhang, J.; Mu, Y., Separation of bastnäsite from fluorite using ethylenediamine tetraacetic acid as depressant. *Miner. Eng.* **2019,** *134*, 134-141.
34. Xiong, W.; Deng, J.; Zhao, K.; Wang, W.; Wang, Y.; Wei, D., Bastnaesite, Barite, and Calcite Flotation Behaviors with Salicylhydroxamic Acid as the Collector. *Minerals* **2020,** *10* (3), 282.
35. Ren, J.; Lu, S.; Song, S.; Niu, J., A new collector for rare earth mineral flotation. *Miner. Eng.* **1997,** *10* (12), 1395-1404.
36. Waterson, C. N.; Tasker, P. A.; Farinato, R.; Nagaraj, D. R.; Shackleton, N.; Morrison, C. A., A Computational and Experimental Study on the Binding of Dithio Ligands to Sperrylite, Pentlandite, and Platinum. *The Journal of Physical Chemistry C* **2016,** *120* (39), 22476-22488.
37. Rio-Echevarria, I. M.; White, F. J.; Brechin, E. K.; Tasker, P. A.; Harris, S. G., Surface binding vs. sequestration; the uptake of benzohydroxamic acid at iron(iii) oxide surfaces. *Chem. Commun.* **2008,** (38), 4570-4572.
38. Frey, M.; Harris, S. G.; Holmes, J. M.; Nation, D. A.; Parsons, S.; Tasker, P. A.; Winpenny, R. E. P., Elucidating the Mode of Action of a Corrosion Inhibitor for Iron. *Chemistry – A European Journal* **2000,** *6* (8), 1407-1415.
39. Elam, W. A., Molecular Modeling for the Design of Novel Performance Chemicals and Materials. *The Yale Journal of Biology and Medicine* **2014,** *87* (4), 604-605.
40. Pradip, Design of crystal structure-specific surfactants based on molecular recognition at mineral surfaces. *Current Science* **1992**, 180-186.
41. Pradip; Rai, B.; Rao, T. K.; Krishnamurthy, S.; Vetrivel, R.; Mielczarski, J.; Cases, J. M., Molecular Modeling of Interactions of Diphosphonic Acid Based Surfactants with Calcium Minerals. *Langmuir* **2002,** *18* (3), 932-940.
42. Pradip; Rai, B., Molecular modeling and rational design of flotation reagents. *Int. J. Miner. Process.* **2003,** *72* (1), 95-110.
43. Zhao, G.; Zhong, H.; Qiu, X.; Wang, S.; Gao, Y.; Dai, Z.; Huang, J.; Liu, G., The DFT study of cyclohexyl hydroxamic acid as a collector in scheelite flotation. *Minerals Engineering* **2013,** *49*, 54-60.
44. Everly, D. Surface chemistry of novel collectors and their application to froth flotation of rare earth minerals. Colorado School of Mines, 2018.
45. Marion, C.; Jordens, A.; Li, R.; Rudolph, M.; Waters, K. E., An evaluation of hydroxamate collectors for malachite flotation. *Separation and Purification Technology* **2017,** *183*, 258-269.
46. Xia, L.; Hart, B.; Chelgani, S.; Douglas, K. In *Hydroxamate collectors for rare earth minerals flotation*, Conference of Metallurgists Proceedings, 2014.

47. Cao, S.; Cao, Y.; Liao, Y.; Ma, Z., Depression mechanism of strontium ions in bastnaesite flotation with salicylhydroxamic acid as collector. *Minerals* **2018,** *8* (2), 66.
48. Korpany, K. V.; Majewski, D. D.; Chiu, C. T.; Cross, S. N.; Blum, A. S., Iron oxide surface chemistry: effect of chemical structure on binding in benzoic acid and catechol derivatives. *Langmuir* **2017,** *33* (12), 3000-3013.
49. Hanna, K.; Quilès, F., Surface complexation of 2, 5-dihydroxybenzoic acid (gentisic acid) at the nanosized hematite− water interface: an ATR-FTIR study and modeling approach. *Langmuir* **2011,** *27* (6), 2492-2500.
50. Humbert, B.; Alnot, M.; Quilès, F., Infrared and Raman spectroscopical studies of salicylic and salicylate derivatives in aqueous solution. *Spectrochimica Acta Part A: Molecular and Biomolecular Spectroscopy* **1998,** *54* (3), 465-476.
51. Lewandowski, W.; Baranska, H., The influence of selected metals on the aromatic system of salicylic acid. *Applied spectroscopy* **1987,** *41* (6), 976-980.
52. Thomas, J. E.; Kelley, M. J., Interaction of mineral surfaces with simple organic molecules by diffuse reflectance IR spectroscopy (DRIFT). *Journal of colloid and interface science* **2008,** *322* (2), 516-526.
53. Herrera-Urbina, R.; Pradip; Fuerstenau, D., Electrophoretic mobility and computations of solid-aqueous solution equilibria for the bastnaesite-H 2 O system. *Mining, Metallurgy & Exploration* **2013,** *30* (1), 18-23.
54. Borer, P.; Hug, S. J.; Sulzberger, B.; Kraemer, S. M.; Kretzschmar, R., ATR-FTIR spectroscopic study of the adsorption of desferrioxamine B and aerobactin to the surface of lepidocrocite (γ-FeOOH). *Geochimica et Cosmochimica Acta* **2009,** *73* (16), 4661-4672.
55. Ni, X.; Liu, Q., The adsorption and configuration of octyl hydroxamic acid on pyrochlore and calcite. *Colloids and Surfaces A: Physicochemical and Engineering Aspects* **2012,** *411*, 80-86.
56. Sreenivas, T.; Padmanabhan, N., Surface chemistry and flotation of cassiterite with alkyl hydroxamates. *Colloids and Surfaces A: Physicochemical and Engineering Aspects* **2002,** *205* (1), 47-59.
57. Wanhala, A. K.; Doughty, B.; Bryantsev, V. S.; Wu, L.; Mahurin, S. M.; Jansone-Popova, S.; Cheshire, M. C.; Navrotsky, A.; Stack, A. G., Adsorption Mechanism of Alkyl Hydroxamic Acid onto Bastnäsite: Fundamental Steps toward Rational Collector Design for Rare Earth Elements. *Journal of colloid and interface science* **2019**.
58. Cui, J.; Hope, G. A.; Buckley, A. N., Spectroscopic investigation of the interaction of hydroxamate with bastnaesite (cerium) and rare earth oxides. *Minerals Engineering* **2012,** *36*, 91-99.
59. Espiritu, E. R. L.; Naseri, S.; Waters, K. E., Surface chemistry and flotation behavior of dolomite, monazite and bastnäsite in the presence of benzohydroxamate, sodium oleate and phosphoric acid ester collectors. *Colloids and Surfaces A: Physicochemical and Engineering Aspects* **2018,** *546*, 254-265.

60. Brennan, B. J.; Chen, J.; Rudshteyn, B.; Chaudhuri, S.; Mercado, B. Q.; Batista, V. S.; Crabtree, R. H.; Brudvig, G. W., Molecular titanium–hydroxamate complexes as models for TiO 2 surface binding. *Chemical Communications* **2016,** *52* (14), 2972-2975.
61. Zhao, C.; Sun, C.; Yin, W.; Luo, B., An investigation of the mechanism of using iron chelate as a collector during scheelite flotation. *Minerals Engineering* **2019,** *131*, 146-153.
62. Wei, Z.; Hu, Y.; Han, H.; Sun, W., Configurations of lead (II)–benzohydroxamic acid complexes in colloid and interface: A new perspective. *Journal of Colloid and Interface Science* **2020,** *562*, 342-351.
63. Liu, C.; Zhang, W.; Song, S.; Li, H., Study on the activation mechanism of lead ions in wolframite flotation using benzyl hydroxamic acid as the collector. *Minerals Engineering* **2019,** *141*, 105859.
64. Al-Saadi, A. A., Conformational analysis and vibrational assignments of benzohydroxamic acid and benzohydrazide. *Journal of Molecular Structure* **2012,** *1023*, 115-122.
65. Kaczor, A.; Szczepanski, J.; Vala, M.; Proniewicz, L. M., Matrix-isolation and computational study of salicylhydroxamic acid and its photochemical degradation. *Physical Chemistry Chemical Physics* **2005,** *7* (9), 1960-1965.
66. García, B.; Secco, F.; Ibeas, S.; Muñoz, A.; Hoyuelos, F. J.; Leal, J. M.; Senent, M. L.; Venturini, M., Structural NMR and ab initio study of salicylhydroxamic and p-hydroxybenzohydroxamic acids: evidence for an extended aggregation. *The Journal of organic chemistry* **2007,** *72* (21), 7832-7840.

Appendix

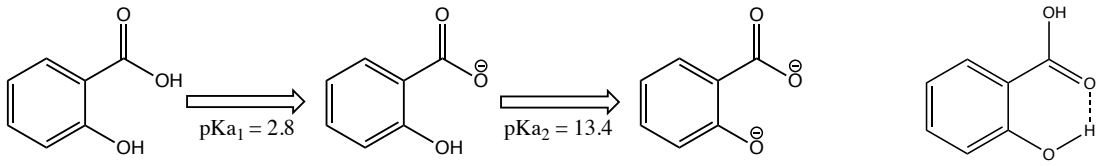

Figure 3.1: Intramolecular H-bonding in salicylic acid.

Table 3.1: Hydroxamates and their stability constants.

	Aceto			**Benzo**			**Salicyl**	
H+	9.40	-	-	8.63	-	-	7.40	9.78
Ca(II)	2.45	-	-	2.14	-	-	3.24	-
Ce(III)	7.85	6.90	5.76	7.25	6.40	5.22	11.00	8.69
La(III)	6.99	6.05	3.98	6.75	5.90	-	10.90	7.77

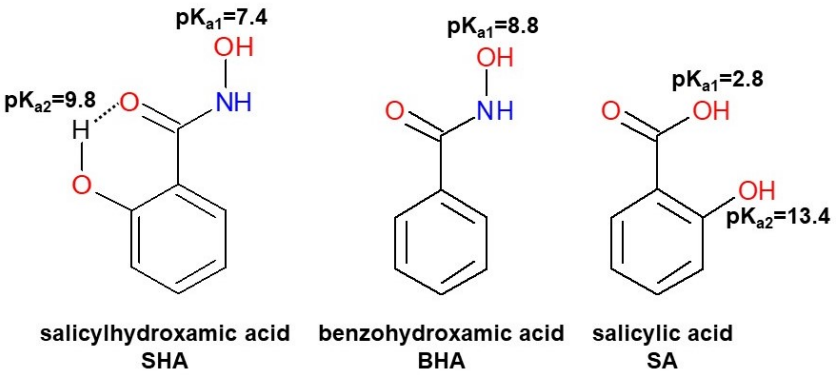

Figure 3.2: Structures of SHA, BHA, and SA

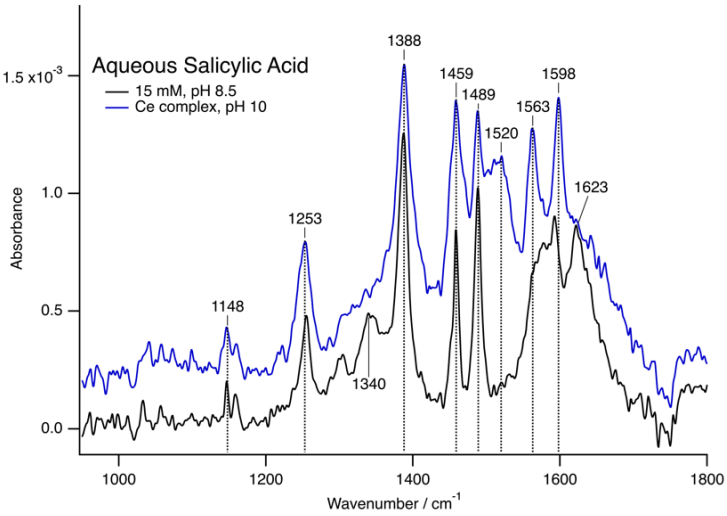

Figure 3.3: FTIR spectra of salicylic acid and Ce-salicylate in aqueous solution.

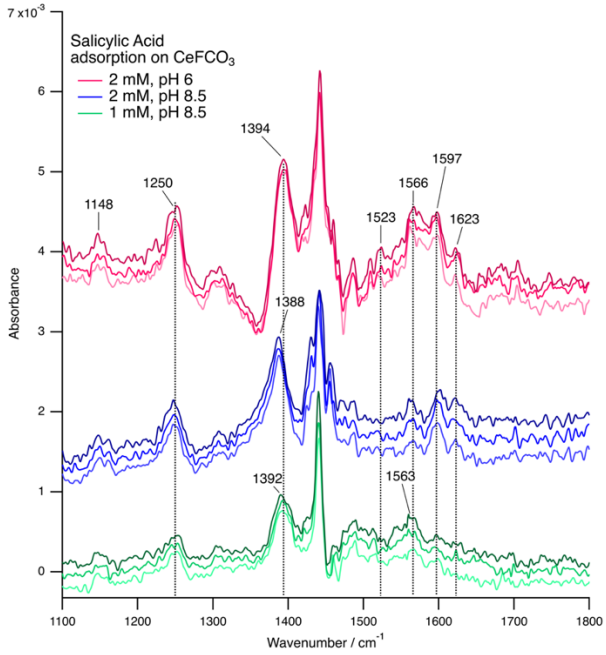

Figure 3.4: FTIR spectra of salicylic acid adsorbed to bastnäsite.

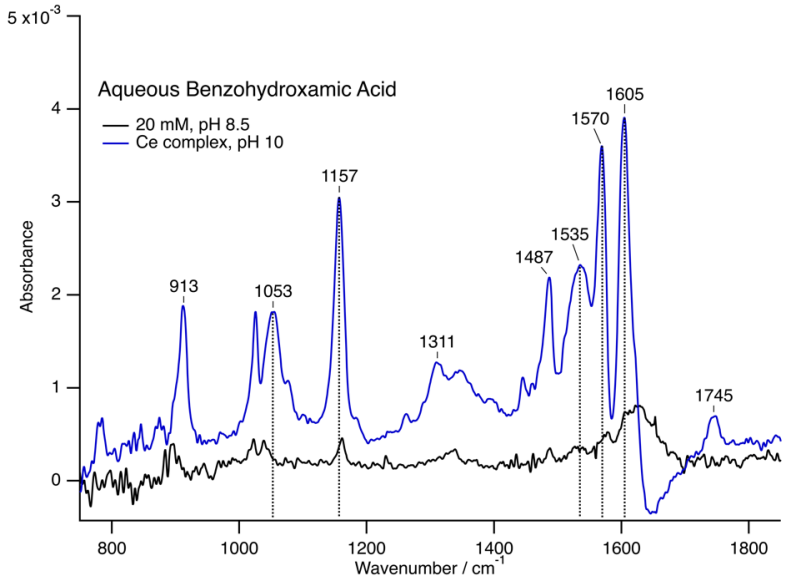

Figure 3.5: FTIR spectra of benzohydroxamic acid and Ce-benzohydroxamate in aqueous solution.

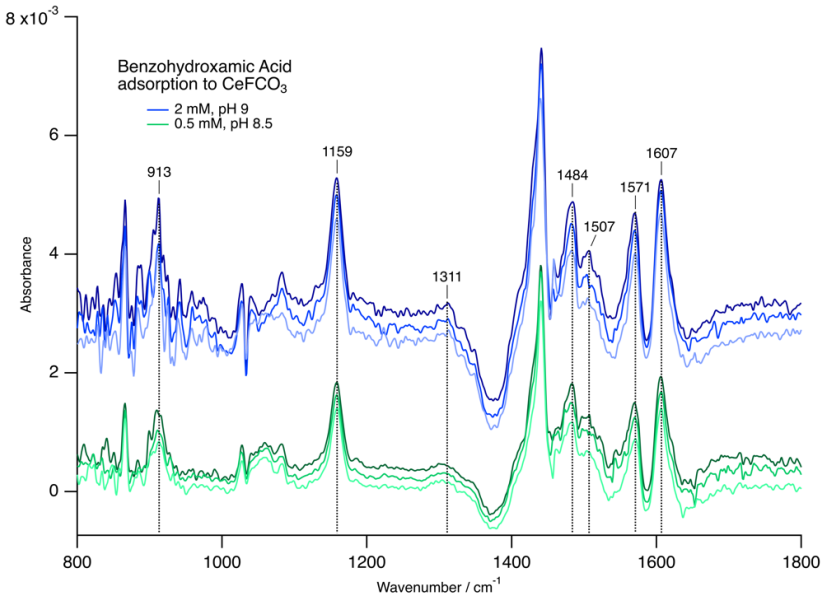

Figure 3.6: FTIR spectra of benzohydroxamic acid adsorbed to bastnäsite.

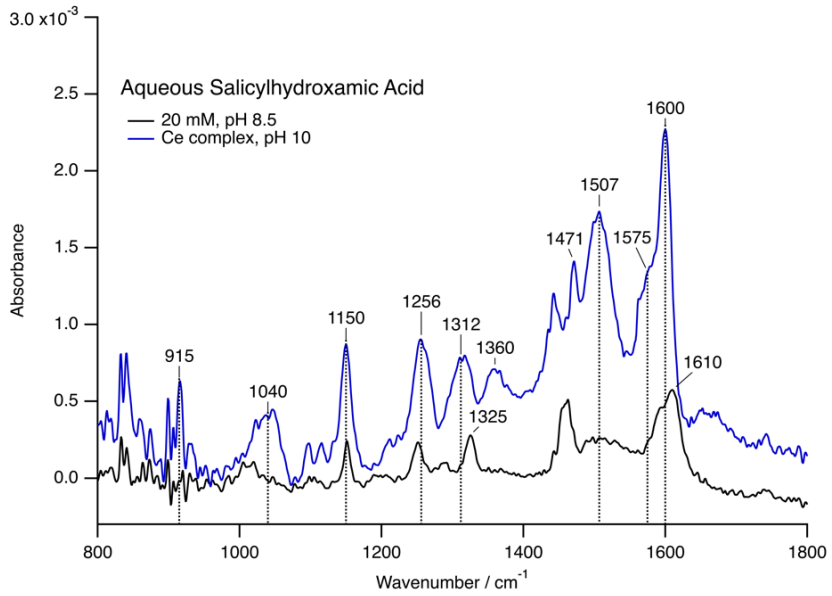

Figure 3.7: FTIR spectra of salicylhydroxamic acid and Ce-salicylhydroxamate in aqueous solution.

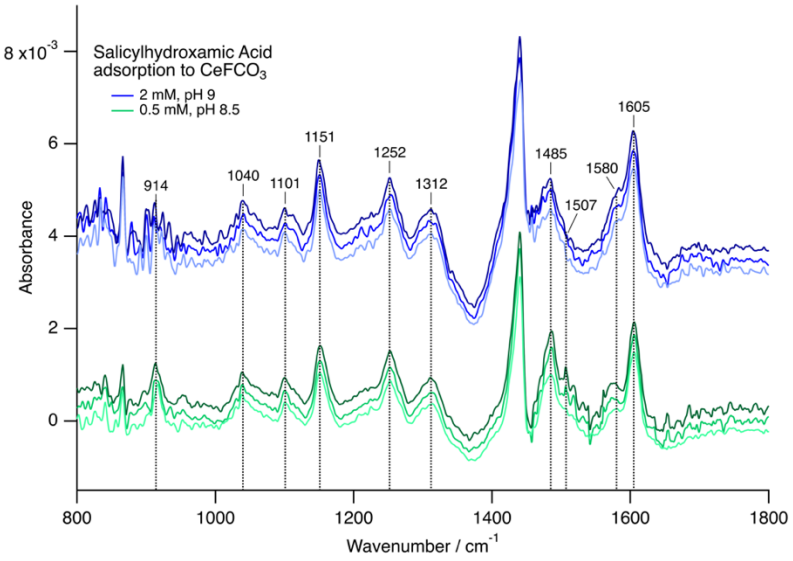

Figure 3.8: FTIR spectra of salicylhydroxamic acid adsorbed to bastnäsite.

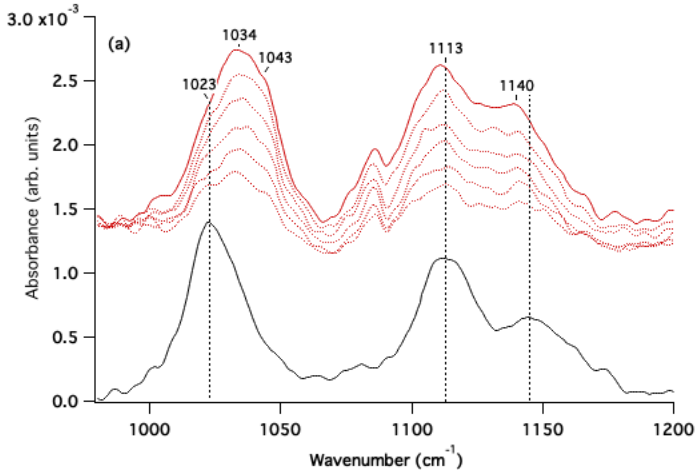

Figure 3.9: FTIR spectra of 13b (0.4 mM) adsorbed onto synthetic Ce-bastnäsite.

The spectrum of the ligand in aqueous solution (4 mM) is shown in black at the bottom of the plot. The colored traces are the spectra taken at (bottom to top) 10,

20, 30, 40, 50, and 60 minutes of the adsorbed ligand in situ, with the bastnäsite particle film and bulk water spectra subtracted (adsorbed spectra are vertically offset from aqueous spectra for clarity). The unlabeled peaks at 1090 cm^{-1} in each adsorbed spectrum are a residual peak from the bastnäsite background.

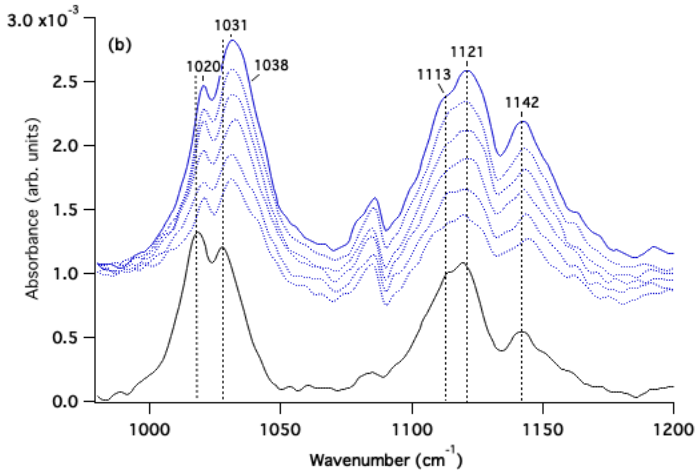

Figure 3.10: FTIR spectra of 10b (0.4 mM) adsorbed onto synthetic Ce-bastnäsite.

The spectrum of the ligand in aqueous solution (4 mM) is shown in black at the bottom of the plot. The colored traces are the spectra taken at (bottom to top) 10, 20, 30, 40, 50, and 60 minutes of the adsorbed ligand *in situ*, with the bastnäsite particle film and bulk water spectra subtracted (adsorbed spectra are vertically offset from aqueous spectra for clarity). The unlabeled peaks at 1090 cm^{-1} in each adsorbed spectrum are a residual peak from the bastnäsite background.

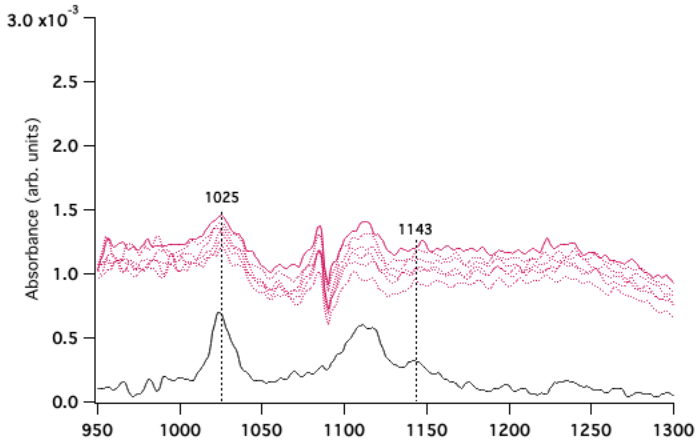

Figure 3.11: FTIR spectra of 24 (1 mM) adsorbed onto synthetic Ce-bastnäsite.

The spectrum of the ligand in aqueous solution (4 mM) is shown in black at the bottom of the plot. The colored traces are the spectra taken at (bottom to top) 10, 20, 30, 40, 50, and 60 minutes of the adsorbed ligand in situ, with the bastnäsite particle film and bulk water spectra subtracted (adsorbed spectra are vertically offset from aqueous spectra for clarity). The unlabeled peaks at 1090 cm^{-1} in each adsorbed spectrum are a residual peak from the bastnäsite background.

CHAPTER 4
STRUCTURE OF THE BASTNÄSITE (001) SURFACE

At the time of this dissertation, the results presented in this chapter are part of an ongoing project. A manuscript is currently in development:

Wanhala, A.K., Stubbs, J., Gordon, A., Custelcean, R., Lee, S.S., Stack, A.G. Structure of Bastnäsite (001) at the Mineral-Water Interface.

Anna K. Wanhala performed the CTR data fitting, including script writing to add parameters to the model code. She also conducted a set of experiments at the Advanced Photon Source to obtain one of the data sets, along with Sang Soo Lee.
The rest of the datasets, including the sample in air analyzed in this chapter, were collected at the Advanced Photon Source by Joanne Stubbs, Alexander Gordon, and Andrew Stack. Joanne Stubbs aided in the script writing for the model and provided guidance throughout the fitting process.
Radu Custelcean conducted a refinement of the bastnäsite bulk structure using single-crystal X-Ray Diffraction.

Abstract

Rare earth elements (REEs) are crucial components in energy efficient technologies, but current methods used for beneficiation of REE ores are inefficient. Bastnäsite ([Ce,La]FCO_3) is the primary mineral source of light rare earth elements, but its surface structure is not well understood. This presents a major limitation to rational design of better separation strategies through "molecular recognition."

The crystal structure of bastnäsite consists of alternating layers of carbonate (CO_3^{2-}) and cerium-fluoride (CeF^{2+}) along the (001) direction. Despite being one of the most common surfaces found in natural samples, this surface presents no obvious stoichiometric termination, because both of these layers carry an overall charge. Thus, it is not clear what surface sites are available for chelation by ligands used for separation.

Surface X-ray scattering was used to measure crystal truncation rods (CTRs) of the bastnäsite [001] surface in air and in aqueous solutions. In this chapter, results of the surface in air are presented. Model fitting of specular and off-specular data reveals the three-dimensional atomic structure of the interface. The resulting fit is a partially occupied carbonate layer at the surface, which is significantly altered from the bulk structure. This dramatic relaxation, enabled by the increased space of the partially occupied layer, explains why this surface is so stable in nature. Evidence of ordered water at the interface is also observed.

The sets of CTR data measured for this surface in solutions of varying pH may reveal conditions in which the surface would be more favorable for adsorption of flotation collectors. The resulting fit of the crystal in air describes the surface structure in a set of rationalized model parameters, which will be used in ongoing work to directly compare the additional datasets. At the time of this dissertation, the measured surface structure differs from previous density functional theory (DFT) and ab-initio molecular dynamics (AIMD) simulations. The extent of relaxation in the terminal layer is greater than computational

predictions, resulting in a surface that is more stable than anticipated. Computational simulation of this surface with expanded consideration for these dramatic changes may result in a better approximation to the experimental findings. This work highlights the limitations of certain assumptions—specifically, an abundance of cerium cation sites on the surface—when designing flotation collectors. With this improved understanding of the surface structure, appropriate strategies to target the bastnäsite surface in flotation can be developed.

Background

Existing Models of the Bastnäsite Surface

The crystal structure of bastnäsite has layers of cerium and fluorine that alternate with layers of carbonate along the z direction, as shown in Figure 4.3. A computational evaluation of several possible surfaces predicted that the (100) surface would exhibit the greatest stability.[1] This result makes sense intuitively; cutting the crystal along the z axis leaves an alternating row of cationic and anionic groups at the surface. Indeed, crystals in nature are often terminated in this way. However, as shown in Figure 4.4, many samples are dominated by the (001) surface, which is predicted to have a much lower stability. Termination at either the CO_3^{2-} layer or the CeF^{2+} layer results in a residual surface charge.

Similar dipolar surfaces in oxide minerals have been observed to relax significantly from bulk crystal structures.[2] Predicted states for the bastnäsite (001) surface feature a much greater reorientation relative to nonpolar surfaces such as (100). Figure 4.5 shows a comparison of the optimized structures for these two surfaces, revealing carbonate group in the (001) surface that are rotated from their positions in the bulk.

Water is also expected to play a role in surface stabilization. If the surface is stoichiometrically terminated, the resulting residual charge may be balanced by adsorbed water molecules. The Ce-O distance of adsorbed water in modeled

CeF terminated structures is about 2.5-2.7 Å. In the X-ray data, water will only contribute to the fit if it is in an ordered structure. Under ambient conditions, there is likely some amount of water vapor adsorbed to the surface. In solution, surfaces of ionic minerals have been observed to have a layer or two of ordered water.[3, 4]

X-Ray Reflectivity and the Crystal Truncation Rod

X-ray reflectivity is a valuable tool for characterizing mineral-water interfaces *in situ* because X- rays are not significantly absorbed by water. X-rays also have very small wavelengths—on the order of Angstroms—which corresponds to the size of individual atoms. Therefore, the interference of X-rays scattered from atoms in an ordered crystal can measure structures with atomic-scale precision.[5]

Incident X-rays are scattered by electrons, and electron density is concentrated around individual atoms. Two scattered waves are in phase when their path length difference is an integer multiple of the wavelength. Waves that are in-phase interfere constructively, and the magnitude of the amplitude of the scattered wave is the sum of the incident amplitudes. In a crystalline solid, atoms are located at periodic distances from each other. Waves reflected from planes of atoms separated by distance *d* have different path lengths. This is illustrated in Figure 4.1.

Here, the difference in path lengths between waves reflected from point A and point B is related to the atomic spacing, *d*, and the diffraction angle, θ. The wave reflected from point B is longer by exactly 2d sinθ. The waves will interfere constructively when this path length difference is an integer number of wavelengths, λ, expressed by Bragg's Law:

$$2d\ sin\theta = n\lambda$$

The Bragg condition is met at any diffraction angle where n is an integer.

X-ray diffraction (XRD) is used to determine the bulk structure of a crystal by measuring the scattering intensity as a function of incident angle. X-ray *reflectivity* is the application of XRD for studying interfaces. In a terminated crystal lattice, scattering from the bulk structure appears as high intensity Bragg peaks. Additionally, there is a very small scattering intensity from the surface. At angles where the bulk Bragg condition is not satisfied (between Bragg peaks), the scattering intensity is attributed to the crystal surface. This intensity is known as the Crystal Truncation Rod (CTR), because it is continuous between Bragg points (like a rod) and arises from a truncated crystal.[6] The CTR intensity can be observed in Figure 4.2.

In reciprocal space, scattering can be expressed in terms of the momentum transfer, *Q*, rather than the diffraction angle. *Q* is a vector with magnitude related to the diffraction angle by:

$$|Q| = \frac{4\pi}{\lambda}\sin(\theta)$$

Q is expressed in terms of the crystal lattice constants (*abc*) and Miller Indices (HKL) probed by a particular scattering angle. A Bragg peak appears at values of *Q* that correspond to an integer multiple of the Bragg plane spacing, *dHKL*:

$$Q_{HKL} = [H(2\pi/a), K(2\pi/b), L(2\pi/c)]$$

$$|Q_{HKL}| = \frac{n2\pi}{d_{HKL}}$$

A CTR is measured along L at fixed H and K. The scattered intensity, *ICTR,* is proportional to the square of the structure factor, *F*:

$$I_{CTR} \propto |F|^2 = \frac{|f_0|^2}{4sin^2(Qc/2)}$$

where *f0* is the scattering strength of the layer and *c* is the layer spacing. The structure factor is summed over each atom, *j*, in the sample:

$$F = \sum_j f_j(Q) \exp\left[i\boldsymbol{Q} \cdot \boldsymbol{R}_j\right] \exp\left[-\tfrac{1}{2}\left(Qu_j\right)^2\right]$$

The atomic scattering factor, $f_j(Q)$, varies as a function of the momentum transfer. At Q=0, f_j is equal to the atomic number, Z. $\mathbf{R}_j$ is the position vector, and u_j is the vibrational amplitude. The second part of the summation is the Debye-Waller factor, which is the distribution of an atom from its average position, in Å, due to thermal vibrations. Atoms at the surface typically have a greater vibrational amplitude than bulk atoms because they are less constrained.
For a crystal that is terminated by the (001) plane, the unit cell repeats infinitely in both directions from the origin in a and b, but only in one direction in c. Scattering is then dependent on a 2-dimensional Bragg condition—when H and K are integers—and continuous along L at these values. The shape of the CTR—that is, the variation of its intensity with Q—depends on the structure of the surface.

Introduction

Modern approaches to collector design employ powerful computational methods to predict adsorption.[7] The utility of molecular design in developing specialized froth flotation ligands increases as detailed information about mineral-water interfaces becomes available. This shift, from traditional empirical methods to a more informed approach, has the potential to reduce the time and resources involved in testing many individual ligands. However, computational methods rely on accurate starting information. In the case of froth flotation, this includes not only the structure of the mineral-water interface but also the reactivity of adsorption sites as a function of solution chemistry.

The existence—and apparent natural stability—of the (001) surface presents some questions that are critical to the surface chemistry of bastnäsite. The primary difference between bastnäsite and calcite is the presence of trivalent rare earth cations. If the (001) surface is terminated at the CeF^{2+} layer, this

surface would provide plenty of cation sites for ligand adsorption. However, termination at the CO_3^{2-} layer would hinder adsorption on this crucial surface that constitutes much of the surface area of bastnäsite.

Several mineral types have been analyzed using X-Ray reflectivity. In some cases, the surface layers relax significantly with respect to bulk positions, while other mineral surfaces show smaller relaxations.

Geissbühler and Fenter[3] analyzed the structure of the calcite(104)-water interface using X-ray reflectivity. The authors found two layers of ordered water at 2.2 and 3.2 angstrom from the surface. The authors found vertical and lateral relaxations in the first two layers of calcite, with both Ca and CO3 ions moving in toward the bulk. The carbonate groups also rotated to lie closer to the surface.

The lateral displacement at the surface was -0.26 and -0.39 Angstrom for calcium and carbonate, respectively. The authors determined that the first water layer was significantly displaced laterally from the Ca^{+2} surface sites.

Xenotime (YPO_4) is another mineral source of REEs. Stack et al.[8] investigated the structure of the xenotime(100)-water interface and found very little movement of surface atoms from bulk positions. Additionally, there were two layers of ordered water molecules, coordinated with surface sites. The authors attributed the small surface relaxation (relative to other minerals) to the large trivalent REE cations, which were oriented in stable periodic bonded chains (PBCs) with phosphate anions.

Bastnäsite and xenotime have similar REE cations. While xenotime contains a mixture of yttrium (Z=39) and heavier elements near dysprosium (Z=66), bastnäsite is composed of mostly lanthanum, cerium, and neodymium (Z=57-60). However, the bastnäsite surface may behave more similarly to other carbonate minerals, such as calcite, which show more significant relaxations. Furthermore, the (001) surface is charged—either a CeF^{2+} or CO_3^{2-} termination—and will likely undergo some rearrangement to balance the residual charge.

Methods and Materials

Bastnäsite Bulk Structure

The bulk structure of bastnäsite is shown in Figure 4.3. Bastnäsite has a hexagonal crystal structure (space group $P\bar{6}2c$) with unit cell dimensions $a = b =$ 7.1129 Å, c = 9.7577 Å, Z = 6. The structure features alternating layers of CeF^{2+} and CO_3^{2-} along the z direction.

The structure of the bastnäsite sample used for crystal truncation rod measurements was determined by single-crystal X-ray diffraction at 23 °C using a Bruker SMART APEX CCD diffractometer with fine-focus Mo K_α radiation (λ = 0.71073 Å), operated at 50 kV and 30 mA. The structure was solved by direct methods and refined on F^2 using the SHELXTL software package (Bruker AXS Inc., Madison, WI, 1997). Absorption corrections were applied using SADABS, part of the SHELXTL package. The refined structure is consistent with published bastnäsite structures.[9, 10]

The (001) surface was used for CTR measurements. The crystal was cut within 0.06° of the (001) surface, then polished using a colloidal silica suspension, and cleaned with acetone, ethanol, and DI water.

Crystal Truncation Rod Measurements

Crystal truncation rods were measured by X-Ray Reflectivity at beamline 13-BM-C at the Advanced Photon Source. Incident energy was 15 keV (λ = 0.8266 Å) for all measurements. The beam was focused horizontally with a side deflecting Rowland circle Si monochromator. Vertical focus was achieved by a dynamically bent Rh-coated Si mirror. The resulting beam dimensions were 0.4 mm (horizontal) by 0.07 mm (vertical).

Samples were mounted in a Newport Kappa six-circle diffractometer. Intensity of the reflected beam was measured with a Dectris PILATUS 100k pixel array detector (Dectris, Inc.). Specular reflectivity was measured under each

condition, along with a set of off-specular measurements at a 2° fixed incidence angle. Intensities of the reflected beam were background subtracted and integrated using the Python Data Shell software package.[11]

To measure the sample under various conditions, the sample was held in a thin film cell, covered by a 7.5 μm Kapton film. Between measurements, the cell was filled with the next solution and allowed to equilibrate for at least 30 minutes. Immediately prior to reflectivity measurements, most of the solution volume was removed, leaving a thin film of solution between the sample and Kapton film.[12] The surface was monitored for changes due to degradation from the X-ray beam by occasionally measuring several points along the *10L* rod. No significant change in intensity was observed.

The sample was first measured with no solution present. Aqueous measurements then followed in the order: pH 8.5 (NaOH), pH 4.2 (HCl), pH 1.6 (HCl), and pH 9 (Na_2CO_3). A total of 11 CTRs were measured under each condition, excluding symmetry-equivalent duplicates.

CTR Fitting

The CTR data was fit to a model of the surface structure using the GenX software package, with the figure of merit evaluated by chi-squared (χ^2):

$$\chi^2 = \frac{1}{N_p}\sum_i \left(\frac{|R_i - R_c|}{\sigma_i}\right)^2$$

N_p is the number of data points, R_i and R_c are the measured and calculated intensities for each data point *i*, and σ_i is the measured error for each point.

The surface model included two single-unit-cell slabs: a bulk slab with the refined crystal structure, and a surface slab that changed as parameters were added to the fit. Parameters were added systematically, beginning with those expected to have the greatest effect on the overall model.

Throughout the fitting, p3 plane group symmetry was maintained. This assumption is supported by the close match between measured rods that are

equivalent by this symmetry, which were averaged in the fitted dataset. F atom movement in the x/y plane was restricted by unit cell symmetry. Furthermore, the CO_3 group was kept together in its trigonal planar shape.

The unit cell is oriented with a carbonate layer at the surface; to test for each termination, a model with the terminal carbonate layer removed was also compared. Initially, neither termination resulted in a significantly better fit. However, as parameters were added, the model with a terminal carbonate layer included began to emerge as the better fit.

Results and Discussion

Figure 4.6 shows the full set of crystal truncation rods measured for the bastnäsite sample in air, after averaging symmetrically equivalent reflections. The reciprocal space representation of these surface rods is plotted in Figure 4.7. There was very good agreement between equivalent measurements; for instance, the intensities along (-1,1) were a close match to the symmetry equivalent (1,0) rod. The resulting error bars in the data are very small. There are 1253 data points in the set.

Specular reflection is plotted in the (0,0,L) rod. The specular rod is significant because it measures laterally-averaged electron density in the surface normal direction. For the (001) surface, this corresponds to atomic positions in the z direction. The specular rod is measured to L=10.27, corresponding to a resolution of <1Å. The rest of the rods are off-specular rods, which contain information about the lateral position of atoms, as well as the vertical position.

The CTR data is fitted by modeling the structure of the surface, starting with all atoms in bulk positions. With each added parameter, the chi squared figure of merit is evaluated to determine the quality of the fit. The parameters that have the greatest effect on the fit are added first, followed by finer adjustments.

Figure 4.8 shows the modeled intensity of the specular rod (0,0) and an off-specular rod (1,3) with each surface termination. Neither bulk-like termination

fits this rod particularly well. Adjusting for intensity and surface roughness improves the fit, but the data at high Q are still far from the model. Because the specular rod only measures structures normal to the interface, there is little difference between the two terminations. Off-specular rods are necessary to gather data about ordering in the lateral direction. In comparison, the shape of the (1,3) rod changes significantly with surface termination. Again, adjusting for intensity and roughness slightly improves the fit but does not significantly alter the model. The bulk-like terminations with intensity and roughness adjustments fit to chi-squared of about 58.3 for the CO_3 termination, and 53.8 for the CeF termination.

The CTR model was first evaluated to determine whether the surface was terminated by CeF^{2+} or CO_3^{2-}. Initial fits with atoms in bulk-like positions were very poor with either termination, even with parameters added for relative intensity and surface roughness. The fit was significantly improved by the addition of a symmetry-related parameter; the bastnäsite unit cell contains two of each ionic layer, related by a rotoinversion. Individual layers are separated by half of the unit cell in height (4.879 Å). Even a slight variation from an atomically flat surface would result in both layers of the unit cell being present at the surface. When the parameter was added to account for the relative distribution of each layer at the surface, it fit consistently to about 0.5, indicating both layers in equal amounts. This lowered the figure of merit to 37.6 and 35.0 for the CO_3 and CeF terminations, respectively.

The top layer of atoms was then allowed to relax, further improving the fit. Relaxation consisted of allowing partial site occupancies and movement of atoms, with the carbonate group moving together. With the addition of these adjustments, both fits began to point to a carbonate-terminated surface, with cerium and fluorine occupancies of the terminal layer fitting to nearly zero occupancy. From this point, the fit was continued assuming a carbonate terminal layer.

Certain rods were still very poorly fit. A script was then written to enable rotation of the carbonate groups in three directions. A diagram of these three rotation angles is shown in Figure 4.9. This significantly improved the fit, with the effect on the 21L rod shown in Figure 4.10. The resulting fit featured a carbonate occupancy of about 0.40, with the carbonate groups rotated about 23.5 degrees in the plane of the surface, and 17.7 degrees away from surface normal ("laying down"). The carbonate rotation improved the figure of merit to 12.9.

Two sets of ordered water molecules were then added to the fit. Hydrogen atoms do not contribute to the reflected signal, so the water molecules were represented by oxygen atoms. The starting positions of these atoms were set to where the next layer of Ce and F atoms would be. Their positions and displacement parameters were fit, resulting in an improvement in the chi-squared to 10.2. Allowing the second layer of atoms in the unit cell to relax further improved the figure of merit to 7.54.

The adsorbed water atoms have much higher displacement parameters than atoms in the solid. To further improve the fit, parameters were added to enable anisotropy of these atoms. Thermal displacement was constricted to equal in all directions within the surface plane, and separate displacement in the direction normal to the surface. This improved the figure of merit to 6.62.

The resulting structure is shown in Figure 4.11. This fit features a partially-occupied carbonate layer on the surface that is relaxed significantly from the bulk structure. Additionally, two layers of adsorbed water are present. These atoms have a greater displacement parallel to the surface plane. Overall, 55 parameters were added to the fit and the chi-squared figure of merit was 6.62.

The fit is a good visual match to the data, as shown in Figure 4.12. Because the chi-squared figure of merit weighs the difference between the data and simulation at each point by the reported error, the small error reported in the data prevents the figure of merit from getting much lower than this. Realistically,

there is some amount of systematic error present in the data. By adding a systematic error of only 2%, the chi-squared improves to 2.80.

Summary and Conclusion

CTR measurements of the bastnäsite (001) surface in air reveal a surface that is terminated by a partially occupied carbonate layer. The partial occupancy serves two purposes: first, it balances the positive charge from the underlying cerium fluoride layer, without adding additional negative charge. The second effect is that the carbonate layer then has more room to relax. The amount of relaxation of this layer relative to the bulk crystal structure is surprisingly high. This provides a much-needed explanation behind the stability of this surface.

A significant implication of this finding is that the bastnäsite (001) surface does not appear to have cerium cation sites available for anion adsorption. This does not bode well for flotation, where collectors are primarily developed to target specific cation sites. Additional strategies may need to be developed to either manage this surface while targeting other sides of the particles, or to alter the termination structure of this surface. However, the prevalence of this surface in nature does not necessarily correlate to its prevalence in flotation. The equilibrium configuration of surface carbonates is significantly relaxed from the bulk structure. Thus, in the process of grinding the ore for flotation, this surface would not appear as a cleaved surface. The findings of this work suggest that the (001) surface is not a dominant breakage plane in bastnäsite.

The CTR data taken under aqueous solution conditions show a significant change in both shape and intensity of some rods. It is possible that the occupancy of the terminal carbonate layer is changed by the solution conditions. This further investigation will also provide insight into how the cutting and polishing process, necessary for measuring crystal truncation rods, may have influenced the surface structure. After prolonged exposure to solution, it is possible the surface rearranges again. This work will be continued to apply the

existing model to the remaining datasets to determine the cause of the observed intensity changes.

If the carbonate layer is depleted under acidic conditions, acid treatment of the ore may be utilized to change the surface termination. This type of pretreatment could produce surfaces with more metal cation sites to facilitate collector chelation. Fundamental understanding of what surfaces are produced by breaking mineral phases in the mining process, and how these surfaces respond to changes in solution chemistry, is vital to developing computational approaches that design ligand molecules to specifically target mineral surfaces.

References

1. Srinivasan, S. G.; Shivaramaiah, R.; Kent, P. R.; Stack, A. G.; Riman, R.; Anderko, A.; Navrotsky, A.; Bryantsev, V. S., A comparative study of surface energies and water adsorption on Ce-bastnäsite, La-bastnäsite, and calcite via density functional theory and water adsorption calorimetry. *Physical Chemistry Chemical Physics* **2017,** *19* (11), 7820-7832.
2. Noguera, C., Polar oxide surfaces. *Journal of Physics: Condensed Matter* **2000,** *12* (31), R367.
3. Geissbühler, P.; Fenter, P.; DiMasi, E.; Srajer, G.; Sorensen, L.; Sturchio, N., Three-dimensional structure of the calcite–water interface by surface X-ray scattering. *Surface Science* **2004,** *573* (2), 191-203.
4. Bracco, J. N.; Lee, S. S.; Stubbs, J. E.; Eng, P. J.; Heberling, F.; Fenter, P.; Stack, A. G., Hydration structure of the barite (001)–water interface: Comparison of x-ray reflectivity with molecular dynamics simulations. *The Journal of Physical Chemistry C* **2017,** *121* (22), 12236-12248.
5. Fenter, P. A., X-ray reflectivity as a probe of mineral-fluid interfaces: A user guide. *Reviews in mineralogy and geochemistry* **2002,** *49* (1), 149-221.
6. Robinson, I. K., Crystal truncation rods and surface roughness. *Physical Review B* **1986,** *33* (6), 3830.
7. Zhao, G.; Zhong, H.; Qiu, X.; Wang, S.; Gao, Y.; Dai, Z.; Huang, J.; Liu, G., The DFT study of cyclohexyl hydroxamic acid as a collector in scheelite flotation. *Minerals Engineering* **2013,** *49*, 54-60.
8. Stack, A. G.; Stubbs, J. E.; Srinivasan, S. G.; Roy, S.; Bryantsev, V. S.; Eng, P. J.; Custelcean, R.; Gordon, A. D.; Hexel, C. R., Mineral–Water Interface Structure of Xenotime (YPO4){100}. *The Journal of Physical Chemistry C* **2018,** *122* (35), 20232-20243.
9. Mariano, A. N., The Atomic Arrangement of Bastnasite-(Ce), Ce (CO3) F, and Structural Elements of Synchysite-(Ce), Röntgenite-(Ce), and Parisite-(Ce). *American Mineralogist* **1993,** *78*, 415-418.
10. Gysi, A. P.; Williams-Jones, A. E., The thermodynamic properties of bastnäsite-(Ce) and parisite-(Ce). *Chemical Geology* **2015,** *392*, 87-101.
11. Github Repository for the xray Data analysis Library (Tdl). https://github.com/xraypy/tdl.
12. Lee, S. S.; Fenter, P.; Park, C., Optimizing a flow-through X-ray transmission cell for studies of temporal and spatial variations of ion distributions at mineral–water interfaces. *Journal of synchrotron radiation* **2013,** *20* (1), 125-136.

Appendix

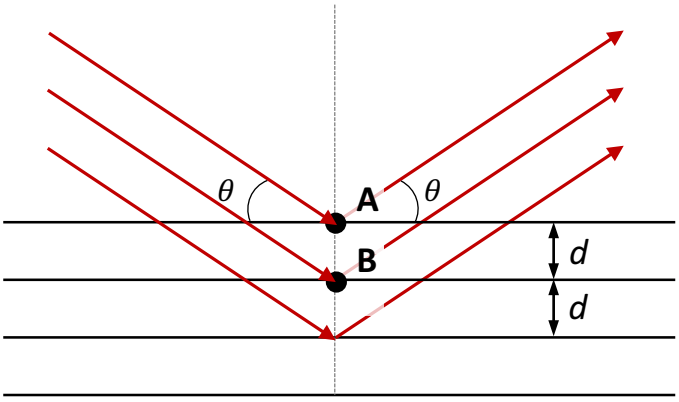

Figure 4.1: Diagram of X-ray scattering from atomic planes in a crystal.

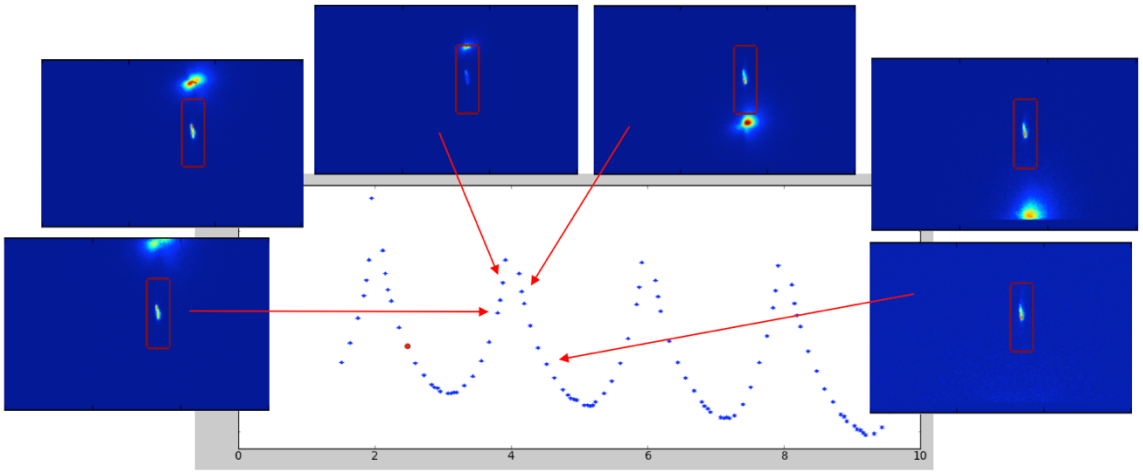

Figure 4.2: Reflected CTR intensity near the Bragg peak.

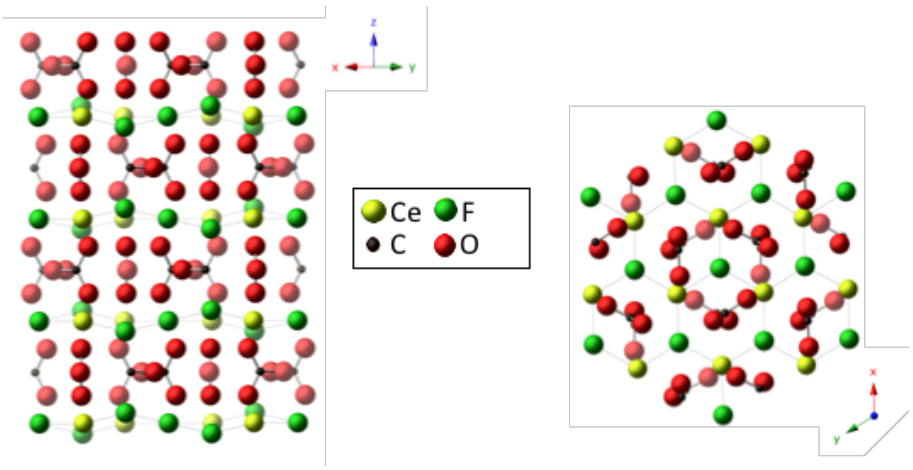

Figure 4.3: Crystal Structure of Bastnäsite

Figure 4.4: Natural bastnäsite crystals, prominently displaying the (001) surface.

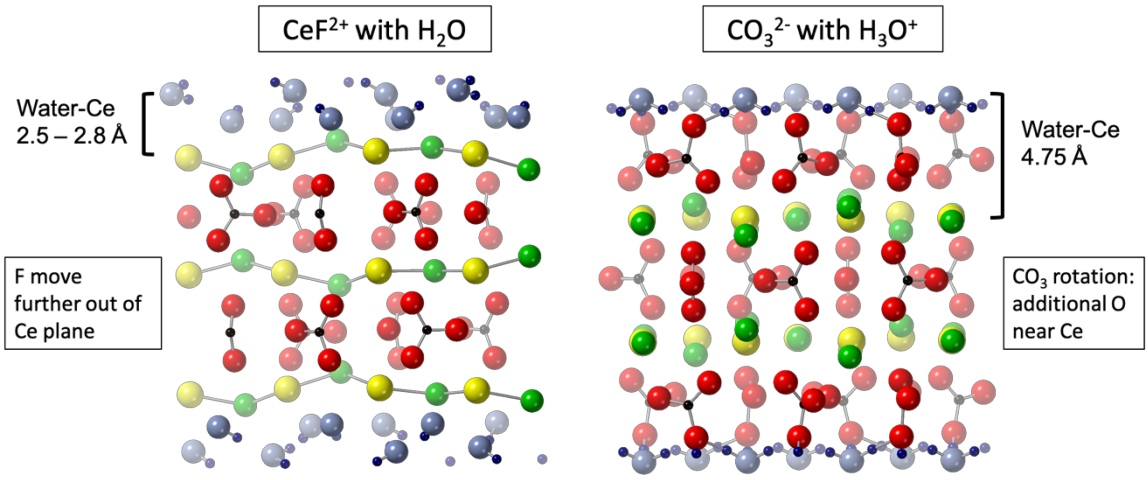

Figure 4.5: Modeled bastnäsite (001) surface arrangements

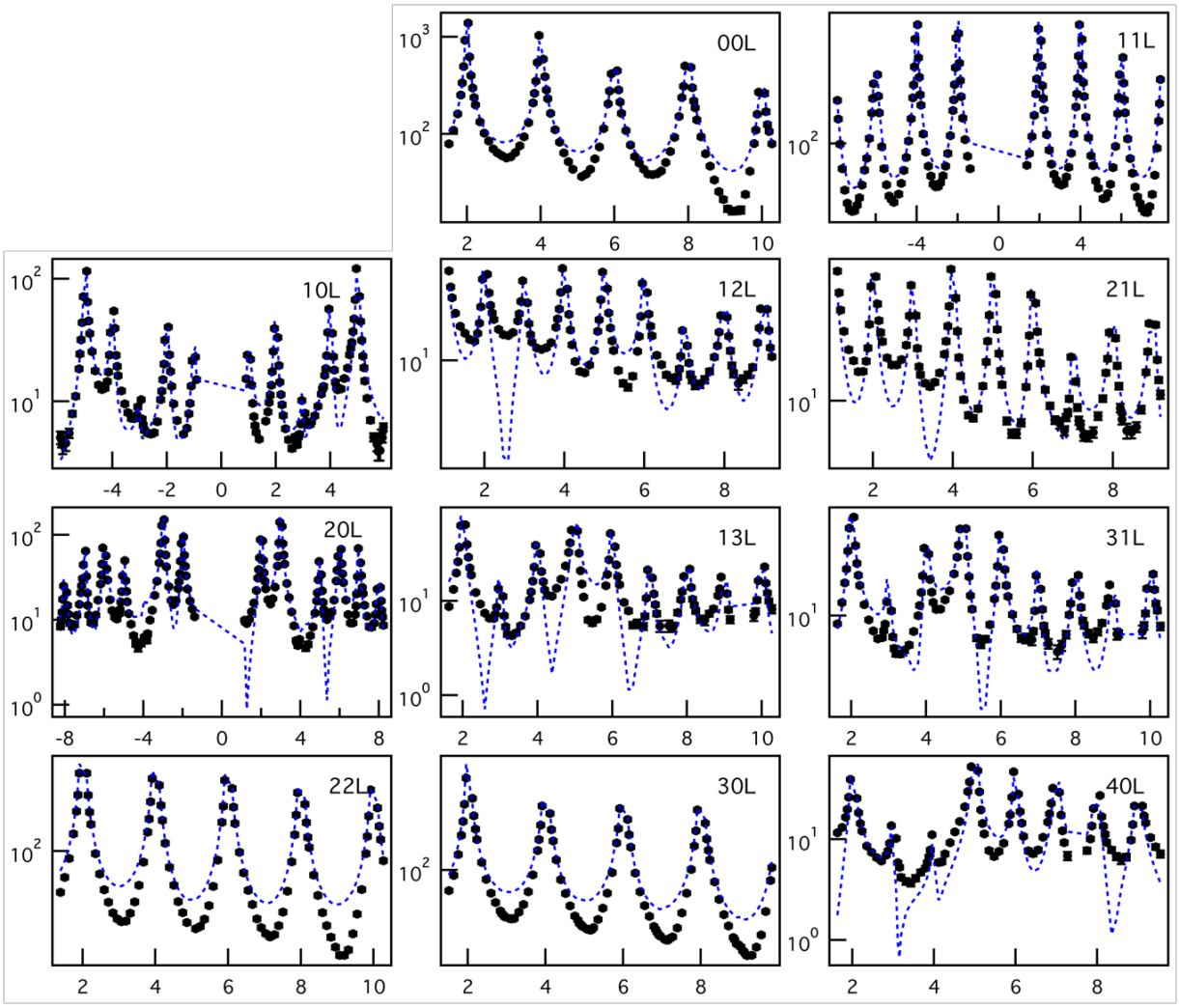

Figure 4.6: CTR data in air

Black dots represent measured intensities. The blue traces are the simulated intensities of a carbonate-terminated model structure before parameters were added to relax atomic positions.

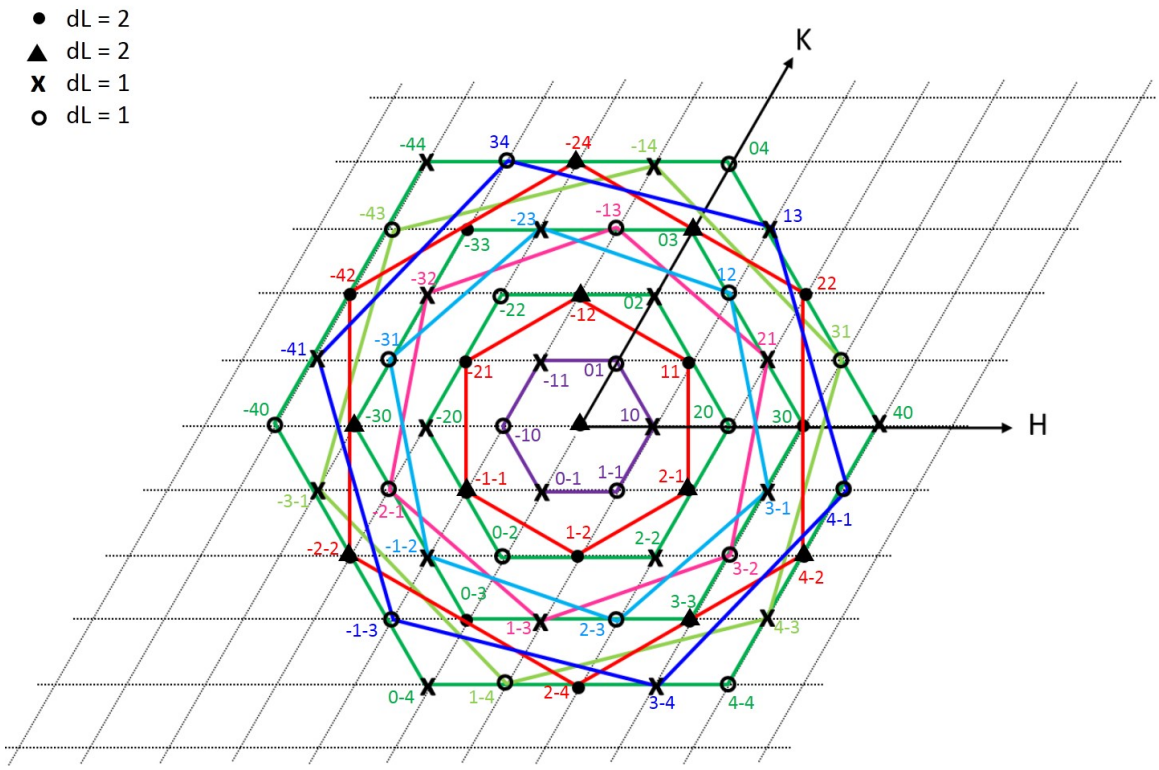

Figure 4.7: Bastnäsite Crystal Symmetry

Symmetry equivalent rods are equidistant from midpoint (0,0,L) and separated by 120º rotation; for instance, (1,0,L) and (0,-1,L) are equivalent.

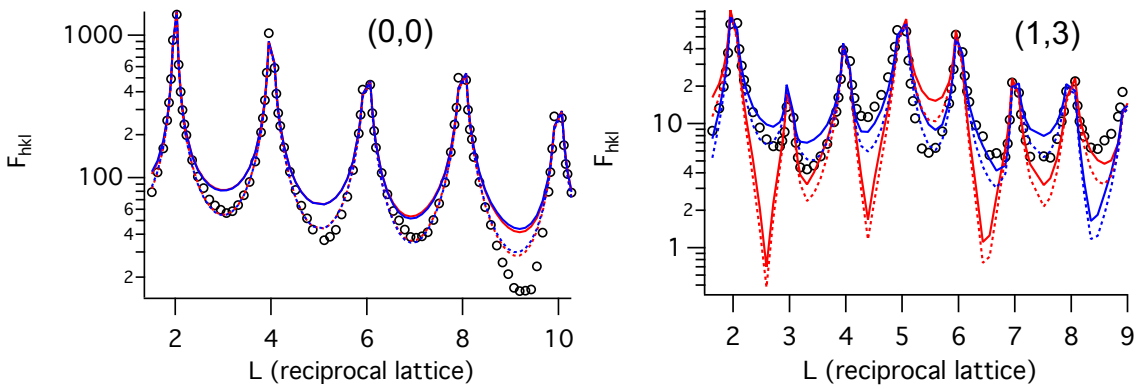

Figure 4.8: Fit of bulk structure after intensity and roughness adjustments

Red traces represent the CeF-terminated structure. Blue traces are CO_3-terminated structure.

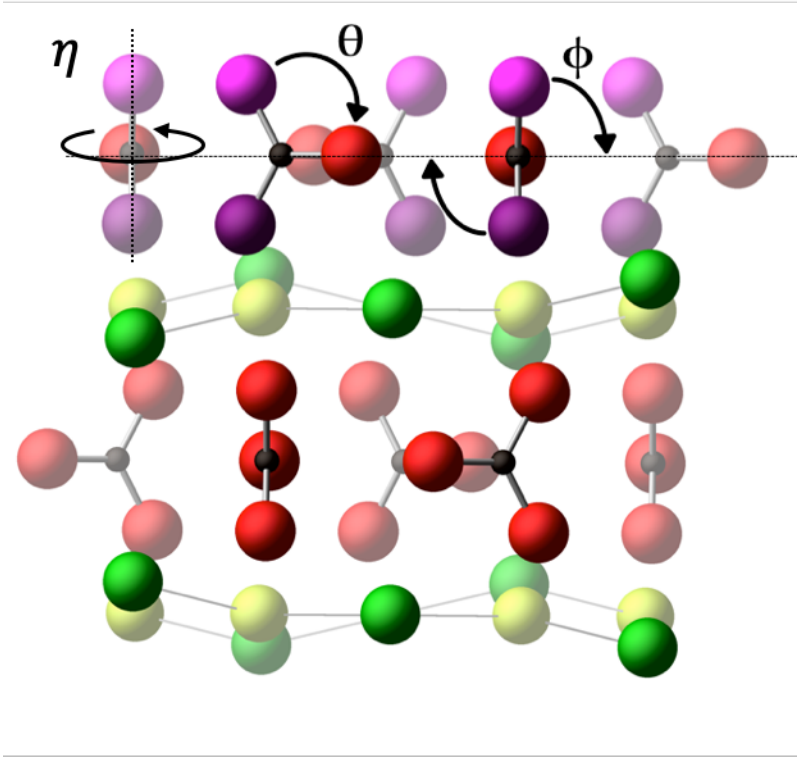

Figure 4.9: Carbonate rotation parameters added

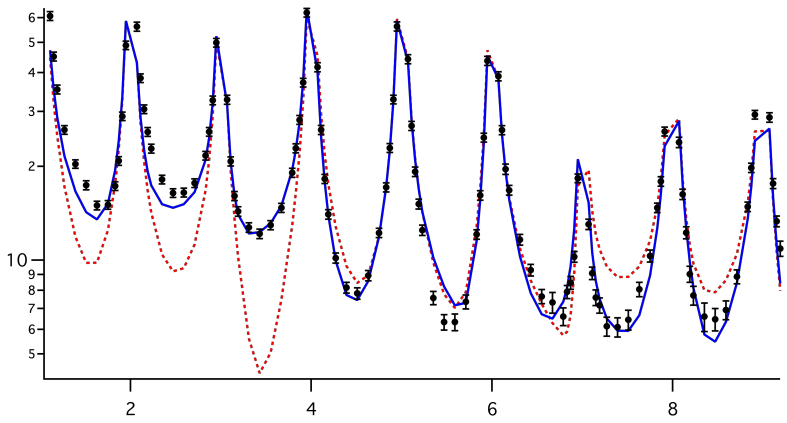

Figure 4.10: Effect of carbonate rotation on the 21L rod

Red trace is before, and blue trace is after rotation parameters are added.

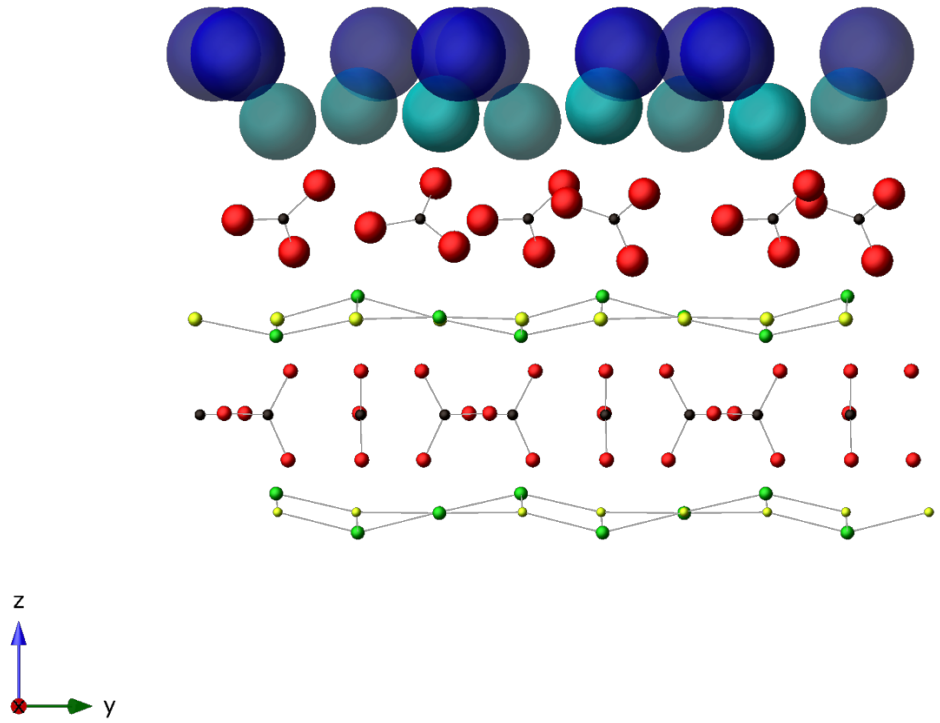

Figure 4.11: Best-fit model of the bastnäsite surface

Atom sizes represent Debye-Waller displacement (70% probability). Blue atoms above surface carbonates correspond to ordered adsorbed water.

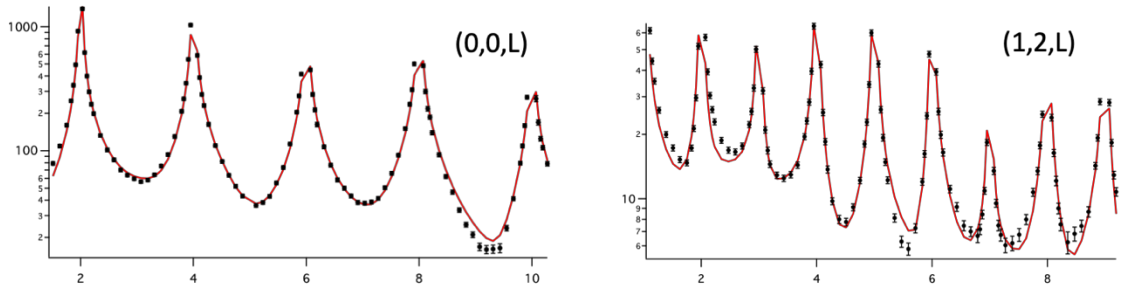

Figure 4.12: CTR model fit versus data

CHAPTER 5
CONCLUSION

In this work, a multifaceted approach was taken to investigate surface chemistry aspects of the bastnäsite flotation system, revealing important insights into the development of new collectors. In Chapters 2 and 3, vibrational spectra of the ligands in the adsorbed state was measured in-situ using ATR-FTIR spectroscopy. Infrared bands corresponding to the functional groups indicate the adsorption mechanism. Comparing the adsorption of similar ligands to bastnäsite reveals relationships between ligand structure and selectivity.

This work is consistent with decades of research supporting the affinity of the hydroxamic acid functional group for bastnäsite surfaces. A comparison of a few related hydroxamate collectors revealed ways in which the ligand structure influences flotation performance. Given the strength of hydroxamate chelation with rare earth cations, this family of ligands is a promising route to developing better collectors for bastnäsite. A possible advantage of hydroxamates with aromatic rings, for instance, as opposed to long alkyl chains, is a slight decrease in hydrophobicity. This may improve ligand selectivity—specifically, by limiting flotation of undesired ores, which may have a relatively smaller amount of ligand adsorbed. Ligands that adsorb more readily, and exhibit greater hydrophobicity, will improve bastnäsite recovery, at the cost of reduced selectivity. Future work could investigate similar hydroxamic acid collectors—possibly featuring two hydroxamate functional groups in different geometries—to recover bastnäsite at very low concentrations.

In Chapter 4, the bastnäsite (001) surface structure was determined using X-ray reflectivity measurements. The data was fit to models of the surface using GenX to determine the structural changes that occur when the surface reacts with aqueous solutions. These findings show a complicated surface, that features a highly-relaxed carbonate layer.

This lends some perspective to decades of attempts to develop more selective collectors. The bastnäsite surface is apparently more difficult to target than previously anticipated. Further investigations into this surface will determine whether the surface termination is altered under varying aqueous conditions. This may present opportunities to pretreat surfaces prior to froth flotation. As methods for inventing new ligands become more sophisticated, the assumptions behind these methods must catch up to the level of detail needed. This will ultimately improve the production of rare earth minerals, importantly, reducing the high environmental cost.

APPENDIX

GenX Model Code

```
# import modules and packages
import models.sxrd as model
#import models.sxrd_uanis2 as model
from models.utils import UserVars
import numpy as np

# Define the unit cell parameters
unitcell = model.UnitCell(7.1129, 7.1129, 9.7577, 90, 90, 120)

# Define the instrument
inst = model.Instrument(wavel = .831, alpha = 2.0)

# Define user variables
usr=UserVars()
usr.new_var('termA', 1.0)
usr.new_var('beta', 0.0)

# Define the bulk
bulk = model.Slab()

# 4.a Define the atoms
#            atom name, element, x,    y,          z,          Uh,       Uk,       Ul, Uhk,   occupancy
bulk.add_atom('O1','o',      0.67456, 0.05706, 0.86455, 0.0147, 1)
bulk.add_atom('O2','o',      0.3825,  0.32544, 0.86455, 0.0147, 1)
bulk.add_atom('O3','o',      0.94294, 0.6175,  0.86455, 0.0147, 1)
bulk.add_atom('C1','c',      0.6779,  0.9698,  0.7500,  0.0083, 1)
bulk.add_atom('C2','c',      0.2919,  0.3221,  0.7500,  0.0083, 1)
bulk.add_atom('C3','c',      0.0302,  0.7081,  0.7500,  0.0083,  1)
bulk.add_atom('O4','o',      0.6827,  0.7914,  0.7500,  0.0151,  1)
bulk.add_atom('O5','o',      0.1087,  0.3173,  0.7500,  0.0151, 1)
bulk.add_atom('O6','o',      0.2086,  0.8913,  0.7500,  0.0151, 1)
bulk.add_atom('O7','o',      0.67456, 0.05706, 0.63545, 0.0147, 1)
bulk.add_atom('O8','o',      0.3825,  0.32544, 0.63545, 0.0147, 1)
bulk.add_atom('O9','o',      0.94294, 0.6175,  0.63545, 0.0147, 1)
bulk.add_atom('F2','f',      0.3333,  0.6667,  0.5504,  0.0126, 1)
bulk.add_atom('Ce1','ce',    0.33914, 0.0000,  0.5000,  0.00606, 1)
bulk.add_atom('Ce2','ce',    0.66086, 0.66086, 0.5000,  0.00606, 1)
bulk.add_atom('Ce3','ce',    0.0000,  0.33914, 0.5000,  0.00606, 1)
bulk.add_atom('F3','f',      0.0000,  0.0000,  0.5000,  0.0126,  1)
bulk.add_atom('F4','f',      0.6666,  0.3333,  0.4496,  0.0126,  1)
bulk.add_atom('O10','o',     0.32544, 0.3825,  0.36455, 0.0147,  1)
bulk.add_atom('O11','o',     0.6175,  0.94294, 0.36455, 0.0147,  1)
bulk.add_atom('O12','o',     0.05706, 0.67456, 0.36455, 0.0147,  1)
bulk.add_atom('C4','c',      0.3221,  0.2919,  0.2500,  0.0083,  1)
bulk.add_atom('C5','c',      0.7081,  0.0302,  0.2500,  0.0083,  1)
bulk.add_atom('C6','c',      0.9698,  0.6779,  0.2500,  0.0083,  1)
bulk.add_atom('O13','o',     0.3173,  0.1087,  0.2500,  0.0151,  1)
bulk.add_atom('O14','o',     0.8913,  0.2086,  0.2500,  0.0151,  1)
bulk.add_atom('O15','o',     0.7914,  0.6827,  0.2500,  0.0151,  1)
bulk.add_atom('O16','o',     0.32544, 0.3825,  0.13545, 0.0147,  1)
bulk.add_atom('O17','o',     0.6175,  0.94294, 0.13545, 0.0147,  1)
bulk.add_atom('O18','o',     0.05706, 0.67456, 0.13545, 0.0147,  1)
bulk.add_atom('F5','f',      0.6667,  0.3333,  0.0504,  0.0126,  1)
```

```
bulk.add_atom('Ce4','ce',   0.33914, 0.0000,  0.0000,  0.00606, 1)
bulk.add_atom('Ce5','ce',   0.66086, 0.66086, 0.0000,  0.00606, 1)
bulk.add_atom('Ce6','ce',   0.0000,  0.33914, 0.0000,  0.00606, 1)
bulk.add_atom('F6','f',     0.0000,  0.0000,  0.0000,  0.0126,  1)
bulk.add_atom('F1','f',     0.3334,  0.6667,  -0.0504, 0.0126,  1)

#Define a surface unit cell
surf1 =  model.Slab(c = 1.0)
#           atom name, element, x,   y,         z,         Uh,      Uk,      Ul, Uhk,  occ, mult
#surface unit cell
surf1.add_atom('O1','o',    0.67456, 0.05706, 0.86455, 0.0147,  1,3)
surf1.add_atom('C1','c',    0.6779,  0.9698,  0.7500,  0.0083,  1,3)
surf1.add_atom('O4','o',    0.6827,  0.7914,  0.7500,  0.0151,  1,3)
surf1.add_atom('O7','o',    0.67456, 0.05706, 0.63545, 0.0147,  1,3)
surf1.add_atom('F2','f',    0.3333,  0.6667,  0.5504,  0.0126,  1,1)
surf1.add_atom('Ce1','ce',  0.33914, 0.0000,  0.5000,  0.00606, 1,3)
surf1.add_atom('F3','f',    0.0000,  0.0000,  0.5000,  0.0126,          1,1)
surf1.add_atom('F4','f',    0.6666,  0.3333,  0.4496,  0.0126,          1,1)
surf1.add_atom('O10','o',   0.32544, 0.3825,  0.36455, 0.0147,  1,3)
surf1.add_atom('C4','c',    0.3221,  0.2919,  0.2500,  0.0083, 1,3)
surf1.add_atom('O13','o',   0.3173,  0.1087,  0.2500,  0.0151,  1,3)
surf1.add_atom('O16','o',   0.32544, 0.3825,  0.13545, 0.0147,  1,3)
surf1.add_atom('F5','f',    0.6667,  0.3333,  0.0504,  0.0126,          1,1)
surf1.add_atom('Ce4','ce',  0.33914, 0.0000,  0.0000,  0.00606, 1,3)
surf1.add_atom('F6','f',    0.0000,  0.0000,  0.0000,  0.0126,          1,1)
surf1.add_atom('F1','f',    0.3334,  0.6667,  -0.0504, 0.0126,  1,1)


#adsorbates (Oad1-3 in F-like positions, Oad4 in Ce-like positions)
surf1.add_atom('Oad1','o', 0.6667,  0.3333,  1.0504,  0.04,     0,1)
surf1.add_atom('Oad2','o', 0.0000,  0.0000,  1.0000,  0.04,     0,1)
surf1.add_atom('Oad3','o', 0.3334,  0.6667,  0.9496,  0.04,     0,1)

surf1.add_atom('Oad4','o', 0.33914, 0.0000,  1.0000,  0.04,     0,3)


#Define atom groups
surf1_F13 = surf1['F2'] + surf1['F3'] + surf1['F4']
surf1_CO2 = surf1['C1'] + surf1['O4'] + surf1['O7']
surf1_CO3 = surf1['C1'] + surf1['O1'] + surf1['O4'] + surf1['O7']
surf1_CO3_2 = surf1['C4'] + surf1['O10'] + surf1['O13'] + surf1['O16']
surf1_Oad123 = surf1['Oad1'] + surf1['Oad2'] + surf1['Oad3']



# Define the rotoinversion axis parameters for the creation of the terminations
# 1. an arbitrary point on the rotoinversion axis
P = np.matrix([0.00,0.00,0.00])
# 2. the rotation part around the rotoinversion axis
R = np.matrix([[0,1,0],[1,0,0],[0,0,1]])
# 3. the translational part along the rotoinversion axis
T = np.matrix([0.0,0.0,0.5])

# Create the first termination
sample = model.Sample(inst, bulk, [surf1], unitcell)
```

```
# 7 Symmetry operations - example for p3 symmetry
p3 = [model.SymTrans([[1, 0],[0, 1]]), model.SymTrans([[0, -1],[1, -1]]),model.SymTrans([[-1, 1],[-1, 0]]) ]

#Defining the user variables for carbonate rotation
usr.new_var('O4theta0', 0.0) #This is the original angle between O4 and C1 in y,z
usr.new_var('dtheta', 0.0) #This is the degree of rotation in y,z about C1
usr.new_var('distO4', 0.0) #Original distance between O4 and C1 in yparallel,z
usr.new_var('distO1', 0.0) #Original distance between O1 and C1 in yparallel,z
usr.new_var('dphi', 0.0) #Degree of phi rotation in ynormal, z
usr.new_var('deta', 0.0) #Degree of eta rotation in yparallel, ynormal

#I calculate starting phi angles and distances in sim function, so not sure they have to be variables.
#usr.new_var('O1phi0', 0) #Original O1-C1 angle in ynormal,z
#usr.new_var('O4phi0', 0) #Original O4-C1 angle in ynormal,z
#usr.new_var('O7phi0', 0) #Original O7-C1 angle in ynormal,z
#usr.new_var('distO1n', 0.0) #Original distance between O1 and C1 in ynormal, z
#usr.new_var('distO4n', 0.0) #O4-C1 distance in ynormal,z
#usr.new_var('distO7n', 0.0) #O7-C1 distance in ynormal,z

usr.new_var('CO3dx', 0.0) #Amount that the group is translated in x
usr.new_var('CO3dy', 0.0) #Amount that the gruop is translated in y
usr.new_var('CO3dz', 0.0) #Amount that the group is translated in z

usr.new_var('O4yp0', -1.2860123) #Original O4-C1 distance parallel to y axis
usr.new_var('O4z0', 0) #Original O4-C1 distance in z
#usr.new_var('O4yp', 0) #Theta rotated O4-C1 distance parallel to y
#usr.new_var('O4z', 0) #Theta rotated O4-C1 distance in z
usr.new_var('O4yn0', 0.02956777) #Original O4-C1 distance normal to y
#usr.new_var('O4yn', 0) #Phi rotated O4-C1 distance in yn
#usr.new_var('O4z2', 0) #Phi rotated O4-C1 distance in z

usr.new_var('O1yp0', 0.6325502) #Original O1-C1 distance parallel to y axis
usr.new_var('O1z0', 1.11774454)  #Original O1-C1 distance in z
#usr.new_var('O1yp', 0)  #Theta rotated O1-C1 distance parallel to y
#usr.new_var('O1z', 0) #Theta rotated O1-C1 distance in z
usr.new_var('O1yn0', -0.02057424) #Original O1-C1 distance normal to y
#usr.new_var('O1yn', 0) #Phi rotated O1-C1 distance in yn
#usr.new_var('O1z2', 0) #Phi rotated O1-C1 distance in z

usr.new_var('O7yp0', 0.6325502)  #Original O7-C1 distance parallel to y axis
usr.new_var('O7z0', -1.11774454)  #Original distance in z
#usr.new_var('O7yp', 0) #Theta rotated O7-C1 distance parallel to y
#usr.new_var('O7z', 0) #Theta rotated O7-C1 distance in z
usr.new_var('O7yn0', -0.02057424) #Original O7-C1 distance normal to y
#usr.new_var('O7yn', 0) #Phi rotated O7-C1 distance in yn
#usr.new_var('O7z2', 0) #Phi rotated O4-C1 distance in yn

usr.O4theta0 = np.degrees(np.arctan(usr.O4z0/usr.O4yp0))

usr.new_var('O13yn0', -0.02956777) #Original O13-C4 distance normal to y
usr.new_var('O10yn0', 0.02057424) #Original O10-C4 distance normal to y

#C1 and C2 bond lengths in yz and xz planes are the same. Both ignore the third component.
usr.distO4 = np.sqrt((usr.O4yp0*usr.O4yp0)+(usr.O4z0*usr.O4z0))
usr.distO1 = np.sqrt((usr.O1yp0*usr.O1yp0)+(usr.O1z0*usr.O1z0))
```

```
#Phi angles and bond lengths use z that depends on theta rotation, so I'm putting their calculations in the
sim function instead.

#Second layer 'thetab' and 'phib' variables
usr.new_var('dthetab', 0.0) #This is the degree of second layer theta rotation in y,z about C4
usr.new_var('dphib', 0.0) #Degree of second layer phi rotation in ynormal, z


usr.new_var('CO3bdx', 0.0) #Amount that the second layer is translated in x
usr.new_var('CO3bdy', 0.0) #Amount that the second layer is translated in y
usr.new_var('CO3bdz', 0.0) #Amount that the second layer is translated in z




# 9 Define the Sim function

# Define the Sim function
def Sim(data):
    # Apply carbonate theta rotation
    #theta_a = usr.theta0 + usr.dtheta
    #theta_b = usr.theta0 + 60 + usr.dtheta  --Changing to actual calculated angle (about 60.5)
    #theta_c = usr.theta0 - 60 + usr.dtheta
    O1theta0 = np.degrees(np.arctan(usr.O1z0/usr.O1yp0))
    O7theta0 = np.degrees(np.arctan(usr.O7z0/usr.O7yp0))


    O4z = usr.distO4*(-1*np.sin(np.radians(usr.O4theta0+usr.dtheta)))
    #surf1.setO4dz(((O4z-usr.O4z0)/9.7577)+usr.CO3dz)
    O4yp = usr.distO4*(-1*np.cos(np.radians(usr.O4theta0+usr.dtheta)))
    #surf1.setO4dy(((O4yp-usr.O4yp0)/7.1129)+usr.CO3dy)
    #surf1.setO4dx(usr.CO3dx)

    O1z = usr.distO1*(np.sin(np.radians(O1theta0+usr.dtheta)))
    #surf1.setO1dz(((O1z-usr.O1z0)/9.7577)+usr.CO3dz)
    O1yp = usr.distO1*(np.cos(np.radians(O1theta0+usr.dtheta)))
    #surf1.setO1dy(((O1yp-usr.O1yp0)/7.1129)+usr.CO3dy)
    #surf1.setO1dx(usr.CO3dx)

    O7z = usr.distO1*(np.sin(np.radians(O7theta0+usr.dtheta)))
    #surf1.setO7dz(((O7z-usr.O7z0)/9.7577)+usr.CO3dz)
    O7yp = usr.distO1*(np.cos(np.radians(O7theta0+usr.dtheta)))
    #surf1.setO7dy(((O7yp-usr.O7yp0)/7.1129)+usr.CO3dy)
    #surf1.setO7dx(usr.CO3dx)

    #Apply phi rotation -- Start angles and bond lengths depend on z from theta rotation.
    O1phi0 = np.degrees(np.arctan(O1z/usr.O1yn0))
    O4phi0 = np.degrees(np.arctan(O4z/usr.O4yn0))
    O7phi0 = np.degrees(np.arctan(O7z/usr.O7yn0))

    distO1n = np.sqrt((usr.O1yn0*usr.O1yn0)+(O1z*O1z))
    distO4n = np.sqrt((usr.O4yn0*usr.O4yn0)+(O4z*O4z))
    distO7n = np.sqrt((usr.O7yn0*usr.O7yn0)+(O7z*O7z))

    O1yn = distO1n*(-1*np.cos(np.radians(usr.dphi+O1phi0)))
    O1z2 = distO1n*(-1*np.sin(np.radians(usr.dphi+O1phi0)))
```

```
#    surf1.setO1dx((2*(O1yn-usr.O1yn0)/(7.1129*np.sqrt(3)))+usr.CO3dx)
#    surf1.setO1dy((((O1yp-usr.O1yp0)/7.1129)+((O1yn-usr.O1yn0)/(7.1129*np.sqrt(3))))+usr.CO3dy)
     surf1.setO1dz(((O1z2-usr.O1z0)/9.7577)+usr.CO3dz)

     O4yn = distO4n*(np.cos(np.radians(usr.dphi+O4phi0)))
     O4z2 = distO4n*(np.sin(np.radians(usr.dphi+O4phi0)))
#    surf1.setO4dx((2*(O4yn-usr.O4yn0)/(7.1129*np.sqrt(3)))+usr.CO3dx)
#    surf1.setO4dy((((O4yp-usr.O4yp0)/7.1129)+((O4yn-usr.O4yn0)/(7.1129*np.sqrt(3))))+usr.CO3dy)
     surf1.setO4dz(((O4z2-usr.O4z0)/9.7577)+usr.CO3dz)

     O7yn = distO7n*(-1*np.cos(np.radians(usr.dphi+O7phi0)))
     O7z2 = distO7n*(-1*np.sin(np.radians(usr.dphi+O7phi0)))
#    surf1.setO7dx((2*(O7yn-usr.O7yn0)/(7.1129*np.sqrt(3)))+usr.CO3dx)
#    surf1.setO7dy((((O7yp-usr.O7yp0)/7.1129)+((O7yn-usr.O7yn0)/(7.1129*np.sqrt(3))))+usr.CO3dy)
     surf1.setO7dz(((O7z2-usr.O7z0)/9.7577)+usr.CO3dz)

     surf1.setC1dx(usr.CO3dx)
     surf1.setC1dy(usr.CO3dy)
     surf1.setC1dz(usr.CO3dz)

     #Apply eta rotation in x/y plane
     O1eta0 = np.degrees(np.arctan(O1yp/O1yn))
     O4eta0 = np.degrees(np.arctan(O4yp/O4yn))
     O7eta0 = np.degrees(np.arctan(O7yp/O7yn))

     distO1xy = np.sqrt((O1yn*O1yn)+(O1yp*O1yp))
     distO4xy = np.sqrt((O4yn*O4yn)+(O4yp*O4yp))
     distO7xy = np.sqrt((O7yn*O7yn)+(O7yp*O7yp))

     if O1eta0 < 0:
        O1yn2 = distO1xy*(-1*np.cos(np.radians(usr.deta+O1eta0)))
        O1yp2 = distO1xy*(-1*np.sin(np.radians(usr.deta+O1eta0)))
     else:
        O1yn2 = distO1xy*(np.cos(np.radians(usr.deta+O1eta0)))
        O1yp2 = distO1xy*(np.sin(np.radians(usr.deta+O1eta0)))

     surf1.setO1dx((2*(O1yn2-usr.O1yn0)/(7.1129*np.sqrt(3)))+usr.CO3dx)
     surf1.setO1dy((((O1yp2-usr.O1yp0)/7.1129)+((O1yn2-usr.O1yn0)/(7.1129*np.sqrt(3))))+usr.CO3dy)
#    surf1.setO1dz(((O1z2-usr.O1z0)/9.7577)+usr.CO3dz)

     if O4eta0 < 0:
        O4yn2 = distO4xy*(np.cos(np.radians(usr.deta+O4eta0)))
        O4yp2 = distO4xy*(np.sin(np.radians(usr.deta+O4eta0)))
     else:
        O4yn2 = distO4xy*(-1*np.cos(np.radians(usr.deta+O4eta0)))
        O4yp2 = distO4xy*(-1*np.sin(np.radians(usr.deta+O4eta0)))

     surf1.setO4dx((2*(O4yn2-usr.O4yn0)/(7.1129*np.sqrt(3)))+usr.CO3dx)
     surf1.setO4dy((((O4yp2-usr.O4yp0)/7.1129)+((O4yn2-usr.O4yn0)/(7.1129*np.sqrt(3))))+usr.CO3dy)
#    surf1.setO4dz(((O4z2-usr.O4z0)/9.7577)+usr.CO3dz)

     if O7eta0 < 0:
        O7yn2 = distO7xy*(-1*np.cos(np.radians(usr.deta+O7eta0)))
        O7yp2 = distO7xy*(-1*np.sin(np.radians(usr.deta+O7eta0)))
     else:
        O7yn2 = distO7xy*(np.cos(np.radians(usr.deta+O7eta0)))
```

```
      O7yp2 = distO7xy*(np.sin(np.radians(usr.deta+O7eta0)))

   surf1.setO7dx((2*(O7yn2-usr.O7yn0)/(7.1129*np.sqrt(3)))+usr.CO3dx)
   surf1.setO7dy((((O7yp2-usr.O7yp0)/7.1129)+((O7yn2-usr.O7yn0)/(7.1129*np.sqrt(3))))+usr.CO3dy)
#    surf1.setO7dz(((O7z2-usr.O7z0)/9.7577)+usr.CO3dz)

#    surf1.setC1dx(usr.CO3dx)
#    surf1.setC1dy(usr.CO3dy)
#    surf1.setC1dz(usr.CO3dz)

   # Apply second layer carbonate theta rotation

   O13z = usr.distO4*(-1*np.sin(np.radians(usr.O4theta0+usr.dthetab)))
   #surf1.setO4dz(((O4z-usr.O4z0)/9.7577)+usr.CO3dz)
   O13yp = usr.distO4*(-1*np.cos(np.radians(usr.O4theta0+usr.dthetab)))
   #surf1.setO4dy(((O4yp-usr.O4yp0)/7.1129)+usr.CO3dy)
   #surf1.setO4dx(usr.CO3dx)

   O10z = usr.distO1*(np.sin(np.radians(O1theta0+usr.dthetab)))
   #surf1.setO1dz(((O1z-usr.O1z0)/9.7577)+usr.CO3dz)
   O10yp = usr.distO1*(np.cos(np.radians(O1theta0+usr.dthetab)))
   #surf1.setO1dy(((O1yp-usr.O1yp0)/7.1129)+usr.CO3dy)
   #surf1.setO1dx(usr.CO3dx)

   O16z = usr.distO1*(np.sin(np.radians(O7theta0+usr.dthetab)))
   #surf1.setO7dz(((O7z-usr.O7z0)/9.7577)+usr.CO3dz)
   O16yp = usr.distO1*(np.cos(np.radians(O7theta0+usr.dthetab)))
   #surf1.setO7dy(((O7yp-usr.O7yp0)/7.1129)+usr.CO3dy)
   #surf1.setO7dx(usr.CO3dx)

   #Apply second layer phi rotation -- Start angles and bond lengths depend on z from theta rotation.
   O10phi0 = np.degrees(np.arctan(O10z/usr.O10yn0))
   O13phi0 = np.degrees(np.arctan(O13z/usr.O13yn0))
   O16phi0 = np.degrees(np.arctan(O16z/usr.O10yn0))

   distO10n = np.sqrt((usr.O10yn0*usr.O10yn0)+(O10z*O10z))
   distO13n = np.sqrt((usr.O13yn0*usr.O13yn0)+(O13z*O13z))
   distO16n = np.sqrt((usr.O10yn0*usr.O10yn0)+(O16z*O16z))

   O10yn = distO10n*(np.cos(np.radians(usr.dphib+O10phi0)))
   O10z2 = distO10n*(np.sin(np.radians(usr.dphib+O10phi0)))
   surf1.setO10dx((2*(O10yn-usr.O10yn0)/(7.1129*np.sqrt(3)))+usr.CO3bdx)
   surf1.setO10dy((((O10yp-usr.O1yp0)/7.1129)+((O10yn-usr.O10yn0)/(7.1129*np.sqrt(3))))+usr.CO3bdy)
   surf1.setO10dz(((O10z2-usr.O1z0)/9.7577)+usr.CO3bdz)

   O13yn = distO13n*(-1*np.cos(np.radians(usr.dphib+O13phi0)))
   O13z2 = distO13n*(-1*np.sin(np.radians(usr.dphib+O13phi0)))
   surf1.setO13dx((2*(O13yn-usr.O13yn0)/(7.1129*np.sqrt(3)))+usr.CO3bdx)
   surf1.setO13dy((((O13yp-usr.O4yp0)/7.1129)+((O13yn-usr.O13yn0)/(7.1129*np.sqrt(3))))+usr.CO3bdy)
   surf1.setO13dz(((O13z2-usr.O4z0)/9.7577)+usr.CO3bdz)

   O16yn = distO16n*(np.cos(np.radians(usr.dphib+O16phi0)))
   O16z2 = distO16n*(np.sin(np.radians(usr.dphib+O16phi0)))
   surf1.setO16dx((2*(O16yn-usr.O10yn0)/(7.1129*np.sqrt(3)))+usr.CO3bdx)
   surf1.setO16dy((((O16yp-usr.O7yp0)/7.1129)+((O16yn-usr.O10yn0)/(7.1129*np.sqrt(3))))+usr.CO3bdy)
   surf1.setO16dz(((O16z2-usr.O7z0)/9.7577)+usr.CO3bdz)
```

```
    surf1.setC4dx(usr.CO3bdx)
    surf1.setC4dy(usr.CO3bdy)
    surf1.setC4dz(usr.CO3bdz)



    # create the domains by applying the screw axis operation
    sample_d0 = sample                      # A-domain
    sample_d1 = rotodomain(sample,P,R,T,1)     # B-domain
    sample_d0.set_surface_sym(p3)           # A-domain p3 symmetry
    sample_d1.set_surface_sym(p3)           # B-domain p3 symmetry

    # Simulate the rods
    h = np.concatenate([set.extra_data['h'] for set in data[:]])
    k = np.concatenate([set.extra_data['k'] for set in data[:]])
    l = np.concatenate([set.x for set in data[:]])
    LB = np.concatenate([set.extra_data['LB'] for set in data[:]])
    dL = np.concatenate([set.extra_data['dL'] for set in data[:]])
    beta = usr.beta
    rough = (1-beta)/((1-beta)**2 + 4*beta*np.sin(np.pi*(l - LB)/dL)**2)**0.5

    f_d0 = sample_d0.calc_f(h, k, l)
    f_d1 = sample_d1.calc_f(h, k, l)

    # Incoherent addition of the two domains A,B
    f_tot2 = (usr.termA*(abs(f_d0)**2) + ((1-usr.termA)*abs(f_d1)**2))
    f_tot = rough*np.sqrt(f_tot2)


    # prepare array to return
    ind = 0
    l = []
    for set in data[:]:
        l.append(f_tot[ind:ind+len(set.x)])
        ind = ind + len(set.x)
    return l


#============================
def rotoaxis(myslab,P,R,T,n):
    newslab = myslab.copy()
    x = newslab.x
    y = newslab.y
    z = newslab.z
    dx = newslab.dx
    dy = newslab.dy
    dz = newslab.dz

    # scale T with the c-parameter along the z-direction
    T2 = T.copy()
    T2[:,2] = T2[:,2]/newslab.c


    # transform the xyz coordinates of the atoms
    xyz = np.matrix([x,y,z])
```

```
    xyz = xyz.transpose()

    xyz = xyz-P
    xyz = xyz*(R**n)+(n*T2)
    xyz = xyz+P

    # move x- and y- coordinates back into intervall [0, 1)
    xyz[:,0] = xyz[:,0] - np.floor(xyz[:,0])
    xyz[:,1] = xyz[:,1] - np.floor(xyz[:,1])

    xyz = np.array(xyz.transpose())

    # now the displacements (only rotation has to be applied)
    dxyz = np.matrix([dx,dy,dz])
    dxyz = dxyz.transpose()

    dxyz = dxyz*(R**n)

    dxyz = np.array(dxyz.transpose())

    newslab.x = xyz[0,:]
    newslab.y = xyz[1,:]
    newslab.z = xyz[2,:]
    newslab.dx = dxyz[0,:]
    newslab.dy = dxyz[1,:]
    newslab.dz = dxyz[2,:]

    return newslab

#================================
def rotodomain(sample,P,R,T,n):

    # transform the bulk slab
    mybulk = rotoaxis(sample.bulk_slab,P,R,T,n)

    # copy of the sample's surface slabs list
    myslabs = sample.slabs[:]

    #transform the surface slabs
    for ii in range(len(myslabs)):
        # apply roto axis rotation
        myslabs[ii] = rotoaxis(myslabs[ii],P,R,T,n)

    # build up transformed sample
    mysample = model.Sample(sample.inst, mybulk, myslabs, sample.unit_cell)

    return mysample
```

VITA

Anna K. Wanhala received a Bachelor of Arts in Chemistry from Albion College in May 2014 before beginning her PhD work in the Bredesen Center for Interdisciplinary Research and Education at The University of Tennessee. Her research focuses on understanding atomic-scale structure and mechanisms of ligand adsorption at the mineral-water interface using X-ray reflectivity and spectroscopic experimental techniques.